GENERATION AND CHARACTERIZATION OF QUANTUM TURBULENCE

By

KYLE J. THOMPSON

A DISSERTATION PRESENTED TO THE GRADUATE SCHOOL
OF THE UNIVERSITY OF FLORIDA IN PARTIAL FULFILLMENT
OF THE REQUIREMENTS FOR THE DEGREE OF
DOCTOR OF PHILOSOPHY

UNIVERSITY OF FLORIDA

2012

© 2012 Kyle J. Thompson

ACKNOWLEDGMENTS

There are many people without whom my journey to completing a dissertation would be much more difficult. First, I would like to thank the different students I have worked with. When they were present there was always an additional energy and urgency in the laboratory. Specifically I owe, Lydia Munday, Dr. Wei Gou, Alex Marakov, Roman Chapurin, Austin Griffith, John Pilkey, Manish Amin, Jihee Yang, Chad Hopkins, Ivan Lozano, Milap Patel, Travis Nelson, Emma Borrowman, Joe Triana, Casey Litton, James Stankowicz, and Carley Nicoletti for their time working with me. In particular, I would like to thank Lydia for spending her weekends for the past month reading over this document, section, by section, to make available the thesis that is here. I would also like to thank Wei Guo for allowing me use his design for second sound transducers and for productive discussions about the control motor design, and the longest tenured undergraduate, Roman who calibrated the first inductive position sensor and spent many hours in the lab.

In addition to the lab members with whom I have worked, the technical staff in the department have been invaluable. The electronics shop have provided me with advice on the manufacture of circuits and always were able to provide the spare parts when necessary. The machinists in the machine shop were always available to discuss my latest design idea and how best to make an apparatus work. The last shop I would like to thank is the cryogenic shop. They always had helium available when it was needed, night and day, weekend and weekday. In addition to their normal job of providing cryogenics they were my primary source of sound engineering advice. Specifically, I would like to thank Greg Labbe for all of his time, attention, and thought he put into my work. More than anyone else, he made the experiments work and has always been a constant source of information.

This project, like so many others, has turned into a multi-university collaborative effort. In no particular order, I would like to thank; Dr. William Vinen from Birmingham

University for creating and being a constant presence in the development of the inertial motor, Dr. Peter McClintock from the University of Lancaster for beginning this research with Gary and developing the idea for the passing motor and Drs. Dan McKinsey and Wei Guo from Yale University who have brought the new and exciting excimer technology to turbulence research,

Finally, I owe a special dept to my chairman and advisor, Gary. G. Ihas. Over the past 5 years he has steadily guided this work and been available with enthusiasm at all times, particularly when the experiments were running.

In addition to all of those I worked with, I would like to thank my colleagues who went through this Ph.D. process with me; Evan Donoghue, Maureen Petterson, Dan Pajerowski, Joe Gartner, Dylan Sweeny, Rich Ottens, Jeff Hoskins, and Danial Arenas. I would also like to thank my friends from Gainesville who have done their best to keep me from getting all my work done, Phil Nassoiy, Sarah Nassoiy, and Mike Greathouse. Finally, last but by no means least, I would like to thank my personal support team and girlfriend Denise Bloom.

TABLE OF CONTENTS

LIST OF TABLES

LIST OF FIGURES

Abstract of Dissertation Presented to the Graduate School
of the University of Florida in Partial Fulfillment of the
Requirements for the Degree of Doctor of Philosophy

GENERATION AND CHARACTERIZATION OF QUANTUM TURBULENCE

By

Kyle J. Thompson

August 2012

Chair: Gary G. Ihas
Major: Physics

Turbulence is a specific type of fluid flow. We all know what it is but it is difficult to define. Turbulence is the rule, rather than the exception and is ubiquitous in nature. It is prevalent in the interstellar dust clouds reaching between the stars and crucial to the plasma dynamics inside them. It can't be ignored in the dynamics of planetary atmospheres, oceans, or cores. It is ubiquitous, from the observable environment down to the internal structure of the human body and every living organism known and unknown. We are composed of and encompassed in an ever changing mess of fluid motion. Nearly the entire universe is in a fluid state, and the majority of fluids are turbulent. Yet there exists no analytic solution to the equations that govern the chaos. This is incredible when pondered; almost everything that can be experienced is governed by the same rules, independent of size, shape or constituents. However, to describe our surroundings we are confined to brute force calculation and experiments. The theories of fluid dynamics are truly theories of everything, and yet, so many properties are still not understood.

Presented in this thesis are: an experimental implementation of an existing linear motor to create the first studies of quantum turbulence created by this means in the low temperature limit; identification of the possible shortfalls of this preliminary motor system; the development of a new, more sophisticated, drive apparatus, and the creation, exploration, and development of new and existing sensors for measuring the

properties of quantum turbulence. Each of the above parts in this thesis are different prongs of a multifaceted approach underway at the University of Florida to understand quantum turbulence across its entire temperature range. The work here builds on the previous projects in the group, to develop millikelvin turbulence machinery and techniques, but also goes forward in a new direction to explore the higher temperature regime with some existing technology (second sound) and promise for using a brand new helium molecule visualization technique. In the end, the work in this thesis is aimed at revealing one more tiny sliver of information of a fascinating phenomenon.

CHAPTER 1
INTRODUCTION

Turbulence is a specific type of fluid flow. We all know what it is but it is difficult to define. Turbulence is the rule, rather than the exception and is ubiquitous in nature. It is prevalent in the interstellar dust clouds reaching between the stars and crucial to the plasma dynamics inside them. It can't be ignored in the dynamics of planetary atmospheres, oceans, or cores. It is ubiquitous, from the observable environment down to the internal structure of the human body and every living organism known and unknown. We are composed of and encompassed in an ever changing mess of fluid motion. Nearly the entire universe is in a fluid state, and the majority of fluids are turbulent. Yet there exists no analytic solution to the equations that govern the chaos. This is incredible when pondered; almost everything that can be experienced is governed by the same rules, independent of size, shape or constituents. However, to describe our surroundings we are confined to brute force calculation and experiments. The theories of fluid dynamics are truly theories of everything, and yet, so many properties are still not understood.

Turbulence is not defined by any single property or equation; there is no critical parameter at which a fluid will suddenly switch from a predictable laminar flow to a stochastic turbulent one. Rather, it is a string of events and a series of properties which define turbulence. Tennekes and Lumley [1] describe turbulence as containing many of the following characteristics: Irregularity of flow, which means that the flow is statistically characterized rather than deterministically. Turbulence is diffuse, the flow properties spread out over many momentum and length scales. The fluid flow has a large Reynolds number which separates the dissipative and kinematic flow regimes. Turbulence is 3 dimensional and contains vorticity in each dimension. The flow must have a source of dissipation. Turbulence requires continuum mechanics, implying that individual atoms and molecules should not factor into the dynamics. Finally, turbulence is a flow

phenomenon, not a fluid property. Among these properties, a defined dissipation source and the continuum mechanics requirement are of particular interest to the quantum turbulence investigated in this thesis.

1.1 General Background

Fluids are primarily described by examining the conservation of momentum, mass, and energy flowing through and contained in an arbitrary test volume. From these governing principles, the Naiver-Stokes equation can be derived,

$$\frac{\partial \rho \vec{v}}{\partial t} + \nabla(\rho \vec{v} \cdot \vec{v}) = -\nabla p + \nabla \cdot \mathbb{T} + \rho \vec{f}. \tag{1–1}$$

Here ρ is the fluid density, $\vec{v}$ is the velocity, p is the pressure, $\mathbb{T}$ is the deviatoric stress tensor, and $\vec{f}$ is the body force on the fluid volume. In general, unless specific and confining assumptions are made, this equation has no analytic solution. The mathematical complexity of this equation enforces that experimentation typically leads theory in our understanding of the dynamics.

The simplest manifestation of turbulence contains homogenous and isotropic vorticity, where the flow is statistically invariant to both cartesian shifts in position and angular rotations, greatly simplifying the Navier-Stokes equation. In other words, for this flow pattern, there is no preferred position or direction in the fluid and on average the fluid "*looks*" the same in every direction. This thesis concentrates on both the creation and characterization of this specific type of turbulence. We have chosen to use liquid helium as our test fluid. Helium, in many regards, is the simplest fluid, yet in other ways the most complex. Before the specific material properties which make helium special are discussed, some basic fluid dynamic concepts that will be pertinent to this work are explained.

1.2 Classical Fluid Dynamics

From the conservation of mass, momentum and energy, the basic forms of fluid dynamics can be derived. All three conservation laws are intuitive, but still powerful

when written with mathematical rigor. However, prior to formulating these equations it is important to note how fluid dynamics differ from solid mechanics. A striking difference is, in fluids the fundamental unit of volume used to describe a flow is a stationary and arbitrary volume which the fluid flows, rather than a specific fluid atom or molecule. Therefore, in a particular test volume there can be both a net acceleration $\frac{\partial}{\partial t}$, and a convective change of the fluid in the volume which change the manner in which the dynamics are described. In hydrodynamics, this property is taken into account by creating a hydrodynamic derivative,

$$\frac{D\vec{A}}{Dt} = \frac{\partial \vec{A}}{\partial t} + \vec{V} \cdot \nabla \vec{A}, \tag{1–2}$$

where the change in the arbitrary vector property $\vec{A}$ is examined both in time and space. The hydrodynamic derivative, Equation 1–2, reduces to $\frac{\partial}{\partial t}$ when the reference frame of the traveling fluid is used.

This type of derivative is best understood by example. Let A represent pressure for this thought experiment. A sensor is sitting in a fluid when the pressure of the fluid is raised. The sensor would measure that change and this is the $\frac{\partial}{\partial t}$ component of the derivative. Now the same sensor is once again in the fluid and a current carries extra fluid into the test volume. In this case, the sensor will measure a change in pressure as a function of the amount of liquid traveling into the sample volume, even though the overall pressure profile of the fluid is left unchanged. This measurement represents the convective portion of the hydrodynamic derivative ($\vec{V} \cdot \nabla \vec{A}$). When both types of pressure change are accounted for, the hydrodynamic derivative for pressure is defined.

The first of the conservation equations, the conservation of mass, is given by the equation,

$$\frac{\partial \rho}{\partial t} + \nabla(\rho \vec{v}) = 0. \tag{1–3}$$

This conservation law is also called “the continuity equation” and it states that the net sum of the incoming to outgoing mass has to equal the change in mass of the test

volume. The second equation is the conservation of momentum, it is also known as the Naiver-Stokes equation and has already been presented in Equation 1–1. Finally there is the conservation of energy,

$$\frac{\partial}{\partial t}(\rho e + \frac{1}{2}\rho v^2) + \nabla \cdot (\rho \vec{v}(e + \frac{1}{2}v^2)) = -\nabla \cdot \vec{q} + \nabla \cdot (\mathbb{T} \cdot \vec{v}) + \rho \vec{v} \cdot \vec{f}, \tag{1–4}$$

where e is the internal energy and q is heat flux. This equation can be further broken into a thermal and kinetic component. However, we will not require this separation to either motivate our work or describe results in this thesis. Therefore, further explanation is superfluous here. For the interested reader, more information can be found in many other sources [1–3]. Together, these three equations form the basis for most fluid dynamic theory. These equations take the form of non-linear partial differential equations which are analytically unsolvable and computationally taxing. To better understand fluid dynamics, simplifying assumptions are necessary and will be explicitly mentioned as they are used in Chapter 1.

The most severe restriction theoretically placed on a system is to stipulate that the velocity field of the fluid is equal to the gradient of a scalar field. This type of flow is called potential flow. The entire velocity field is defined by a scalar potential which eliminates complex flow patterns and vorticity. It is the flow type that is achieved when there are no, or entirely negligible, shear stresses. Descriptions of real physical situations with this simplification are useful for basic understanding of flow patterns. One example of a successful potential flow explanation is the Bernoulli effect which is used to understand the pressures on a spinning baseball or flow over an air plane wing. This simple flow type is always a good place to prepare initial intuitive assumptions. For potential flow, the vector $\vec{v}$ is conservative and can therefore be replaced with $\nabla\Phi$ in the Equations 1–1, 1–3, and 1–4 .

One motivation for using superfluid helium as a test fluid stems from the velocity field being conservative due to quantum effects (see Equation 1–14). The well known

restriction on the velocity field of superfluid helium matches potential flow definition and makes it a naïvely perfect potential flow fluid. If this were the entire story, superfluid helium would be the archetype for tests on potential flow. Potential flow not only simplifies the Naiver-Stokes equations, but this restriction also disallows rotational flow patterns and turbulence. How can this be? The superfluid velocity is defined by the gradient of a scalar, but superfluids have been shown to support both turbulence and turbulent decay. There is clear evidence the apparently simple fluid is interesting and unique.

Another assumption commonly used in fluid dynamics is that the flow is incompressible. Care is needed here as incompressible flow is not the same thing as an incompressible fluid. Helium for example is a very compressible fluid, but the flows that are discussed in this thesis are described in incompressible language. Panton describes incompressible *flows* as "constant density, viscosity, specific heat, and thermal conductivity. With these assumptions, the velocity field can be found using the continuity and momentum equations without regard for the energy equation and equations of state [2]."

The preference of potential flow has motivated work on the dynamics of superfluid helium. But due to unexpected quantum effects, superfluid He^4 is able to support a complex and interesting flow. However, like all fluids there are many different types of flow. We elect to investigate the simplest turbulent system, homogenous and isotropic turbulence . Classically, the most common way to produce this flow type is achieved by pulling a mesh grid through a stationary fluid or conversely flowing a fluid through a stationary grid. We have elected to do the former in superfluid helium.

With incompressible, nearly Newtonian flow, the Naiver-Stokes equation can be simplified to,

$$\frac{\partial \vec{v}}{\partial t} + (\vec{v} \cdot \nabla)\vec{v} = \frac{-\nabla P}{\rho} + \nu \triangle \vec{v} + \frac{\vec{f}}{\rho}. \tag{1–5}$$

In this equation ν is the kinematic viscosity which is defined as the ratio of the dynamic viscosity, μ, and the fluid density, ρ. The left hand side of Equation 1–5 represents the

inertial behavior of the fluid and the right hand side is responsible for describing fluid stress and dissipation. On the left, there is the fluid dynamic derivative describing the fluid motion. $\frac{\partial \vec{v}}{\partial t}$ is the volume unit acceleration and $(\vec{v} \cdot \nabla)\vec{v}$ is the convective acceleration of flow through the sample volume. The right hand side of the equation contains the body force, $\vec{f}$, and the pressure gradient, ∇p, both of which act on the fluid per unit volume. The final term is the dissipative viscous term, $\nu \triangle \vec{v}$, responsible for dissipation. In this simplified form, the Navier-Stokes equation can be made non-dimensional to produce one or more non-dimensional scaling parameters characteristic of the flow. The existance of these parameters is due to dynamic similarity and is possibly the most important concept in fluid dynamics. The non-dimensional parameter relevant for the work in this thesis is the Reynolds number. By transforming each variable to its dimensionless counterpart, we are left with a new variable that is normalized to the fluid and flow. For this process, the doppelganger variables are,

$$\vec{v}' = \frac{\vec{v}}{V}, p' = \frac{p}{\rho v^2}, \vec{f}' = \frac{D}{\rho v^2}, \frac{\partial}{\partial t'} = \frac{D\partial}{V\partial}, \nabla' = D\nabla.$$

With these we can rewrite the Navier-Stokes equation in a non-dimensional form. In the equation above, D is the characteristic length, and v is the mean flow velocity. Plugging the above parameters into the Navier-Stokes equation, omitting the prime symbols, and multiplying through by $D/\rho v^2$, the non-dimensional Navier-Stokes equation is expressed as

$$\frac{\partial \vec{v}}{\partial t} + (\vec{v} \cdot \nabla)\vec{v} = -\nabla P + \frac{1}{Re}\triangle \vec{v} + \vec{f} \tag{1–6}$$

where the Reynolds number, Re, is defined as

$$Re = \frac{DV}{\nu}. \tag{1–7}$$

The Reynolds number represents the ratio of the inertial force to the dissipative viscous force in a particular flow. Therefore, for high Reynolds number, kinetic energy is transported to different length scales without dissipation, while for low Reynolds number

the fluid motion decays into internal heating. The non-dimensional parameters and the unit free Reynolds number and the theory of dynamic similarity state that flows with similar parameters can be measured in one system, and extrapolated into a completely different system without loss of generality.

Since the dissipative forces are inversely proportional to the characteristic length scale D (Equation 1–5 and Equation 1–7), energy is predominantly lost by motion on the smallest scales. In other words high Reynolds number flows are not dissipative, while the low Reynolds number flows are. One of the requirements for turbulence mentioned is the kinetic energy of the flow is spread out over many length scales. However, for flows with high Reynolds number there must be some mechanism which transports the energy from large length scales to the small. This thought led A.N. Kolmogorov in 1941 [4] to derive a formula for the energy spectrum of turbulence across the different scales. However the Kolmogorov theory is asymptotic, it is valid when certain conditions are met. Such conditions are a high Reynolds number, energy is transferred from large length scales to smaller ones, and that the turbulence is random. Here the assumptions and results of the Kolmogorov theory of turbulence are outlined. This general outline can be found in many different texts on classical turbulence [1–3].

With Fourier integrals, the Navier-Stokes equation can be written in spectral form making it transparent how energy may be transferred among different wave numbers. For the first order of energy transfer it is assumed that $k_1 = k_2 + k_3$, where subsequent orders of approximation several more wavenumbers can be involved. For this derivation, it is assumed that the predominant wave number mixing comes from similar k values, or $k_2 \approx k_3$ rather than $k_1 \approx k_2$. This assumption picks the wave numbers that most rapidly advance the energy spectrum in k space, this assumption is also loosened in more rigorous calculations of the energy spectrum. It is clear that mixing of the wave numbers, by summation, leads to ever increasing wave numbers, eventually resulting with a very large value of k_1. This process is envisioned to occur until a cutoff wave

number k_{max}, where the Reynolds number is approximately equal to one and viscous dissipation becomes relevant. The intermediate range of validity in k-space, from $2\pi/L$ to $2\pi/\tilde{\ell}$, is called the inertial range, where L is the channel size and $\tilde{\ell}$ is the dissipation length scale. At the dissipation length scale the Reynolds number will be reduced to $Re_\ell = \mathcal{O}(1)$.

Inside this specialized regime of the turbulent energy spectrum, the energy density at any given k value should depend only on the wave number and the rate of energy dissipation, defined as ϵ. This assumption is valid because we are examining the turbulence in the inertial regime where the high Reynolds number dictates that viscosity and internal stresses are not primary effects. Therefore E can only be functionally dependent on these variables, or

$$E(k, \epsilon) = Ck^{\alpha}\epsilon^{\beta}.$$

Here α and β are arbitrary constants which must be worked out to match the units of E. A dimensional argument can be made for the spectrum of the energy, namely that given the dimensions of k and ϵ, only certain values for the exponents α and β are allowed. A possible configuration for the system is

$$E(k, \epsilon) = Ck^{-5/3}\epsilon^{2/3}. \tag{1–8}$$

This is the famous Kolmogorov spectrum, the spectrum will prove to be an important starting point for the study of energy decay in quantum (as well as classical) turbulence. To further understand the quantum system a sound foundation in liquid helium is required.

1.3 Superfluid Helium 4

The element of helium is both extremely light and inert. It belongs to the nobel gas column in the periodic table and is not reactive. It has a very weak electro-magnetic interaction with other elements, including itself. Under normal conditions, it does not

form molecules and only interacts through the Van der Waals dipole forces. Helium has a low mass which gives it a relatively high RMS velocity at every temperature. These properties combine to push the saturated vapor liquefaction temperature of helium down to 4.2K. In addition to the low lignification temperature, it will not solidify at ambient pressure, even at absolute zero. To form a solid, pressure higher than 25 bar is required. Below $2.17K$, where the zero point quantum energy is greater than either the thermal or electrical interaction energy of helium, the fluid passes through a second order phase transition from a classically defined fluid into an entirely new quantum state. The second order phase transition that helium passes through is observed by a discontinuity in the first derivative of the thermodynamic free energy which describe the fluid state. For second order transitions, there is no release of energy in the form of latent heat, but there are sharp features in many properties, such as specify heat. For helium, this is famously seen as a infinity in heat capacity at the lambda point.

The phase diagram of helium is shown in Figure 1-1. The low temperature phase of helium is commonly referred to as superfluid helium or as helium II. The name superfluid is due to helium's vanishingly small kinematic viscosity which makes it flow like a *super*fluid. The minuscule or vanishing viscosity is the property that produces the high Reynolds number flows relative to classical fluids. A chart of kinematic and effective kinematic viscosities is shown in Table 1-1 [5]. Helium II sets the bottom of this chart, but it shares its vanishing viscosity with the other quantum fluids. These include the lighter isotope of helium, helium 3, and the various Bose-Einstein condensed gasses. Each of the quantum fluids has a vanishing classical viscosity, but contains a finite 'effective' viscosity. For quantum fluids the source of the viscosity is different than that of a classical fluid and is entirely absent during laminar flow. The low viscosity of helium II, for turbulent flow, instigated its use as a test fluid.

The information in Table 1-1 begs an interesting question: how can a superfluid show any viscosity? The previous definition states 'a superfluid flows without resistance',

Table 1-1. Kinematic Viscosity of Different Fluids

Material	Kinematic Viscosity	
Air	$1.9 - 254 \times 10^{-6}$	m^2/s [6]
Compressed Air	$1.1 - 1,000 \times 10^{-7}$	m^2/s [5]
Water	$2.9 - 17.87 \times 10^{-7}$	m^2/s
Freon,	$1.9 - 3.1 \times 10^{-7}$	m^2/s
Mercury	$6.7 - 12.4 \times 10^{-8}$	m^2/s
Liquid Helium	$1.8 - 2.6 \times 10^{-6}$	m^2/s
Compressed Helium	$5 - 10,000 \times 10^{-8}$	m^2/s
Superfluid Helium	$1.0 - 200 \times 10^{-11}$	m^2/s [7]

implying zero viscosity. How can both of these statements be true? The answer is, lies in how one measures the viscosity and in what situation it is measured. The first measurements on the viscosity of helium II, which showed a zero viscosity, were done by attempting to measure the pressure drop of He II in Poiseuille flow (forced flow through a pipe). These experiments produced a value of viscosity which was vanishingly small and are shown in Figure 1-2 [8]. The viscosity in this figure is calculated by taking the derivative of velocity with respect to the applied pressure across the channel. For Poiseuille flow, a zero slope means that the flow velocity through the channel is independent of applied pressure and that there is zero shear force on the liquid from the walls. However, when the viscosity of helium is measured by a different mechanism, the results are startlingly different. These are shown in Figure 1-3 [9]. These data are from the famous experiment where a torsional disk is rotated in a bath of superfluid helium and the change in natural frequency is measured. For this experiment the viscosity is inferred from the amount of fluid dragged by the oscillator. The difference between these two experiments is subtle. Both try to measure the ensemble fluid viscosity, but are in fact are measuring it in two distinct components of superfluid helium. Figure 1-2 shows a diminishing viscosity with temperature while Figure 1-3 shows a sharp rise in viscosity as a function of the temperature. These seemingly opposing measurements are due to the different measurement techniques. In the Poiseuille flow experiments, the measured quantity is the shear of the superfluid with the capillary walls, while in the rotating disc

experiment the increasing mean free path of the excitations in the superfluid bulk are measured. These experiments led to the empirical two fluid model where helium II is composed of 2 interpenetrating fluids with different properties.

The separation of "normal" and "super" is the foundation of the two fluid model. This well known phenomenon (shown in many helium texts such as Wilks and Betts [10]) shows that below the lambda transition (at $\sim$ 2.17K), the relative density of normal fluid monotonically decreases as the superfluid component increases keeping the total relative density always equal to 1. The theoretical basis of the two fluid model of liquid helium was first proposed by Tiza in 1938 to explain several strange behaviors, such as the loss of viscosity, thermo-mechanical effect and various sound modes. The two fluid model results from the assumption that only eight variables are needed to define a complete set of parameters to describe the hydrodynamic properties of superfluid helium II. The description and solution for the model was first proposed by Landau [11] and is well described by S. J. Putterman [12]. The result of the derivation is the following set of 4 equations,

$$\frac{\partial \rho}{\partial t} + \nabla \cdot (\rho_n \vec{v}_n + \rho_s \vec{v}_s) = 0 \tag{1–9}$$

$$\frac{\partial \rho s}{\partial t} + \nabla \cdot (\rho s \vec{v}_n) = 0 \tag{1–10}$$

$$\frac{D\vec{v}_s}{Dt} = 0 \tag{1–11}$$

$$\frac{\partial}{\partial t}(\rho_n v_n + \rho_s v_s)_i + \frac{\partial}{\partial r_\alpha}(p\delta_{i\alpha} + \rho_n v_{n,i} v_{n,\alpha} + \rho_s v_{s,i} v_{s,\alpha}) = 0. \tag{1–12}$$

The n and s subscripts represent the normal and superfluid components respectively, $\frac{D()}{Dt}$ is defined in Equation 1–2, ρ is the total fluid density including both ρ_s and ρ_n, $\vec{v}$ is the velocity, and Einstein notation is used in the 4th equation.

The two fluid model has found enormous success in the description of the behavior of liquid helium. In essence, it allows each fluid component to behave independently of the another while being contained by the same volume. The two fluid model allows for each component to have its own velocity field and carry a distinct entropy. Therefore, the

superfluid component will move according to a potential flow and will carry zero entropy, and all of the heat energy and "viscosity" are carried in the normal fluid component. There are many well described effects by this model, such as the thermomechanical effect and several sound modes. The thermomechanical effect asserts that changes in temperature can drive a very large change in pressure, and is observed in the form of the fountain effect. The two fluid model also supports several new sound modes, 2nd, 3rd, and 4th sound in addition to the normal pressure waves of 1st sound. Second sound is a transport mode in which superfluid and normal fluid move 180° out of phase, such that there is no or very little change in the ensemble fluid density. Third sound is a mode in which the helium is confined to a two dimensional film and the normal fluid component is locked to the surfaces, allowing a surface wave of pure superfluid to propagate. Fourth sound is the same as 3rd, but with the normal fluid locked into a one dimensional channel. It just happens that the attenuation of second sound waves through vorticity is a sensitive measurement of vortex line density. Second sound is a common measurement tool above 1K and its properties will be reviewed in sec. 1.4.

The two fluid model describes many properties of superfluid helium, but it falls short in some situations. One area in particular exemplifies the insufficiencies of the model. If the superfluid component is truly described by potential flow, then $\nabla \times \vec{v} \equiv 0$ everywhere at sufficiently low temperatures. This leads to a circulation integral of $\oint \vec{v} \cdot d\ell = 0$, implying that circular motion is not allowed and there is no vorticity. Experimental evidence counter to this was shown in an experiment by Osborne [13], where a classical meniscus is seen on a rotating superfluid. The circulation integral dictated by the two fluid model does not allow for a sloped meniscus in a simply connected vessel, such as the rotating vessel in this experiment. Therefore, something must be missing in this 2 fluid model.

A more sophisticated description of the superfluid He^4 was postulated by London. This more formal approach to understanding the behavior of superfluid treats the fluid as

a quantum liquid, complete with a wave function. The existence of a macroscopic wave function with the form

$$\psi = |\psi| e^{iS(\vec{r},t)}, \tag{1–13}$$

was proposed. Here ψ is the wave function and S is the phase. This quantum wave function obeys all the typical properties, including the definition of the velocity operator, $-i\nabla$. Therefore this wave function naturally gives rise to a potential velocity field,

$$\vec{v} = \hbar/m_{He} \nabla S(\vec{r}, t), \tag{1–14}$$

where m_{He} is the mass of a helium atom. The wave function produces a velocity field that is a gradient of a scalar, in this case the phase of the wave function. The brilliance of this formulation is that the velocity field for a superfluid is the natural result of quantum mechanics. Feynman and Osanger in 1955 observed that with this formulation the velocity field is not required to be simply connected [14]. Therefore, two dimensional linear defects in the fluid field are possible and circular flow around these defects does not violate any physical properties and still allows the superfluid to be free of viscosity! In fact the circulation the circulation around a vortex core can be calculated. Given that the wave function of superfluid helium in single valued, if the phase S is integrated in a closed loop around a vortex dislocation the resulting value should be an integer multiple of 2π. Formally this is expressed by the following integral

$$\oint S \cdot d\vec{r} = \oint \frac{m_{He}}{\hbar} \vec{v} \cdot d\vec{r} = \frac{m_{He}}{\hbar} \kappa = 2\pi, \tag{1–15}$$

where $\kappa \equiv \oint \vec{v} \cdot d\vec{r}$ is the circulation. Following from Equation 1–15

$$\kappa = \frac{nh}{m_{He}}, \tag{1–16}$$

where n is the quantum number for the circulation. In all experiments n has been found to be equal to exactly 1. Vortex lines and their dynamics are discussed in section 1.5. After the second sound technique is described in Section 1.4.

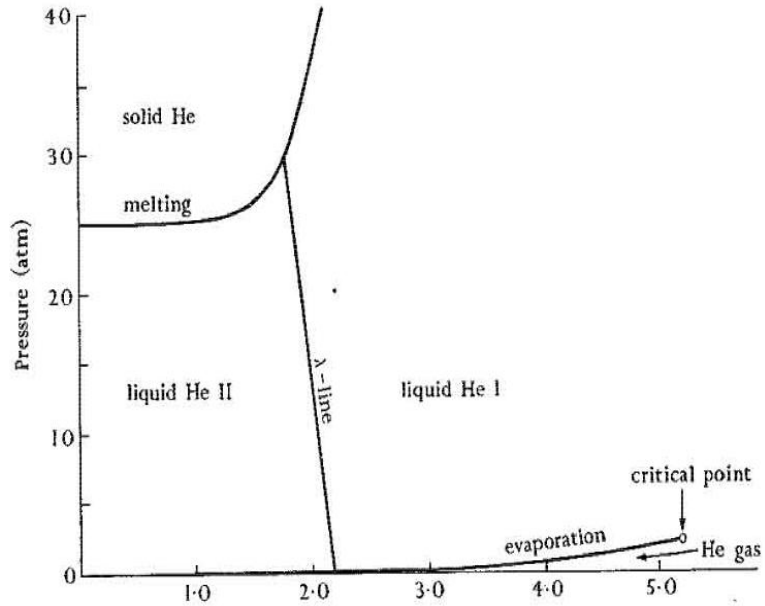

Figure 1-1. The low temperature phase diagram of helium 4. Reprinted from London, F. London, Superfluids: Macroscopic theory of superfluid helium, Structure of matter series. [15].

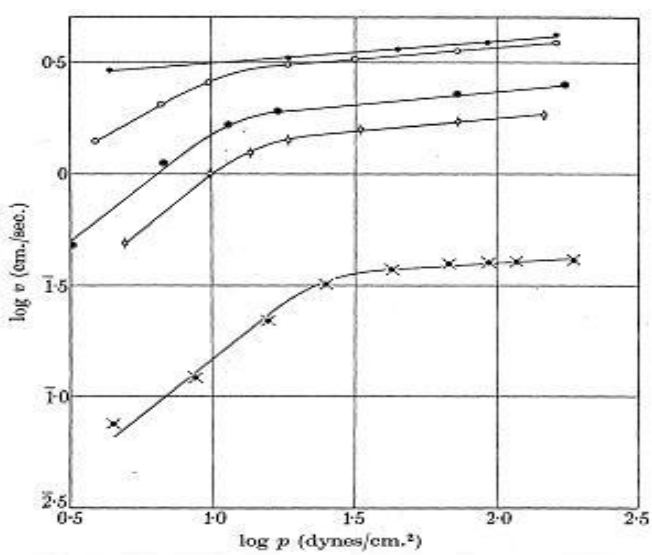

Figure 1-2. Poiseuille helium flow in a small capillary. This figure shows a clear increase in flow velocities through a small channel as a function of applied pressure when the temperature of the helium bath is lowered. The lower temperature data (1.164 K) are presented in the top of the figure and the temperature increases until the bottom set of data (2.162 K). This implies that the viscosity of helium decreases as a function of temperature. Reprinted from Misener, J. Allen, D. Misener, Royal Society of London Proceedings Series A 172, 467 (1939) [8]

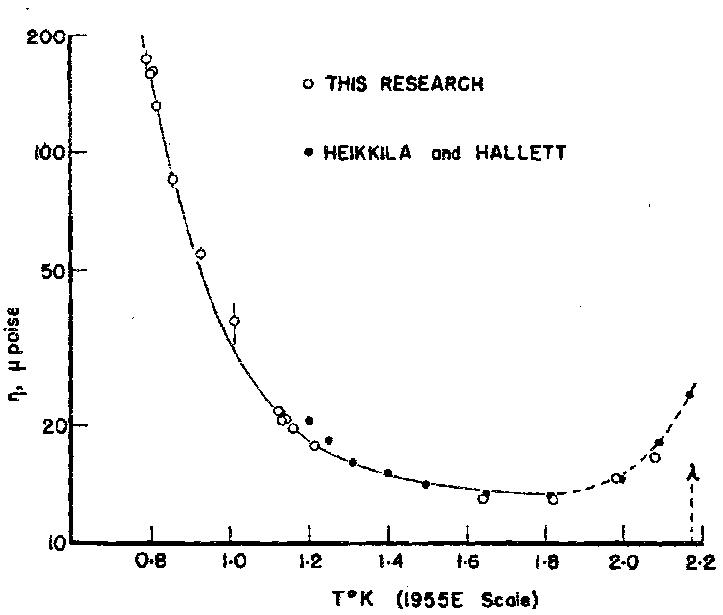

Figure 1-3. This plot shows the normal fluid viscosity as a function of temperature in a rotating body of superfluid helium. This data is in direct opposition to the decreasing viscosity shown in the previous figure. Reprinted with the permission from NRC research press, Canadian Journal of Physics 41, 596 (1963) [9].

1.4 Second Sound

Perhaps the best use for any theory is the ability to predict new phenomenon. For the two fluid model, the first instance of this was the observation of sound modes. After the two fluid model was presented by Tisza [16] in 1938 and later formalized by Landau [11] in 1941, different sound modes in helium II were detected by Peshkov [17] in 1944. This provided strong evidence supporting the two fluid theory in this particular situation. In addition to confirmation of earlier ideas about the properties of helium, second sound has turned into a strong tool to study vortex dynamics. Once again, following Putterman, we can linearize Equations 1–17 - 1–20 for the situation of small pressure and entropy changes relative to their absolute value. This is the case for sound. Following from this we obtain a closed set of 4 equations to describe the second sound mode,

$$\frac{\partial \delta\rho}{\partial t} + \nabla \cdot (\rho_n \delta\vec{v}_n + \rho_s \delta\vec{v}_s) = 0 \tag{1–17}$$

$$s_o \frac{\partial \delta\rho}{\partial t} + \rho_o \frac{\partial \delta s}{\partial t} + \nabla \cdot (\rho_s \delta\vec{v}_n) = 0 \tag{1–18}$$

$$\frac{\partial \delta\vec{v}_s}{\partial t} - s_o \nabla \delta T + \frac{1}{\rho_o} \nabla \delta p = 0 \tag{1–19}$$

$$\rho_{n,0} \frac{\partial \delta\vec{v}_n}{\partial t} + \rho_{s,0} \frac{\partial \delta\vec{v}_s}{\partial t} = -\nabla \delta p. \tag{1–20}$$

The zero subscript denotes the equilibrium states in which the sound propagates.
All of the equations are expanded to the first order of the small pressure and entropy fluctuations. Simultaneously solving these four relations for traveling longitudinal waves reveals two distinct sound modes, one with a velocity $u^2 = u_1^2 + \frac{u_1^2 u_2^2}{u_1^2 - u_2^2}(1 - C_v/C_p)$ and the other, $u^2 = u_2^2 + \frac{u_1^2 u_2^2}{u_1^2 - u_2^2}(1 - C_v/C_p)$. The parameter 1- C_v/C_p is almost always a very small number ($\sim 10^{-3}$), as the difference between constant volume and pressure specific heat is small. Therefore the sound modes are often only examined in the first order, or $u = u_1$ or u_2. As it turns out in u_1 the superfluid and normal fluid components travel in phase, much like classical sound, and in u_2 the two components travel out of phase. This is the new and unique second sound mode.

The absorption of second sound is commonly used [18, 19] and is a sensitive tool [20] to determine the the vortex line density in a volume of quantum turbulence. The measured line density, L, can be related to the vorticity ω of the volume by the equation,

$$\omega = \kappa L. \tag{1–21}$$

This equation is known as Feynman's rule [21]. For example, if one vortex line ($L = 1 cm\ line/cm^3$) with circulation ($\kappa = 9.97 * 10^{-4}\ cm^2/s$), is stretched across a 1cm sample volume, the vorticity of the volume is $L \times \kappa = 9.97 * 10^{-4}\ Hz$. This is the equivalent of classically rotating the same cell once every 17 hours. Therefore, for any but the slowest of rotations many vortex filaments will span a superfluid container.

Second sound is attenuated by several different means other than the interaction with vorticity, such as viscous bulk and surface losses. To account for these losses in the line density measurements, a calibration in quiescent fluid is required. The calibration is conducted by exciting a standing wave in the experimental cavity and scanning frequencies around the resonance peak. From the resonance, the Q or quality factor, is determined by taking the ratio of the resonant frequency to the width of the resonant peak, measured as the full width at half maximum of the resonance response. Q is a measure of the ratio of energy stored in the oscillator to the energy dissipated for each oscillation cycle. Measurements and conclusions from our specific experiments will be presented in the second sound experiment section in Chapter 5.

As fundamental research into the properties of helium progressed Hanson and Pellam completed an extensive experimental study on the attenuation of second sound in 1954 which produced a model for bulk attenuation in the fluid as [22]

$$\alpha_B = \frac{\omega^2}{2\rho v_2^3}(\frac{4}{3}\eta\frac{\rho_s}{\rho_n} + \zeta_{II}\frac{\rho_s}{\rho_n} + \frac{K}{C}). \tag{1–22}$$

Here α is the attenuation of the second sound, ω is the angular frequency, ρ is the density, v_2 is the sound velocity, η is the viscosity of the normal fluid or "ordinary"

viscosity, ζ_{II} is the second viscosity coefficient, ρ_s and ρ_n are the super and normal fluid densities, K is analogous to ordinary thermal conductivity, and C is the specific heat capacity of helium II. The first term in the equation is attributed to Pellam, and is due to the ordinary normal fluid viscosity of helium [23]. The second term is associated with both the normal and superfluid components and is termed second viscosity [24, 25]. The final term is of second order in magnitude and is due to thermal processes in the sound mode. Together they define the bulk helium second sound attenuation.

One of the things to note about this equation is the ω^2 dependence on frequency, which means that as frequency is increased, the attenuation increases at a much faster rate. Also, although temperature is explicitly absent from the equation its effects are still observed by the temperature dependence of sound velocity, fluid viscosity, and relative superfluid density. Therefore, it is favorable to run and calibrate the second sound sensors at a place in the T vs. v plot (Figure 1-4) that has a very small derivative. It is worth noting that there is no sound amplitude dependence on the attenuation (at least for the sound amplitudes used in the study presented in Ref. [22]), so larger amplitude waves are not necessarily more damped in the linear regime.

Dissipation from the vortex interactions and bulk interactions is joined by the surface effects. The surface losses are caused by helium's interaction with its containing vessel. Following from Heiserman and Rudnick [26], the dissipation from the walls can be expressed as,

$$\alpha_S = \frac{B}{4A}\frac{\rho_s}{\rho}\frac{\omega\lambda}{v_2} \tag{1–23}$$

where λ is the characteristic length over which a viscous diffusion wave decays and A and B are geometry specific terms. This factor is typically considered to be a small but measurable contribution to the background attenuation and the final component to the attenuation of second sound. Measuring the total attenuation represented by these terms yields the vortex line density, α_v.

Here second sound is produced by the well established technique of forced oscillation of a porous film. These sensors were made by the same technique as many other detectors [27, 28]. The oscillating film is littered with small pores (about $0.2\ \mu m$ in diameter [29]) through which the superfluid flows unimpeded, while the normal fluid viscosity prevents its transit. The result is thousands on point source second sound waves that travel out into the transducer. After a short distance the waves begin to interact with one another and, by Huygens' principle a plane wave is formed and propagates across the cell. The plane wave amplitude is written as,

$$A(f,\,t) = A_o e^{-\alpha x} e^{i(kx-\omega t+\varphi)}. \tag{1–24}$$

In Equation 1–24, A is the amplitude, α is the total dissipation, x is the distance traveled, ω is the frequency, and φ is the phase. Summarizing the results from Stalp [30] and Swanson [31] we can determine the vorticity in a experimental volume by the attenuation of second sound. If we accept that Equation 1–24 represents the second sound wave amplitude, then after one trip across the cell the amplitude falls to $A(f,\,D/v_2) = A_o e^{-\alpha D} e^{i(kD-\omega D/v_2+\varphi)}$, where D is the distance the wave travels. Assuming that the entire wave front is not absorbed, some of it will reflect off of the detecting sensor and circulate back across the cell. If the sum of all the back and forth reflections are taken into account we arrive at the $t = \infty$ amplitude of

$$A(f,\,\infty) = \frac{A_o}{e^R\left(e^{\alpha_r D+R-iD(\omega/v_2-\alpha_i)} - e^{-\alpha_r D-R+iD(\omega/v_2-\alpha_i)}\right)}.$$

In this equation the attenuation α has been separated into its dissipitive component α_r and its imaginary component that shifts the phase of the plane wave α_i, where $\alpha = \alpha_r + i\alpha_i$. Since it is not the complex amplitude that is experimentally measured by a lock-in amplifier, the magnitude of the signal must be taken by multiplying A by its complex conjugate A^* and taking the second root. The following equation reveals the amplitude of the second sound as a function of frequency and attenuation after this

operation,

$$A(f,\infty) = A_T(2cosh(2(\alpha_r D + R)) - cos(D(\omega/v_2 - \alpha_i))) \tag{1–25}$$

where A_T is defined as equal to $A_o e^R$. More detail on these derivations can be found in the work of Stalp and Swanson [30, 31].

The attenuation of second sound is the linear sum of the three processes, $\alpha = \alpha_v + \alpha_B + \alpha_S$. If we assume surface losses are insignificant in the same vain as Stalp [30] or that it is unchanging with vorticity and can therefore be grouped with the bulk losses, we can solve for the vorticity as a function of second sound amplitude. can be explicitly solved for. The amplitude as a function of vortex line density is

$$A^2 = A^2_{L=0}\frac{1 - cos(2\pi D f_r/Qv_2)}{cosh(2(\alpha_B + \alpha_v)D + 2R) - 1}. \tag{1–26}$$

$A_{L=0}$ is the resonant amplitude with zero vortex line density. The vortex line attenuation amplitude can be found, giving the vorticity as a function of measured amplitude [30]

$$\alpha_L = \frac{1}{2D} ln[\frac{1 + (A_o/A)^2 C + \sqrt{2(A_o/A)^2 C + (A_o/A)^4 C^2}}{1 + C + \sqrt{2C + C^2}}], \tag{1–27}$$

where $C = 1 - cos(2\pi D\Delta_o/u_2)$. In addition to acquiring the second sound attenuation, the relationship between homogenous and isotropic vorticity and second sound attenuation is well known from the works of Hall and Vinen [32, 33],

$$\omega_{rms} = \frac{16 v_2 \alpha_v}{\pi B}. \tag{1–28}$$

Here B is the temperature dependent mutual friction parameter and ω_{rms} is the root mean square vorticity, what we seek to determine.

Mutual friction is the dissipative source that occurs as a result of excitations in helium (rotons and phonons) scattering off of vortex cores. The equation describing mutual friction is [21],

$$f_D = -\alpha\rho_s\kappa\vec{s'} \times [\vec{s'} \times (\vec{v_n} - \vec{v_{sl}})] - \alpha'\rho_s\kappa\vec{s'} \times (\vec{v_n} - \vec{v_{sl}}). \tag{1–29}$$

Where v_{sl} is the local superfluid velocity, $\vec{s'}$ is the unit vector along the vortex core, and α and α' are empirical parameters. α includes the the parameter B in the second sound equation by the relation $\alpha = B\rho_n/2\rho$.

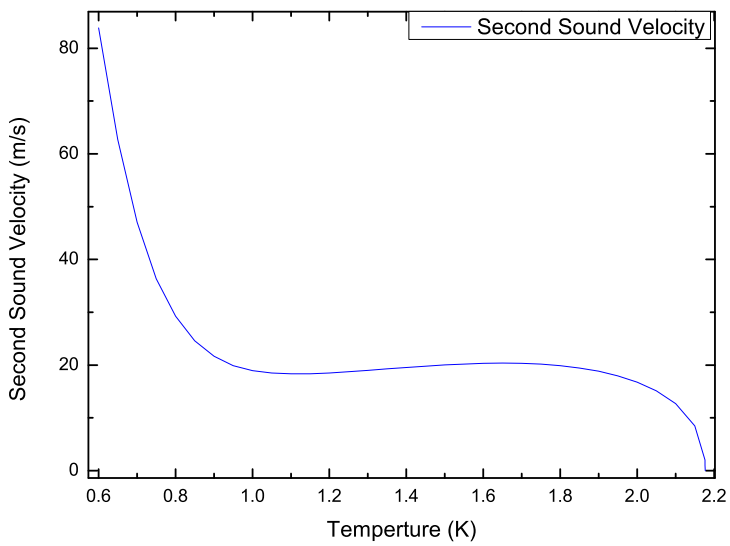

Figure 1-4. This plot shows the dependence of second sound velocity on temperature [34].

1.5 Quantum Dynamics

Second sound as a measurement tool is important for one of the studies reported in this dissertation and for several projects underway (see Chapter 5). However, at millikelvin temperatures, this tool is unavailable, due to the lack of normal fluid, and a different type of experiment, with different dynamics is investigated. While many aspects of fluid motion change in the low temperature limit, notably the loss of mutual friction, between the superfluid component and normal fluid component, the fluid kinetic energy is still contained inside the vortex bundle and is measured, to first order, by the integrated vortex line length. This measurement is to first order because of the overlapping flow fields around different vortex lines. The kinetic energy for a single, isolated, quantum vortex line per unit length is obtained by integration of the fluid's kinetic energy per unit line length along its vortex core, $Ke = \int_a^b \frac{1}{2}\rho v^2 dr^2$. For superfluid helium this is becomes

$$K.E. = \frac{\rho_s \kappa^2}{4\pi} ln(\frac{b}{a}), \tag{1–30}$$

where κ is the circulation, b is a length (such as the experimental cell diameter), and a is the core radius. The vortex line energy, to first order, is directly proportional to its length, with the higher order terms depending on the interaction between the velocity fields of one or more vortex lines. Therefore, for the vortex array to be in its ground state the total line length of the system must be minimized. The decrease in kinetic energy when the vortex tangle is moved into its shortest integrated length state is the driving force for energy decay in quantum turbulence.

The proportionality of line energy to line length has two consequences which drive the motion. These are a restoring force against deformations along the vortex core and vortex line reconnections as two vortices interact at close range. Both of these phenomena are present in classical fluids, but are not typically important in the decay of energy due to the viscous energy channel. A vortex line reconnection is the interaction between two separate vortices as they come into close proximity to each other. The

line reconnection is a distinct topological change in the fluid which has been recently experimentally observed by a group at Maryland [35]. It occurs as two different vortex lines or two parts of the same vortex line cross paths. In this event, it is energetically favorable for the two lines to break apart at their intersection and reassociate with the other line. Both lines break in half, changing the topology of the tangle, and reform with two lines interchanging a portion of their length and reducing the total line length of the system as a whole. This process is shown in cartoon form in Figure 1-5. This process produces a very sharp kink along the vortex line, which is paramount in the transport of energy in quantum turbulence. The sharp kink excites wave modes on the vortex core, which have been shown to have interesting properties. Reconnections fundamentally change the topology of the tangle, but more importantly for turbulent decay, they have the ability to produce sharp kinks on vortex lines. The propagation and effect of the vortex waves will be expanded below when we discuss the restoring forces on the line. Although vortex line reconnections are a known phenomenon, they are still a challenge for theorists and particularly for computations to contend with in turbulence. The difficulty for simulations is shown by the changing critical distance with which lines reconnect [36–38] which is inserted *ad hoc* differently for different research groups. Remarkably though, if the work is done with the entire non-linear Schrodinger or Gross-Pitaevskii equation reconnections naturally arise [39].

During reconnection, the overall line density of the tangle decreases, the loss of kinetic energy through the production of phonons. Leadbeater *et al.* studied this problem by simulating the reconnection of two ring vortices and determined that the energy given to phonons depends strongly on the orientation of the vortex rings. Specifically, the loss of line length is $\sim tan^2(\theta/2)$ [40], where θ is the angle between circulation and the axes of the ring. The angular dependence is due to the need for the vortex lines involved in the reconnection to locally orient themselves such that the connecting parts are parallel and therefore their velocity fields will exactly cancel during the reconnection event. The

energy lost to phonons by this process is not large relative to other possible dissipation sources. Therefore, reconnections are not thought to directly effect the turbulent dynamics unless there is a very large vortex line density and a glut of reconnections.

Vortex line reconnections also occur in classical fluid dynamics, although their properties are substantially different. For classical flows, the reconnection process seems to not only involve but depend on the fluid viscosity, which is absent in a superfluid. A particular report on classical fluids states "*This reconnection process cannot be captured by vortex methods which use continuous filaments for a description of inviscid flow [41], since without viscosity the vortex tube retains its identity for all time. In order for reconnections to occur dissipative effects must be considered.* [42]" This is a most interesting point, since many early quantum turbulence simulations explicitly use continuous filaments with reconnections added in *ad hoc*. Vortex reconnections in superfluid helium are not entirely understood on the most fundamental level, but their effects in quantum turbulence are immense and, without attention to detail, one may lose the connection with classical fluid research. Finally, the sharp deformations along the vortex lines will be investigated. These kinks produce non-linear wave modes along the vortex core itself due to the straightening force on the lines.

The restoring force on a vortex core is a special case of the classically known magnus force, where a vortex is influenced by an external velocity field or two vortices are influenced by each other's velocity field. The magnus force is classically written as $\vec{F} = -\rho\vec{\kappa} \times \vec{V}$, where κ is the circulation and V is the velocity field around the core. For superfluid helium this is equal to,

$$\vec{F} = \vec{f} + \rho_s \kappa \hat{\kappa} \times (\vec{v_L} - \vec{v_s}), \tag{1–31}$$

where κ is h/m, $\hat{\kappa}$ is the unit vector along the length of the vortex, $\vec{v_L}$ and $\vec{v_s}$ are the vortex line velocity and the superfluid velicity respectively, and $\vec{f}$ is the mutual friction force of the vortex in the flow [43]. When the force experienced by the vortex line is due

to a different part of the same vortex filament, the local velocity field can be given by the Biot-Savart law,

$$\vec{L}(\vec{r_o}) = \frac{\kappa}{4\pi} \int \frac{(\vec{r} - \vec{r_o}) \times dr}{|(\vec{r} - \vec{r_o})|^3}. \tag{1–32}$$

The position $\vec{r}$ and the integral are taken along the length of the vortex. The integral diverges for $\vec{r} = \vec{r_o}$, but is accounted for by the finite size of the vortex core. The self-induced flow is important in the dynamics of superfluid turbulence, because it can be shown that the Biot-Savart force supports the propagation of helical waves along a vortex core. Called Kelvin waves, these are a very important path for the transport of kinetic energy for superfluid turbulence decay. This wave form and its dispersion were expressed by Lord Kelvin in 1880 [21, 44].

Equation 1–32 can be expanded for local deformations of the vortex core where $\vec{r}$ and $\vec{r_o}$ are similar. In this case the integral reduces to only the local contributions

$$\vec{v_s}(\vec{r_o}) = (\kappa/4(\pi R))ln(R/a_o), \tag{1–33}$$

Here R is the local radius of curvature of the vortex core and a_o is the core diameter. Equation 1–33 shows that small values of R are associated with large line velocities. Therefore, the two processes described in this section strongly interact in the dynamics of the fluid. Specifically, a reconnection event between two separate or two parts of the same vortex filament creates a sharp kink in the vortex tube, which then induces a high velocity motion on the vortex core due to the magnus effect. This in turn instigates more reconnections due to the increased motion and so on as a cascade process. Once the motion is established, non-linear Kelvin waves are able to transport the energy to different wave numbers along the vortex core in a process eerily similar to the Richardson cascade in the Kolmogorov spectrum.

The series of processes outlined are believed to be very important to the decay of energy in quantum turbulence, particularly in the zero temperature limit. As was described in Sec. 1.2, the energy spectrum of classical turbulence is thought to be

spread out all over the inertial regime. Upon reaching a high wave number, viscous effects become dominant. But in a superfluid, viscous effects should be irrelevant. This means that turbulence is unable to decay. However, there are other processes unique to quantum fluids that take place. The general consensus in the community is that for most types of turbulence a second, different, cascade takes over at the end of the Richardson cascade and carries the energy to even higher wave numbers. The Richardson cascade is the process by which the Kolmogorov spectrum arises. The idea of a cascade of Kelvin waves was first proposed by B.V. Svistunov in 1995 [45], and was followed by W.F. Vinen's suggestion that at extremely high wave numbers the energy on the vortex could be radiated as phonons [46, 47].

The second energy cascade present in quantum turbulence is an energy transport along the vortex lines themselves. The mechanism that carries the kinetic energy is the kelvin wave distortions of the vortex line. The cascade proceeds according to the following scheme: Bundles of vorticity travel through the superfluid until they encounter another traveling vorticity bundle. Upon meeting, several vortex filaments cross paths and perform reconnection operations. Sharp kinks form along the vortex core and initiate motion of individual vortices inside the vortex bundle due to the magnus force. The vortices in a single bundle then acquire the impulse to move and begin reconnecting with their neighboring vortices. This process further kinks the filaments, sending energy to increasingly higher wave numbers, until the vortex lines reach a point where they have such a large amplitude of curvature that reconnections with themselves become the most important process. Once the cascade of reconnections has seeded the vortex core with many and high momentum wave modes, the non-linear kelvin waves are able to move the energy into still higher values of k to eventually be radiated as phonons.

For each reconnection event and the subsequent Kelvin wave cascade, the vortex core is set in oscillation along with the superfluid surrounding it. This process creates sound wave quanta in the superfluid, or phonons, which are able to radiatively reduce

the kinetic energy of the system. It is only at the extremely high wave numbers that the phonon radiation is efficient enough to carry away substantial energy. It is not surprising that large wave numbers are needed to efficiently radiate the energy because in superfluid helium most of the energy contained in phonons are associated with the highest energy modes [10].

The above theoretical frame work is nearly universally accepted for moderate tangle densities. However, for low density turbulence, such as that due to vibrating wires or quartz tuning forks, diffusive decay through the emission of vortex rings is also a possibility [48]. For high density turbulence sound emission directly from reconnection events could also be a relevant decay channel. There is little coconscious about the properties of the momentum regime where quantum energy and classical energy have comparable magnitudes. This process is still up for debate with no strong consensus in the community [49, 50].

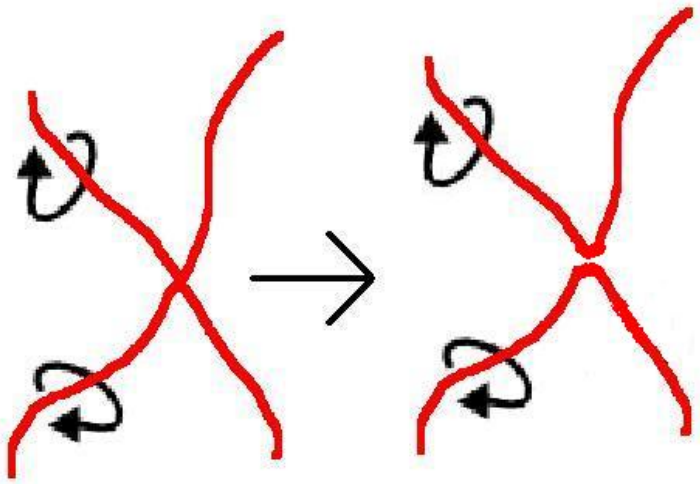

Figure 1-5. This shows a cartoon of two vortex lines reconnecting. After the reconnection two new vortices are formed, each with a sharp kink at the location of the vortex crossing location.

1.6 Calorimetry

One measurement tool that is unavailable at low temperatures is thermometers (see Capter 2). Due to the exceptional decrease in the heat capacity of helium below $1\ K$, the heating that arises as a result of turbulent motion can be measured as a temperature rise. This was first pointed out by Samuels and Barenghi [51] for a non-classical flow, but the idea is well suited for grid turbulence. To understand this it is important to know how the energy travels through the turbulence as a function of time. Similar to the derivation of Kolmogorov spectrum in momentum space, an equivalent dimensional argument can be made for the energy transport in real space. For turbulence generated at a scale much larger than the dissipation scale, it can be assumed that the majority of the energy resides in eddies with a characteristic size D which is on the order of the size of the eddies. These eddies will have a characteristic velocity U, and the energy per unit mass of the system will therefore be

$$E = U^2/2, \tag{1–34}$$

If we assume the the dissipation of energy at low scales in the form described by Vinen and Neimela [43],

$$\varepsilon = \nu'\kappa^2 L^2. \tag{1–35}$$

This equation can be compared to the the derivative of Equation 1–34 to show that the vortex line density should decay with the form of

$$L = \frac{2D}{\kappa\sqrt{\nu'}}(t + t_o)^{-3/2}. \tag{1–36}$$

If all of these equations are combined we are left with the energy as a function of time,

$$E = \frac{2D^2}{(t + t_o)^{-2}}. \tag{1–37}$$

These equations, based on the known information about quantum turbulence, should be approximately accurate. This implies that the dissipation of energy should be,

$$Q = \frac{-4D^2}{(t + t_o^{-3})}. \tag{1–38}$$

1.7 Scope of Work

This dissertation concentrates on the creation and measurement of quantum turbulence by novel processes. The first half of the dissertation, comprising of Chapters 2 and 3, describe work completed towards the goal of creating and measuring turbulence. Many of the techniques and apparatus described in Chapters 2 and 3 were developed as collaborative efforts between the Ihas research group and various other research groups around the world. They were created with the hope that the developed technology would be implemented in a wide ranging set of different experiments.
The latter portion of the dissertation, comprising of Chapter 4, is a review of the measurements on quantum turbulence carried out at millikelvin temperatures. The dissertation will conclude with final thoughts on ongoing and possible future directions for continued work on the techniques described in this work.

CHAPTER 2
SENSOR DEVELOPMENT

The defining equations of fluid dynamics are mathematically intractable, therefore progress in experimental fluid dynamics is dictated by the pace of innovation. Fluid dynamics is a sensor driven field where sophisticated probes are used to probe both the small, and large scale structures of particular flow patterns. To study classical viscous fluids, arrays of pressure, temperature, and velocity sensors are common place. By using many sensors, structural information about the flow is gleaned from fluid property correlations in time and space. The correlations are analyzed to 'visualize' the flow on all length scales. In addition to these indirect measurements, test fluids can be seeded with dyes or neutrally buoyant particles which can be directly visualized and tracked as the fluid travels. Entire conferences and journals are dedicated to not only the fluids being studied, but also the techniques used to study them. However, very little of the instrumentation common to studying classical fluids can be directly applied to the inviscid superfluid Helium 4.

Many of the interesting features of helium dynamics occur at extremely small length scales and are therefore difficult to measure. For example, the large Kolmogorov inertial range (discussed in Section 1.2) is only of experimental interest if we can probe the small length scale and large wave number properties. Otherwise, the additional dynamic range is of limited use. In addition, the interesting quantum physics occurs on the length scales of the vortex cores and their respective bundles. Therefore, for the in-depth study of quantum turbulence, very small sensors with short time constants are needed. In addition to the size requirements of the sensors, the rigors of low temperature research are quite demanding on the instrumentation. The primary concern with instrumentation at millikelvin temperatures is heat load. Specifically, at very low temperatures thermal heat capacities of materials tend to diminish, and therefore all of the sensors used to measure helium need to be run on very small power loads. In

addition to the specific heat of low temperature materials, superfluid helium is a nearly prefect conductor of heat, it is therefore impossible to measure fluid flow velocities by classical hot wire techniques. Helium is also one of the lightest elements, making it very difficult to produce small neutrally buoyant particles to be used in light scattering and other visualization techniques. Overall, helium is a difficult material to work with and to study.

Traditionally, bulk rather than local fluid properties are measured in superfluid helium, using comparably larger and more well-developed sensors. For example, second sound is a measure of the *average* vortex line density of a helium sample across the entire cross sectional area of a sensor, typically of order 1 cm^2. At lower temperatures, a similar averaged vortex line density measurement is accomplished using ionized particles. The particles propagate through a sample filled with turbulence, and the total scattering of the ions by the fluid flow is measured. The integrated scattering and trapping of the ions are converted into the average line density. Sensors like these are not able to resolve the vorticity on a small local scale, but rather measure the average properties over the entire volume encompassed by the sensor. These are powerful tools, but microscopic scale detail, observed in classical flows, is absent. However, we have continued with the help from our collaboration to build and test global property sensors, such as modular second sound transducers.

Thermometers are another sensor useful at low temperatures. In many ways, thermometry is a more powerful tool for quantum fluids than classical ones. This is because at low temperatures, small changes in energy can be measured as comparably large changes in temperature, whereas at higher temperatures the elevated heat capacities of materials require larger energy changes to alter the temperature. However, in other ways thermometry is not well suited for dynamic measurements at millikelvin temperatures because commercially available, typical thermometers require integration times of 10's of seconds to upwards of several minutes to obtain precise readings.

The long equilibrium time required for these sensors tend to mask the local dynamic nature of the fluid, and therefore the quick temperature changes which correspond to fast fluid motions and small scale dynamics are lost. This process makes industrial thermometry non-ideal for our work and has led to the development of our own sensors in collaboration with the Institute of Semiconductor Physics in Kiev, Ukraine, discussed in Chapter 2.

A slightly more localized probe is a pressure sensor. These are common techniques in classical hydrodynamics, but have not been fully developed and made commercially available for work in superfluid helium in the low temperature limit. Pressure sensors have been successfully used in pitot tube gauges at temperature near and below the superfluid transition ($\sim 1.4K$) [52, 53]. These sensors are expensive and still very large compared with the smallest scale motion of interest but have shown promise. In collaboration with the Chan research group, formally at the University of Florida, we have designed and tested miniature MEMS pressure sensors.

Other localized probes are small oscillating objects for the detection of turbulent fluid properties. Both vibrating quartz crystals and vibrating wires are used as a measure of vorticity, and these sensors have found common use in helium 3 turbulence experiments as well as helium 4. The vibrating wires were first used to detect the quantization of circulation [32] and have been used as a sensitive probe ever since. These have found use in many locations including the University of Lancaster, Osaka City University, and Charles University [54–56]

The final technique used to observe turbulence is through visualization. Helium is often visualized by intermingling solid hydrogen globules or hollow glass balls in liquid helium and scattering laser light from the impurity surfaces to form an image of the fluid flow. These techniques are derived from the imaging techniques of classical fluids and have observed some interesting behaviors [35, 57]. Many problems using this technique, with liquid helium. Two of the problems are; matching seed particle density

to that of helium and arranging an optical system and cryostat so that three dimensional images can be recorded. Therefore a new visualization technique is being developed, in collaboration with Yale University and the Manchester University, using optically excited helium molecules to trace the fluid flow [58].

2.1 Second Sound

Second sound, as mentioned is a common technique used to probe the bulk properties of helium. It is a sensitive probe to study turbulent energy decay. The literature is filled with second sound experiments and transducer designs [27, 59, 60]. The method of oscillating a porous membrane was first proposed and tested by Sherlock and Edwards [61] to produce and detect the presence of 2nd sound in helium. A modular second sound transducer was developed through our collaboration with Yale University and is shown in Figure 2-2. These second sound transducers produce the sound mode by oscillating a metal coated porous film by an alternating current. The porous film is a 5-25 μm thick polycarbonate filter paper with 0.2 μm holes which is coated with a thin layer of metal. The films are mounted on a poly carbonate ring and stretched across the transducers shown in Figure 2-1. Pairs of these transducers, mounted 1 cm apart across a flow channel, have been used in two experiments: optical experiment to visualize superfluid helium flow and a grid-pull experiment to measure the vortex line density produced. The mount for this second sound transducer is shown in Figure 2-2 along with the machine drawings for the experimental cell (in the appendix), Figure A-10, and the electrical diagram Figure 2-3.

The transducers used in a resonant configuration with one as a drover and the other as detector of the plane wave activity inside, was cooled below the lambda transition to scan for second sound resonances; a typical frequency scan is shown in Figure 2-4. The pertinent parameters of the second sound sensors are summarized in Table 2-1. The relative signal magnitude for the resonant peak at $\sim$ 26,000 Hz is shown in Figure 2-5 as a function of d.c. bias voltage and in Figure 2-6 as a function of peak to peak

Table 2-1. Second sound transducer

Parameter	Value	
Pore size	0.2	μm
Sensor diameter	0.16	$inch$
Gap between speaker and microphone	0.8	$inch$

oscillator drive voltage. These calibration data were used to pick the parameters for an experiment on the decay of vorticity after a linear grid pull above 1 K. This experiment is introduced in Chapter 5

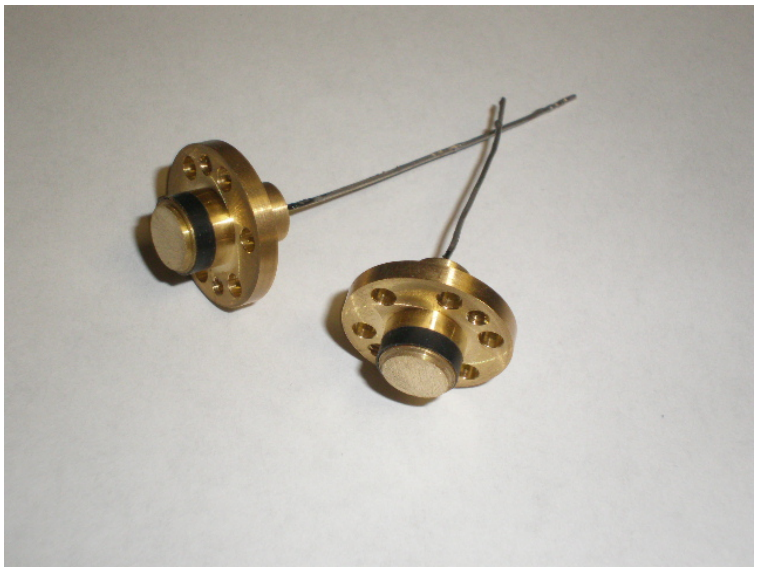

Figure 2-1. This figure shows two second sound transducers, one will operate as a speaker of sound, while the other is a microphone. A porus film is stretched across the brass electrode to produce the sound.

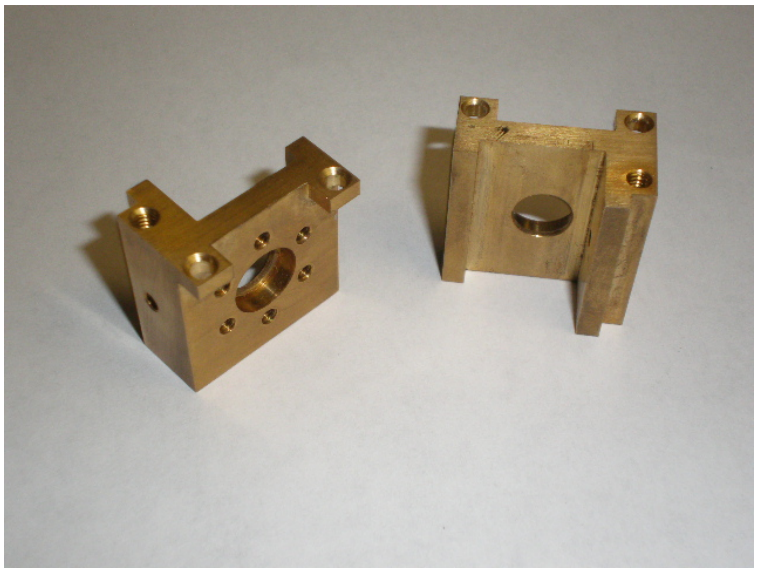

Figure 2-2. This is a photograph of the frames in which the sound transducers are mounted. The square channel inside the mounts is the sample space where turbulence is created.

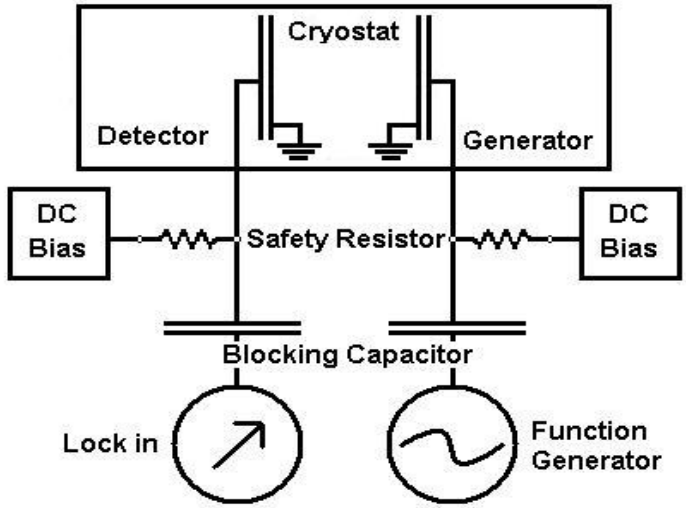

Figure 2-3. This is a electric diagram of the second sound generation and detection apparatus.

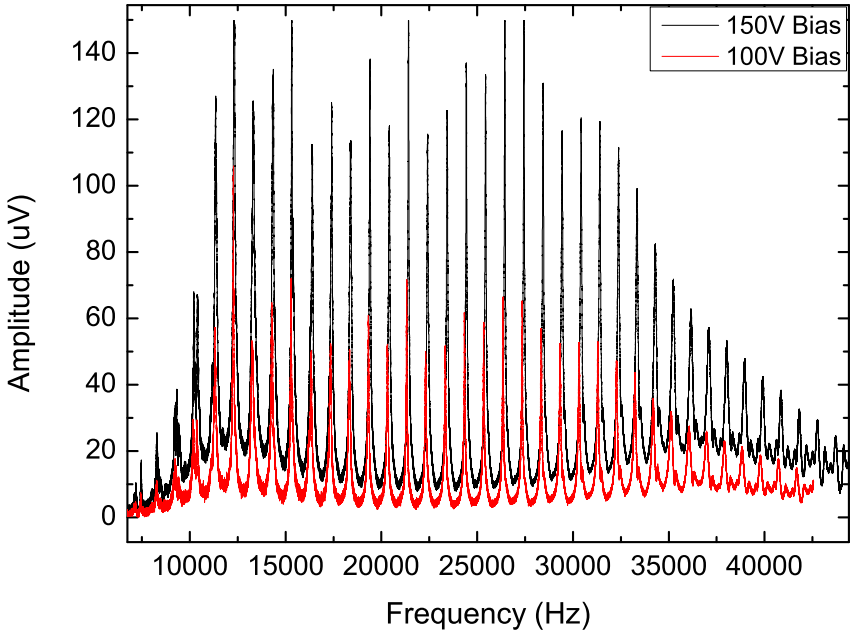

Figure 2-4. This figure shows a scan across a wide range of frequencies with many second sound resonances. The black curve is for a DC bias current of 150 v and the red is for a bias of 100V. The peak to peak drive voltage used for both of these scans was 2 V.

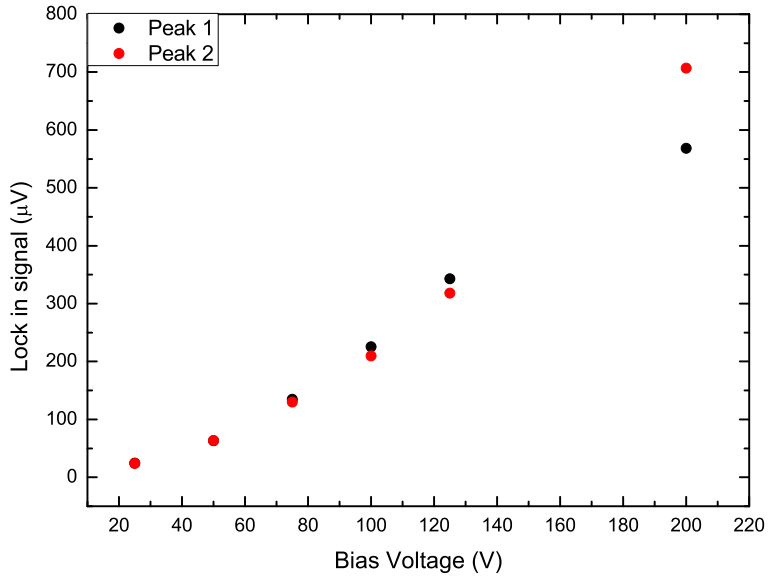

Figure 2-5. This plot shows the second sound signal dependence on the bias for two separate harmonics near 26000 Hz for a peak to peak drive of 6V.

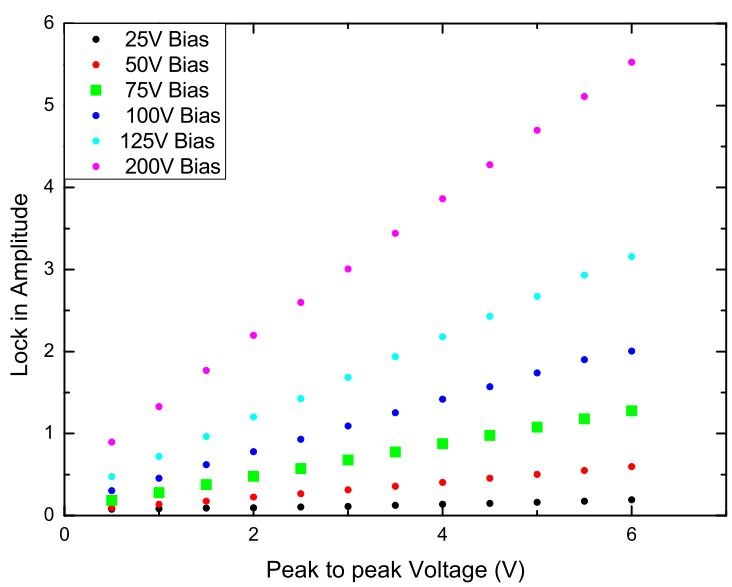

Figure 2-6. This figure shows the second sound resonance response at 26 KHz vs. peak to peak drive voltage dependence for different bias voltages.

2.2 Thermistors

The initial motivation for turbulence research in our group was the measurement of heat release after a turbulent event in a sample of helium. This measurement was to be taken as a function of time with quick responding thermometers. To measure this heat release the thermometers needed to be specifically designed to meet the experimental needs. For this reason a collaborated between the Ihas research group and V.F. Mitin at the Institute of Semiconductor Physics in Kiev, Ukraine, was opened. The goal of this collaboration was to produce miniature Ge film thermometers [62].

The characterization of the thermometers was conducted *in situ* with our calorimetry experiments. Because of the requirements of low temperature calorimetry, the thermistors were designed to have a very weak heat link to everything except the experimental helium. Specifically, the sensors were immersed in superfluid helium 4 and electrically wired with 50 μm gold wire to an electrical connector, which was heat sunk to the mixing chamber of the dilution fridge. The wire was thin to ensure the sensors primary heat link was the helium. During the calibration on these sensors, no sinter was used to heat sink the cell to the mixing chamber, so the minimum operating temperature was about 65 mK. The experimental cell was heat sunk to the mixing chamber by 4 $\times 1/4"$ copper rods mounted on a gold plated mount. The full experimental set up is described in Chapter 4.

The thermistors are based on a 2 μm thick thermosensitive film of Ge, deposited on 150 μm thick substrate made from semi-insulating GaAs. Layering of the materials by this technique produces a diffusive doping, which moves charge carriers from the Ge layer into the bulk GaAs film. Electric contacts to Ge are produced by a sequential deposition of Mo and Au on the film [63]. The sensor is shown in Figure 2-7 with all of the individual layers.

The sensor area and mass are defined by the GaAs substrate rather than the layers of the Ge and other metals, as this is the material that is heat sunk to the helium.

The Ge/GaAs thermistors are typically 0.3 mm square by 0.15 mm thick, yielding an estimated mass of the thermosensitive portion of the thermistor of $10^{-5}g$. For the naïve calculations to follow, the properties of the GaAs layer alone will be investigated and the other metallic films will be ignored. The result will be a limit on the the real response.

There are two main reasons why thermometry requires many seconds for a precise reading. The first is that the power used to run a resistive measurement has to be kept extremely low to avoid joule heating in the sensor. This power is of order picowatts for measurements below 100 mK. At such a low excitation current and detection voltage, electrical white noise is a concern and needs to be minimized. This is typically done by exciting and detecting the thermometer along a very small bandwidth. This technique is common to low temperature application and requires a lock-in amplifier. The other mitigating factor for determining the temperature of a helium sample is the Kapitza boundary resistance between the thermometer and the liquid helium. In the event that the resistance of the thermometer can be read quickly, this fundamental material property characterizes a barrier to heat transfer, both into and out of the thermometer.

If the Kapitza resistance is large, the thermometer, takes a long time to reach an equilibrium temperature with the liquid and does not readily radiate heat into the liquid which lowers the allowed excitation current. Evidence for the effects of internal heating in the thermistors is shown in Figure 2-8. As the temperature of the apparatus is lowered from 4 K to 50 mK the resistance of the thermistor increases in a predictable manner. However as the temperature is lowered past 100 mK, a clear indication of self heating is observed by some of the calibration curves ceasing to change. This is avoided by using lower excitation powers and longer averaging time in the measurement.

This effect can be lessened by using a larger sensor which increases the surface area of the sensor and the heat exchange between the helium and the thermometer or using longer integration times on the lock-in. In this example the second method was used. For steady state quantum turbulence experiments longer integration time and a

larger measurement area have the same effect of enlarging the volume of turbulence that is measured and delocalizing the probe. This equivalence is due to the Taylor frozen turbulence law [64]. The Kapitza bound resistance is present in all resistive low temperature thermometers, but its effect can be estimated by examining the sensors used.

Kapitza boundary resistance sets a limit to the transfer of energy from one material to another. For thermometry, the Kapitza resistance is due to a mismatch of phonon modes between the helium liquid and the sensor body. The different material spectrums do not align, and many of the energy carrying phonons are reflected by the sensor interface and their energy is not transmitted. This fundamental material property is summed up in the material specific Kapitza boundary resistance, R_k. It can be calculated with detailed models of the phonon spectrum of the two interacting materials as due to Khalatnikov [65, 66],

$$R_K = \frac{15 h^3 \rho_s c_t^3}{16\pi^5 k^4 \rho c_1 F(c_\ell/c_t) T^3}, \tag{2–1}$$

where ρ_s and ρ are the solid and liquid densities, k is the Boltzmann constant, c_ℓ and c_t are the longitudinal and transverse sound wave speeds in the solid, F is a function of c_ℓ/c_t which is usually around 1.5-2, and c_1 is the speed of first sound in the liquid. The Kapitza boundary resistance is also heavily dependent on surface finish and roughness, so the values for R_k are typically taken from measurements.

The boundary resistance is measured in a similar way to thermal conductivities, where

$$R_K = \frac{A\Delta T}{\dot{Q}}. \tag{2–2}$$

In this equation $\dot{Q}$ is the heat flow, A is the cross sectional area, and ∇T is the temperature gradient. From this equation, it becomes clear that the small sensors have very poor absolute thermal contact with the helium bath. This is perhaps the reason why the thermistors did not have good heat dissipation below 100 mK. The small

Table 2-2. Quantities used to calculate the Kapitza Resistance

Parameter	Value	
Mass (m)	$7.2 * 10^{-8}$	Kg
Area (A)	$9 * 10^{-8}$	m^2
Kapitza Resistance, (R_k) at 1 K [66]	8.122	m^2K/W
Specific Heat when doped with As, (c) [67]	$1.4799 * 10^{-4}$	J/KgK
Specific Heat when doped with Ga, (c) [67]	$1.8723 * 10^{-4}$	J/KgK

size of our thermistors gives them the advantage of a comparably lower heat capacity to other thermometers but the disadvantage of not being able to dissipate the ohmic heating from measurement. The reaction time to temperature variations in the liquid can be estimated by comparing the heat capacity of our sensors to their maximum thermal conductivity, determined by the Kapitza boundary resistance.

We can estimate the amount of energy it would take to change the temperature of the thermometers with the information in Table 2-2. The specific heat for the material in our thermistors is not explicitly stated so estimates for their values were taken from P. H. Keesom and G. Seidel [67]. The estimates are for As and Ga doped Ge at 500 mK rather than the exact doping of material in the sensors. In addition, the Kapitza resistance for doped germanium was not known, so values of elements with similar structure and periodic table location (Si, Sn, and Pb) were averaged together and the $R_k \propto T^{-3}$ scaling was used. Integrating the linearized specific heat from Table 2-2 and applying the Kapitza resistance the maximum excitation current as a function of temperature can be calculated. These results are plotted in Figure 2-9 where the x-axis is the thermometer temperature and the y-axis is the required temperature gradient for a sensor with the specifications in Table 2-2 to dissipate the $2.5 * 10^{-12}$ W at which the thermometer is driven. These thermistors were used to collect the data presented in Chapter 4.

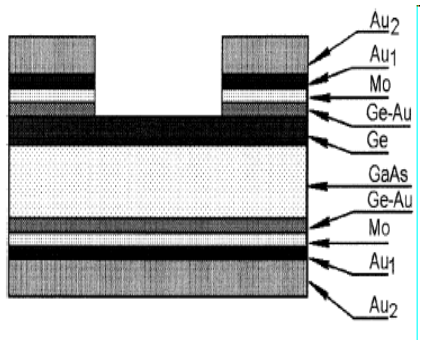

Figure 2-7. This schematic of a thermistor shows the layers of deposited metal present in each thermistor and their relative sizes.

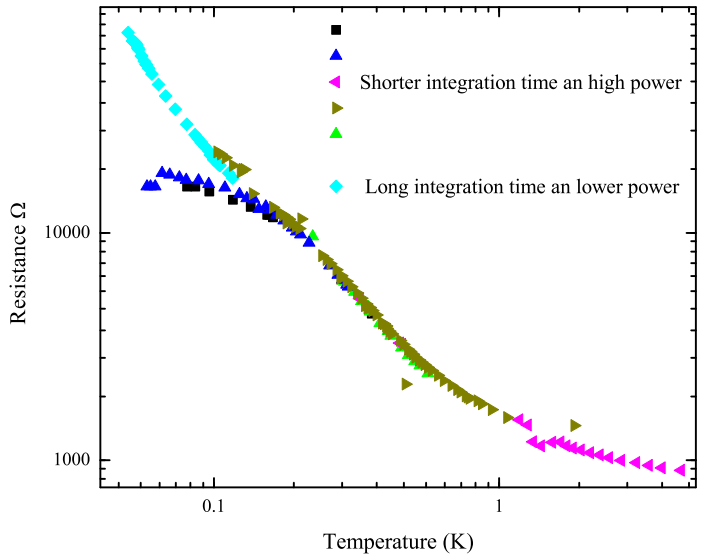

Figure 2-8. This shows a resistance vs. temperature calibration for a thermistor produced by the Mitin group [63]. The division between the curves at low temperatures is due to a self heating effect in the thermistor. The flattened data is for the excitation needed to measure the thermistors on time scales less than one second (30 ms) and the long integration time (3 s) data is for a lower excitation current and longer measurement times.

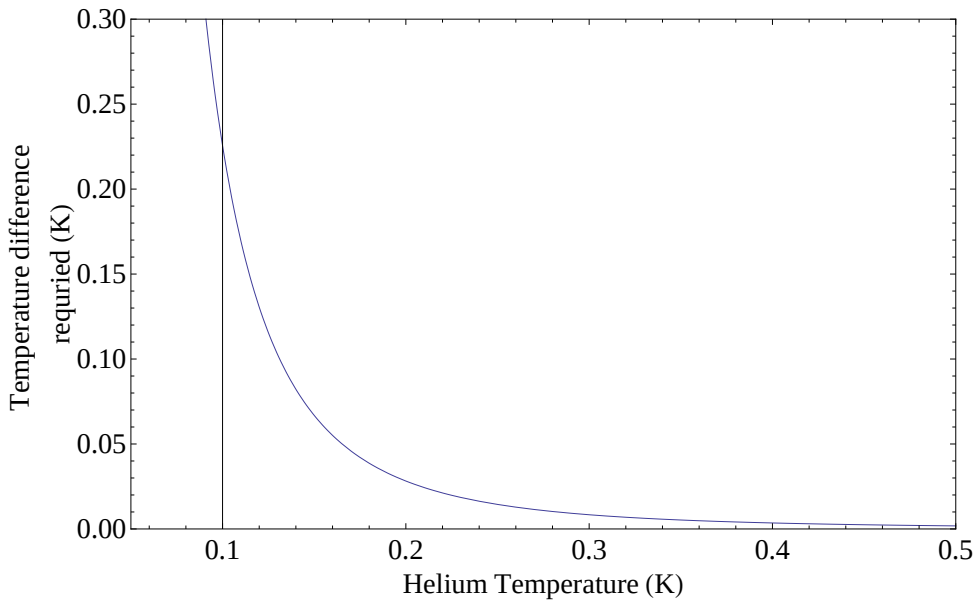

Figure 2-9. This plot shows the temperature gradient between the thermistor and helium bath required to avoid self heating as a function of temperature. The power used to measure the thermistor in this plot is 1.5 pW.

CHAPTER 3
MOTOR DESIGN

After designing new sensors necessary to measure the properties of quantum turbulence, what type of turbulence should be created and how is it made? This question arises naturally because of the plethora of different fluid systems described in the literature. Turbulent systems are ubiquitous in natural processes, and superfluids are no different. In fact, superfluids support a type of turbulence that is not seen in classical fluids, thermal counterflow turbulence. With all of the options available the simplest was chosen for this research, homogenous and isotropic. Previously in this thesis, it was mentioned that there are two typical methods to create this kind flow. First is flow through a channel into a stationary mesh grid and the other is a grid pulled through a stationary fluid. In superfluid helium, due to the low kinematic viscosity, it is incredibly difficult to produce a non-turbulent pipe flow with a flow of any significant velocity. Therefore, pulling a grid through a stationary fluid is more appealing. Helium flowing through a grid is the Galilean transform of pulling a grid through a stationary fluid and therefore these two are equivalent. In the scenario investigated, the fluid is stationary so it will not be turbulent when it comes in contact with the grid.

Several motor systems were conceived, designed, and built to pull the grid through the helium operating at a range of velocities. The final motor design is capable of moving the grid across a large dynamic range in velocities, from 0.01 - 100 mm/s. This motor is designed to produce a relatively large pull range, since a finite distance is required to establish homogenous isotropic turbulence. The motor has a stable operation range of more than 1.5", much longer than the 10 mesh spacings required for the flow behind a grid to be homogenous and isotropic [68]. The speed at which the grid is pulled is large enough to create turbulence but slow enough, relative to the speed of sound ($200\ m/s$), so that we can treat the flow as incompressible. This is a project which received contributions from many research groups, in particular Lancaster and

Florida. All of the motors from our group have all worked on the principle of magnetic levitation due to field expulsion from a superconducting cylinder. The procedure is used to create motion with minimal heat input to the system and no physical connections to the outside. The operating procedures and experimental designs have matured over the years, becoming more sophisticated and producing more consistent motions over increasingly large pull distances. All of these and their results are discussed in Chapter 3.

The development of this apparatus posed a serious experimental challenge because of the severe physical environment of ultra low temperatures and stringent requirements of the motion. For experiments to be of scientific use, the dimensional scales need to be well defined. This means that among other things, the grid must be pulled at a constant velocity, V. Producing large scale motion, on the order of inches, at millikelvin temperatures, without also producing copious heating requires electro-magnetic levitation (for linearly moving grids) or gas/liquid bellows (for flowing liquid). This is because at millikelvin temperatures it is difficult to transfer motion from a room temperature apparatus to the bottom of a cryostat. This type of system can be created for high temperature experiments above 1 K [30]. Standard machinery is difficult to operate at low temperatures; the gears create frictional heating and all resistive electronic components are sources of heat. In the past, resistive motors have been used at millikelvin temperatures, but the internal wiring of the motor was removed and replaced with superconducting wire [61]. Even in this situation, long wait times are required after their use for the heat to dissipate. In addition, most motors will freeze at these temperatures unless modified for low temperature operation, i.e. removing the lubricants. To create turbulence for calorimetric measurements, very large motions are required, so oscillating structures are not ideal. Although there are interesting questions for oscillating flow types, there is little reason to believe they produce homogenous

isotropic turbulence. For all of these reasons, we chose to initiate our turbulence with an electro-magnetic levitation device, henceforth referred to as a motor.

In addition to the inaccessibility of the experimental fluid volume, the important helium parameters relevant for this work are strongly temperature dependent. Therefore, any spurious heat generated from non-fluid motion can severely change the experiment parameters. For our experiments above 1 K, one such property is the fractional superfluid density, and for the millikelvin work, the heat capacity of helium is proportional to T^3. For comparison, metallic heat capacities typically diminish linearly with temperature. Once the electron modes in metals have frozen out ($T \ll T_{Debye}$), the ratio of heat capacities $C_{He}/C_{Metal} \propto T^2$. This not only makes the use of metal in the construction of our apparatus unfavorable, it also means that our experiment is sensitive to very small thermal energy sources which are unrelated to the turbulent decay, including ohmic, eddy current and frictional.

Over the past 20 years there has been a flurry of work on turbulence in superfluid helium. However, other than the motor designs discussed here, no apparatus has attempted to create isotropic and homogenous turbulence at millikelvin temperatures by this mechanism. All turbulence *generation* apparatus can be categorized as highly polarized (rotating) [7], counterflow [69], pipe flow [53], or oscillating objects [55, 70]. The generation of flow in these systems is not homogenous and isotropic, but for such experiments, there is evidence that the late time behavior is. To be sure, grid turbulence is not generated as homogenous and isotropic, but there is substantial evidence that it becomes so a few mesh spacings rom the grid. The nearest experiments to linear grid turbulence at millikelvin temperatures are the recent work on oscillating structures at low and nearly zero frequencies, where a close approximation to linear motion is present [71]. This work has other problems as well, such as flow around the oscillating grid in addition to the flow through it. For the work on oscillating structures, it is not clear if the quasi-linear motion is of high enough quality to reproduce linear grid flow, nor is it

clear that the most important flow length scales are due to the flow through the grid or around the outer region of the grid. Work on quantum homogenous isotropic turbulence above 1 K for both a pulled grid [72] and for a stationary grid with a traveling fluid [53] has been reported. Both of these works show nearly classical behavior, since at 1 K the normal and super components are rigidly locked by mutual friction. For the high temperature fluid flow, a strong classical influence is present due to mutual friction, and this differentiates the flow that we strive to create from the previous work done in this area. We would like to use one system, to explore grid turbulence across the wide range of temperatures in superfluid with several measurement techniques. Over the past 10 years we have developed a progression of different motor designs, beginning with the 'passing design' and ending with the 'control motor'. Each design will be reviewed in Chapter 3 with varying degrees of emphasis.

3.1 Passing Motor

The first linear motor, based on an operating principle similar to that of a particle accelerator concept was produced out of a collaboration by the University of Florida and the University of Lancaster. In a particle accelerator, many different magnetic drive coils work with one another to move a charged particle along a ring or line, each of them producing a well timed impulse to push the ion. In the case of a levitating motor, the particle is a superconducting Nb cylinder (part of a rod shaped armature) and the accelerator is submerged in liquid helium. Each coil in the array is responsible for producing a small localized magnetic field to push the armature a short distance into its neighboring coil. With programmed input currents, this apparatus "passes" the superconducting armature from point to point and may produce nearly any motion profile. A turbulence creating grid can be attached to the superconductor for the creation of turbulence. This motor is described in the literature [73].

The passing motor was designed to be dynamic in the motion patterns it produces, as well as scalable in size. For longer travel distance, more coils are added to the series

to increase the length of the track. The design has a disadvantage of being awkward and difficult to control as many individual actuating coils require individual circuitry and timing. For consistent operation all the coils should be nearly identical. With many coils, and perhaps slightly different coils, a precise control can be exerted (with difficulty) over short distances of roughly the length of the individual solenoids. The control of such a system requires an understanding of how all of the individual fields and superconductor interact. In particular, attention needs to be given during the period of time when the superconducting cylinder is moving through the gaps separating the coils.

As the superconductor travels across the gaps in the coils, the magnetic field gradient along the z-axis will switch from negative to positive. The Meissner force, which will be expanded on in Sec. 3.3, is proportional to $-B\frac{dB}{dz}$ so there is an inherent difference between positive and negative field gradients. Negative gradients are dynamically stable, where as positive gradients are unstable equilibriums. This is clearly visualized by looking at the integral of force or the potential energy. For $\frac{dF}{dz} < 0$, the potential energy at that point can be approximated as a positive parabola, where the stable location is the minimum of the potential. On the other hand if $\frac{dF}{dz} > 0$, the potential is approximated as a negative parabola where the equilibrium point is the maximum. This point is unstable due to the neighboring lower energy states.

This situation is illustrated in Figure 3-1. Here the superconducting actuator is shown as a yellow bordered blue box, and the individual solenoid fields are shown as black curves above the solenoids which are the grey boxes. This figure shows a time lapse with three different motor positions: in the first and top figure the actuator is pushed to the right by the magnetic field, however in the second image it is unclear which direction the force on the actuator is pointing, and it is not until the superconducting cylinder travels all the way to its location in the third image that the field gradient once again pushes the actuator in the proper direction. This figure demonstrates the difficulty

with creating a drive program for this design and exemplifies that precise timing in the circuit is required.

Stacking several identical solenoids on top of one another almost guaranties that at some point the levitated cylinder will pass through one of these transitions. For this motor design to work, the momentum of the actuator needs to be relied on to carry the motion along through these unstable areas. This is not impossible, but it adds a layer of difficulty to the design and makes the electronic timing of critical importance. To date, no working version of this design is in operation for quantum turbulence due to these complications.

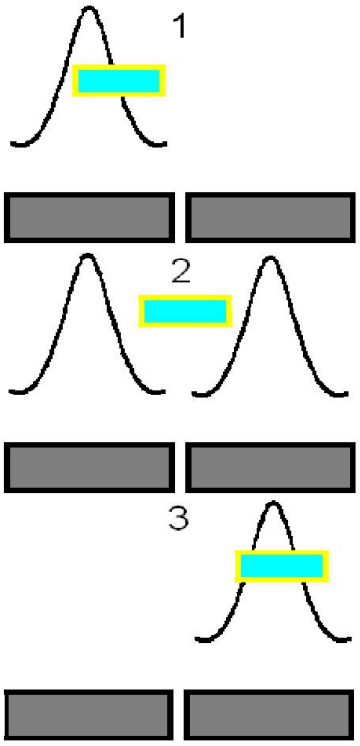

Figure 3-1. This plot shows the motion of the niobium in a cartoon passing motor. The grey bars at the bottom of the plot represent two of the drive solenoids used in this design. The black curves above the magnets display the magnetic fields of the solenoids and the blue bar is the niobium moving through the fields. This motor operates by precisely timing the currents in the drive solenoids.

3.2 Impulse Motor

The design for the impulse motor is similar to the passing motor but multiple coils are replaced with multiple superconducting cylinders [74]. The motor operates by controlling the current in a single solenoid as multiple Nb cylinders are passed through its center. This is in opposition to the previous design where a single Nb cylinder is passed through multiple solenoids. The impulse motor that was constructed uses 2 Nb cylinders. The small number of cylinders limits the range, but lessens the precise timing requirements. Additionally, by switching to one coil and multiple superconductors the differences between separate coils is no longer a factor. This new design is in a sense the Lorentz transform of the previous method. This design is also extensively explained in the literature [75].

The operating procedure for this motor is as follows: a current is applied to the drive solenoid while the first of two Nb cylinders is inside the solenoid. This produces an impulse in opposition to gravity and carries the Nb cylinder out of the solenoid. The second Nb cylinder is attached to the same actuating rod as the first and is initially located below the drive solenoid and well outside of its fringe field. The armature travels upwards until the second attached Nb cylinder is carried into the solenoid field. Because of the initial position of the second Nb cylinder below the coil, the force it experiences opposes the motion and acts as a brake which stops the armature. The momentum of the armature is set by the initial current pulse so the second, or breaking, cylinder will slow the armature and the attached grid at a specified location where the system can be held. This distance is set by the separation of the two cans, 2.1 cm.

This motor system was designed to produce very fast grid motions over a very short time scale. The original motor was designed to produce 1 m/s grid speeds over a motor pull length of 22 of mm. To produce this acceleration, the system is designed with short solenoids and steep field gradients the acceleration. The theory, motion calculations,

designs, and early results for this motor are reported in the dissertation by Shu-Chen Liu [75]. There also results produced from this system are presented in Chapter 4.

For these early motor experiments, the position of the armature was measured by a capacitive position sensor. Later this will change as the geometry of the motor and experimental cell dictate. This position sensor is designed so that the armature travels axially between two semicircular conductors. As the superconductor moves between the plates the dielectric properties of the space change. When the superconducting tube fully fills the space between the plates, the capacitance is at a maximum. When the space between the plates is empty, the capacitance is at a minimum. The capacitive measurements are calibrated at 1 K and assumed to be independent of temperature below this point. The position is a lock-in amplifier detector and compared to the calibration after the motor motion has ceased. Figure 3-2 shows the manner in which this sensor is run and Figure 3-3 shows the calibration data for the sensor. In the figure, the red colored material is the capacitive sensor and the blue colored material is the Nb armature inside the sensitive region.

The armature is guided by phenolic knife edge bearings. The results of using these ring bearings, and the heating they may have produced, were never made clear due to uncontrolled heating from other sources in the experimental cell. In the future motor designs it was omitted in favor of magnetic bearings.

The large current change over short times for the acceleration induces a strong back EMF voltage. An understanding of the EMF produced by the drive coil, as well as its interaction with the current amplification hardware, are required for a quantitative understanding of the entire motor motion. This effect was not accounted for in the original analysis.

In addition, the acceleration produced with this motor required high magnetic fields relative to the critical field, H_c, for Nb. And the sharp corners of the Nb cylinder can

experience penetration of the magnetic field. There is some evidence for this, which is presented in Chapter 4.

Partial penetration can occur because niobium is a type II superconductor. This means that some magnetic flux penetrates the superconductor, but the superconductor remains in the superconducting state. Partial penetration occurs at the lower critical field of a superconductor and the superconductor goes normal at the upper critical field. The lower critical magnetic field of Nb is exceptionally high relative to other elemental type II superconductors. This means that up to high magnetic field values of $\sim 0.2\ T$) Nb will behave as though it were a type I superconductor [76]. Low temperature type I and II superconductors are identical, in the physical sense that electrons in both form cooper pairs and follow BCS theory. The difference between the two types is the ratio of penetration depth, λ, and coherence length ,ξ. For a type I, $\frac{\lambda}{\xi} > 1$, while for type II, $\frac{\lambda}{\xi} < 1$. The differing ratios lead to a change in behavior at the normal to superconducting transition. The critical magnetic field for a superconductor is a function of temperature. The critical field for superconductors can be estimated by the following relations [76],

$$H_{c1} \simeq \frac{\Phi_0}{\pi\lambda^2} \tag{3–1}$$

$$H_{c2} \simeq \frac{\Phi_0}{\pi\xi^2}. \tag{3–2}$$

H_{c1} is the lower critical magnetic field where the nucleation of a single fluxoid is allowed, and H_{c2} is the upper critical field where the superconducting state can no longer be maintained and the material reverts back into its typical normal state. Φ_0 is a fluxoid or a single quanta of flux. For type I, $H_{c1} < H_{c2}$ and for type II the converse is true and therefore only one critical field H_c is measured. The magnetic flux penetrating a material is defined by,

$$\oint_C \vec{A} \cdot d\ell = \int_C \vec{B} \cdot d\sigma = \Phi. \tag{3–3}$$

$\vec{A}$ is the magnetic vector potential, $\vec{B}$ is the magnetic field and Φ is the magnetic flux in the material. Following from Ashcroft and Mermin [77], for a superconductor this turns out to be an integer multiple of $2\pi\hbar/q$ in a superconductor, or more precisely

$$\Phi_o = 2\pi\hbar/2e \simeq 2.0678 \times 10^{-7} gauss - cm^2. \tag{3–4}$$

The fluxoid is analogous to a quanta of circulation in superfluid He^4 as discussed in Chapter 1.

Measurements on Nb at zero temperature place the penetration depth at $\lambda(0) = 47 \pm 5\ nm$ [78] and the superconducting coherence length $\xi \simeq 13\ nm$ [79]. Inserting these values into Equations 3–1 and 3–2, we can expect values of $H_{C1} = 2,979.8\ gauss$ and $H_{C2} = 38,949\ gauss$. The experimental values for H_{C1} and H_{C2} are heavily dependent of the orientation and geometry on the superconductor relative to the magnetic field but the values above are calculated for an ideal geometry. The geometry used to achieve the maximum critical field is a long thin wire superconductor in axial symmetry with an applied magnetic field. This is not the geometry used in the motor design, so diminished values of critical field are expected. A more reasonable estimate for H_{C1} is the number commonly quoted in text books [76, 77] of $1,980\ gauss$ at $T = 0$. This field is calculated for a wide flat geometry.

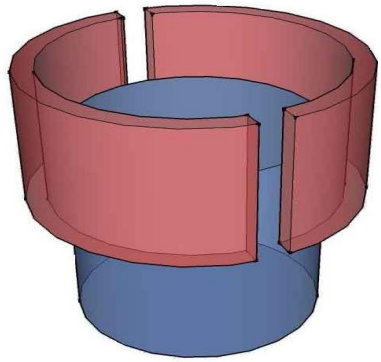

Figure 3-2. This figure shows a cartoon of the capacitive position sensor. In this figure, the blue is the niobium traveling through two copper (red) plates changing the capacitance across the circuit as a function of the niobium position.

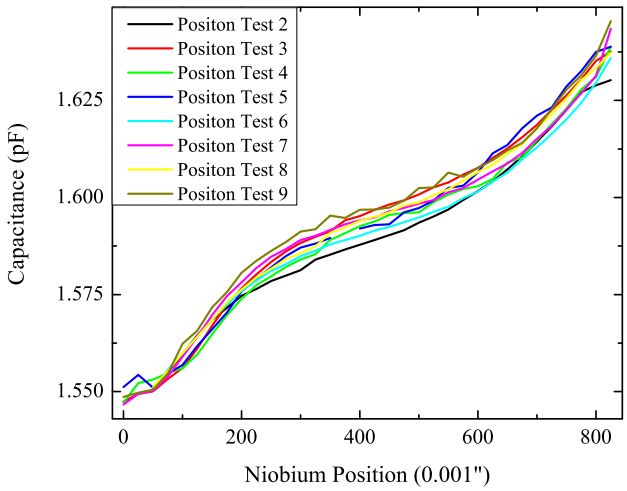

Figure 3-3. This plot shows the calibration of the capacitive position sensor as a function of niobium position. The many traces are different experimental runs.

3.3 Inertial Motor

The inertial motor is a shift in philosophy from previous designs. Rather than using a short solenoid to maximize field gradients, this design has one long solenoid. The short coil design essentially produces an impulse to “throw”the armature and a secondary pulse to “catch” it, while the long coil uses a more sustained force in time. This new technique maintains magnetic contact with the Nb cylinder for its entire motion, so the armature does not need to be passed from coil to coil as it moves. The Faraday voltage, or back EMF, which complicated the motion calculations in the previous work, is integrated into the drive mechanism of this new motor. In fact, the back EMF which previously was a hinderance, is instrumental in the operation of this new design.

The ideal magnetic field profile for this actuation design is one in which the magnetic field profile within the drive solenoid is entirely constant and directly outside is zero. For a magnetic profile such as this and a superconductor as an actuator the only dissipative force in the system is a non-linear drag force. This drag force depends on the velocity and is difficult to model throughout the motion. However, if a larger dissipative force is introduced to the system, which is directly proportional to the velocity of the Nb tube, the dissipation is better defined and controlled motor motion is possible. A convenient method to introduce this frictional force is through the Faraday’s law. This law can be summed up as, “A changing magnetic field induces an electric field" [80], and is defined by the integral and differential equations.

$$\oint \vec{E} \cdot d\vec{\ell} = -\int \frac{d\vec{B}}{dt} \cdot d\vec{a} \tag{3–5}$$

$$\nabla \times \vec{E} = -\frac{\partial \vec{B}}{\partial t} \tag{3–6}$$

Together these relations lead to the well known generation of electromotive force (EMF)

$$\varepsilon = -\frac{d\Phi}{dt} = \frac{d(IL)}{dt} \tag{3–7}$$

where Φ is the flux, L is the inductance, and I is the current in the circuit.

For the motor proposed in this section a resistor is introduced into the drive circuit parallel to the drive solenoid, creating dissipation. Specifically, as the EMF is generated by the changing of IL as a function of time, a dissipative current will flow through the shunt resistor. A back EMF is generated from two distinct sources; changing I in time and a changing L. The $\frac{dL}{dt}$ term determined by analyzing the motion of the motor, while $\frac{dI}{dt}$ will need to be explicitly obtained by analyzing the current flow in the drive circuit. This type of electrical design is common to demagnetization stages for ultra cold cryostats where the current needs to be slowly bled out of the magnet. It is well known that when a superconductor is in the presence of a magnetic field, its magnetization increases linearly with magnetic field (until H_{C1}). Here this implies that the Nb acts as a perfect diamagnet with a magnetization $\propto B$. As a result, as the armature moves it will create a Faraday voltage across the drive coil and parallel resistor. This process is identical to the effect a permanent magnet experiences as it is dropped down a solenoid. The Nb will experience the same type of retarding force as it travels through the drive solenoid. The EMF is directly related to the motion of the armature, so the voltage created by the motion of the Nb cylinder produces a dissipative current in the shunt. This damping force (Faraday drag) is calculated and optimized in the following pages.

The apparatus for this experiment is shown in Figure 3-4. The Nb cylinders are burgundy, the insulating G-10 spacer is purple, the drive solenoid and the position sensor are green. The position sensor is located below the bottom bearing magnet (colored grey) and the drive solenoid is in the center of the image. Also shown in the figure is a sketch of the electronic drive circuitry. The bottom Nb is used as both a bearing and a position sensor while the top Nb cylinder is used to actuate the motor and as a bearing.

In this actuation method, the drive coil ideally creates a magnetic field in its interior which quickly decays outside the solenoid. With this system, if the superconductor is

inside the solenoid as it is in Figure 3-4 an upwards force is established. At the start of the motor motion the current in the drive is set so the armature is on the brink of motion. At this current the Meissner force exactly cancels out gravity (see Equation 3–13) but provides no more force. After this is established the current in the solenoid is raised, producing a lifting force for the armature. By virtue of the magnet design the armature will accelerate until the Faraday drag exactly cancels out the applied force.

Fig 3-5 shows a cartoon of the current profile inside the drive coil as a function of time, with the motor operation over the entire course of motion described here. Initially, the current in the drive solenoid is set to the maximum value that does not produce motion. Therefore, any additional current will produce a force in the z direction. The exact value of the current in the motor at this time is either calculated or calibrated by monitoring the position sensor as the current in the drive is slowly increased. When an additional current step is added, all of it flows through the shunt resistor, because for this stepwise current increase the reactance of the drive is ∞. After a short time, τ, current will begin to flow through the drive coil as well. This increase in drive current produces an acceleration of the armature. The armature will accelerate until it approaches a terminal velocity that is defined by a matching of the induced EMF from the coil and the voltage across the shunt resistor. The current in the drive coil at this point exactly matchs the initial condition where the motor was held on the brink of motion and therefore the armature and grid are traveling in a nearly constant speed. At this point of the motion, all of the additional current added to the circuit bypasses the coil and flows through the shunt resistor. During this constant velocity motions a constant EMF is generated by the “Faraday drag” of the armature. The braking procedure at the end of the motion proceeds similarly, but with the applied current being lowered rather than raised. With this method, linear motions at various speeds are obtainable, and controlled by the size of the instantaneous current step at time $t = 0$.

With a naïve kinetic dissipation model in hand we can develop quantitative equations to match the qualitative description of our motion. This model contains the following assumptions: the magnetic field inside a “long” solenoid is flat; immediately outside the solenoid the same field falls to zero (described by Equation 3–8); the drive coil is a perfect superconductor with zero resistance, and lead resistance of the circuit is negligible. The first two requirements stipulate that the solenoid magnetic field is perfectly “box” shaped, and a perfect superconductor implies that the coil will act as a pure inductor with no real resistive component. Figure 3-6 shows the ideal magnetic field in this design as a function of axial location, z. Physically speaking, this means the current will never “hop" out of the Nb wire and into its copper clad construction causing ohmic dissipation.

Expanding on the idea that a superconductor acts as a perfect diamagnet, we can calculate the exact voltage produced by the Nb cylinder traveling through our coil. It is well known (for example in Tilley and Tilley [81]) that the magnetization, M, of a superconductor is proportional to its surrounding magnetic field, such that $M = -\mu_o H$. In effect, the Nb inside of the drive field acts like a perfect bar magnet of magnetization $M = -B$, where B_o is the solenoid field. It is easy to see that as the Nb cylinder moves out of the solenoid, the end of the cylinder still inside the coil will pass through the many successive loops of the drive solenoid. As each loop is passed by the moving Nb cylinder an EMF will be generated in the superconducting solenoid equal to $d\Phi/dt$ in the opposite direction of the applied voltage. If a resistor is electrically in parallel with the drive, a current will be pushed through the (dissipative) resistor.

Let us specify that the magnetic drive coil has a length b and the field in the core of the coil is expressed by the infinite solenoid approximation,

$$B = \mu_o n I \qquad \textit{Inside solenoid} \tag{3–8a}$$

$$= 0. \qquad \textit{Outside solenoid} \tag{3–8b}$$

where B is the magnetic field, μ_o is the permittivity of free space, I is the current inside of the coil, and n is the turn density. The movement of the superconductor leads to a change in the flux inside individual wire loops of the solenoid. The change of flux, $d\Phi/dt$, inside the solenoid can be measured by a change in inductance or calculated as a function of time,

$$\frac{(Ndx/L)\ (A)\ (B)}{dt}.$$

I_L is the current in the solenoid, L is the solenoid inductance, N is the total number of turns, and A is the armature cross section. In this relation, Ndx/L is equal to the number of current loops in a given length dx. This equation can be rearranged to produce,

$$I_L \frac{dL}{dt} = nABU, \tag{3–9}$$

where U is the armature speed. The induced Faraday voltage of this system is

$$\varepsilon = RI_R = \frac{d(LI)}{dt}. \tag{3–10}$$

This includes both the geometric effect, dL/dt, and the reactance component, dI/dt. Here $\varepsilon = EMF$, R is the resistance of the shunt, and I_R is the current through the shunt. Combining equations 3–9 and 3–10 we arrive at,

$$\varepsilon = RI_R = nAB_oU + L\frac{dI}{dt} = nAB_oU. \tag{3–11}$$

These equations are written for arbitrary magnetic fields and motor speeds. Combining these three equations, 3–9, 3–10, and 3–11, and applying them to particular situations, we can solve for the kinematic response for specific current inputs. Figure 3-7 shows the electrical diagram and the labels for the currents in each part of the circuit.

The net force on the armature is the sum of the gravitational force, pointing in the $-\hat{z}$ direction, and the Meissner force, pointing in the $+\hat{z}$ direction. The Meissner force is defined as the force resulting from the bulk expulsion of magnetic flux from a superconductor. It can be calculated by noting that magnetic energy displaced by a

superconductor is equal to

$$\widetilde{U} = \frac{-\chi B^2 \forall}{2\mu_o} \tag{3–12}$$

where $\widetilde{U}$ is the energy, $\forall$ is the volume, χ is the magnetic susceptibility, B is the magnetic field, and μ_o is the permeability of space. Given force is the gradient of energy, $-\nabla U = \vec{F}$, a cylindrical symmetry, and $\chi = -1$, the Meissner force on the armature equals,

$$F_z = \frac{Adz}{2\mu_o}(2B\frac{dB}{dz}). \tag{3–13}$$

Integrating this equation along the length of the superconducting cylinder and combining with a local gravitational force we arrive at,

$$F = m\dot{U} = \frac{A}{2\mu_o}(B_B^2 - B_T^2) - mg \tag{3–14}$$

B_B is the field at the bottom of the superconducting cylinder, and B_T is the field at the top.

Now we assume the particular magnetic field profile of $B = \mu_o n I$ from Equation 3–8. This field produces a force on the Nb armature equal to $F = \frac{A}{2\mu_o}(\mu_o^2 n^2 I^2) - mg$. For now we ignore the possible effects from resistance in the coil and solve the simplified dynamics. This will be included in this derivation once some of the mathematical machinery has been developed. Are additional force present for motion through a real fluid is the fluid dynamic drag "$\frac{1}{2}A_{grid}\rho U^2$", which will also be ignored for the time being as well. In the end, this term is small compared to the energy dissipation in the shunt resistor and can be ignored in the final result, but here it is an assumption. Adding Equation 3–14 to the list of relations, established in Equations 3–5- 3–7, allows simulation of the real applied magnetic field required for the desired motion.

The maximum current applied to the coil the superconductor is $I = I_o$. The current step delivered to the motor is I_s, therefore the total applied current to the motor circuit is $I_a = I_o + I_s$. The shunt resistor (R) has a current I_r. Arranging the various currents I_L, I_r,

I_a, I_s, and I_o represent the current passing through the drive solenoid, shunt resistor, the combined circuit, current step increase and the current required to exactly cancel gravity respectively. The diagram showing the circuit components and their corresponding labels is shown in Figure 3-7. In this figure, A is the current source, a Kepco bipolar operational amplifier driven by a data acquisition card (DAQ) and labview software. The resistor labeled R is the shunt and the inductor L is the drive coil. The resistance of the lines is assumed to be zero and the impedance of the amplifier is infinite.

The current through the solenoid and shunt for all times after the step current has been applied, $t > 0$, is defined in equations 3–15 and 3–16.

$$I_L = I_o + \delta I(t) \tag{3–15}$$

is the drive coil current and the current in the shunt resistor is

$$I_R = I_s - \delta I(t). \tag{3–16}$$

$\delta I(t)$ is a functional current such that $\delta I(0) = I_s$ and $\delta I(\infty) = 0$, if the initial reactance of the circuit is ignored. $\delta I(t)$ is formally defined as $\delta I(t) = I_a - I_o - \varepsilon/R$. Substituting Equation 3–15 and 3–16 into Equation 3–14 and assuming the field profile from Equation 3–8, the equation of motion is written as

$$m\dot{U} = \frac{A\mu_o n^2 I_o^2}{2} + \mu_o A n^2 \delta I(t) I_o + \frac{\mu_o A n^2 (\delta I(t))^2}{2} - mg \tag{3–17}$$

and with Equation 3–11

$$\varepsilon = RI_R = \mu_o n^2 A(I_o + \delta I(t))U + L\frac{d(I_o + \delta I(t))}{dt}. \tag{3–18}$$

Equation 3–17 can be further simplified by noting that $\frac{A\mu_o n^2 I_o^2}{2} - mg = 0$ (Equation 3–13) and by assuming that second order terms are negligible, $\mu_o A n^2 (\delta I)^2 = 0$. Linearizing, the equation reduces to

$$m\dot{U} = \mu_o A n^2 \delta I(t) I_o. \tag{3–19}$$

Solving for $\delta I(t)$ gives

$$\delta I(t) = \frac{m\dot{U}}{\mu_o A n^2 I_o}. \tag{3–20}$$

Plugging this into Equation 3–18 we arrive at the complete kinematic equation

$$\varepsilon = R(I_a - \frac{m\dot{U}}{\mu_o A n^2 I_o}) = \mu_o n^2 A(\frac{m\dot{U}}{\mu_o A n^2 I_o} + I_o)U + L\frac{m\dot{U}/\mu_o A n^2 I_o + I_o}{dt}. \tag{3–21}$$

Rearranging the terms leads to

$$\frac{R I_o A n^2 \mu_o}{mL} I_a = \ddot{U} + \frac{\mu_o n^2 A}{L I_o} U\dot{U} + \frac{R}{L}\dot{U} + \frac{I_o^2 n^4 A^2 \mu_o^2}{mL} U. \tag{3–22}$$

It is known that if time is taken to $t \to \infty$, the Faraday drag will impose a critical velocity on the Nb and U will become a constant. The existence of a steady critical velocity at $t \to \infty$ implies that, $\delta U = U - U_{steady}$ with U_{steady} equaling the constant velocity at $t = \infty$. Solving Equation 3–22 for the constant velocity condition at $t = \infty$ and substituting $B_o = \mu_o I_o n$,

$$U_{steady} = \frac{R}{A B_o n} I_s. \tag{3–23}$$

This new definition can now be inserted into Equation 3–22 to calculate the velocity at any given time,

$$\frac{R I_o A n^2 \mu_o}{mL} I_s = (\delta\ddot{U}) + \frac{\mu_o n^2 A}{L I_o}(U_{steady}(\delta\dot{U}) + \frac{1}{2}(\delta\dot{U})^2) + \frac{R}{L}(\delta\dot{U}) + \frac{I_o^2 n^4 A^2 \mu_o^2}{mL}((\delta U) + U_{steady}). \tag{3–24}$$

Keeping only the linear terms of δ and rearranging the equation we are left with

$$\widetilde{A} = \delta\ddot{U} + \widetilde{B}\delta\dot{U} + \widetilde{C}\delta U. \tag{3–25}$$

Here $\widetilde{A} = \frac{R I_o A n^2 \mu_o}{mL}(I_a - I_o A n^2 \mu_o U_{steady}) = 0$, $\widetilde{B} = \frac{n^2 A \mu_o}{L I_o} U_{steady} + \frac{R}{L}$, and $\widetilde{C} = \frac{\mu_o^2 n^4 A I_o^2}{mL} = \frac{2gA}{bA_o}$. The constant $\widetilde{C}$ is simplified by incorporating Equation 3–8 and observing that $L = A_o \mu_o n^2 b$, where b is the length of the drive coil and A_o is its inner area. The solution for this simple differential equation is revealed by assuming a solution of the form,

Table 3-1. Inertial Motor Parameters

Parameter	Value	
Turn Density	5072	$Turns/m$
Area	1.52 E-3	m^2
Permeability	4π E-7	$\frac{N}{A^2}$
Current, I_o	1.5	A
Shunt Resistor	0.1	Ω
Inductance	0.383	H

$\delta U = \delta U_o e^{-\beta t}$, where β is the solution of the quadratic equation

$$\beta^2 - \widetilde{B}\beta + \widetilde{C} = 0. \tag{3–26}$$

Solving $\beta = -\widetilde{B}/2 \pm \sqrt{b^2 - 4\widetilde{C}}$, and inserting reasonable numbers for the parameters from Table 3-1

$$\beta = 0.25 \pm 7.6i. \tag{3–27}$$

This solution produces a damped oscillation taking the motor up to a constant speed of U_{steady} with a time constant of 0.25s or a velocity of

$$U \simeq U_{steady} + e^{-t/4} sin(7.6t). \tag{3–28}$$

With the equation of motion for this model system solved, the experimental data from this motor design are presented in Secs. 3.3.1 and 3.3.2. However, before this is done the validity of the assumption that the Faraday drag is a much larger force than the non-linear hydrodynamic drag is checked. To do this numbers are inserted into their equations,

$$F_{Faraday} = nAB_o I_s \tag{3–29}$$

and

$$F_{Hydro} = \frac{1}{2} A_G \rho U^2. \tag{3–30}$$

With the parameters of our system $\frac{F_{faraday}}{F_{Hydro}} = 212460$. The second order terms $\dot{\delta U}^2$ and $\dot{\delta I}^2$ were also ignored. To check this, the ratio of I_o/I_s is taken. This is equal to $\frac{\tau AU}{bA_o}$ or with reasonable numbers is 0.0, showing that the second order terms are indeed small compared to the leading order. The final assumption is that $B_T^2 << B_B^2$. This is checked by calculating the fields at both locations and taking the ratio of the two, $B_T/B_B = 0.006$. Therefore, the non-zero magnetic field at the top of the Nb can be ignored.

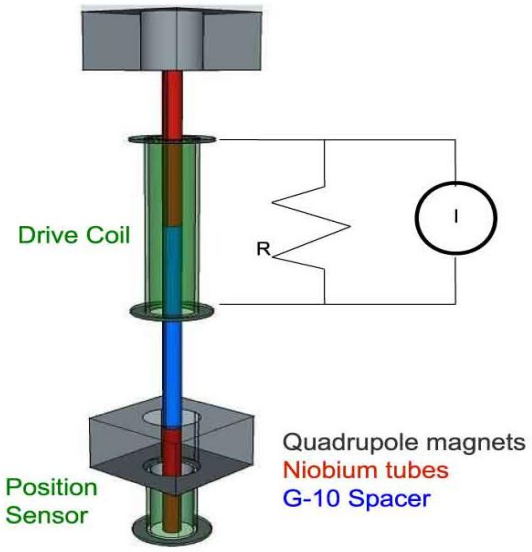

Figure 3-4. Schematic for motors containing quadruple magnets. For the inertial motor the drive solenoid is a single solenoid as is shown in this figure. For the control motor design, the drive coil is surrounded by an anti-Helmholtz set of three coils.

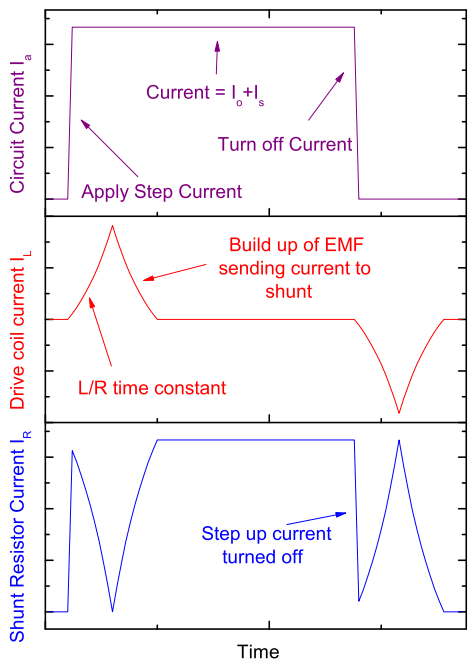

Figure 3-5. This diagram shows the values of current in each component of the inertial motor as a function of time. The applied current in the purple figure is the sum of the current traveling through the drive solenoid and shunt resistor branches.

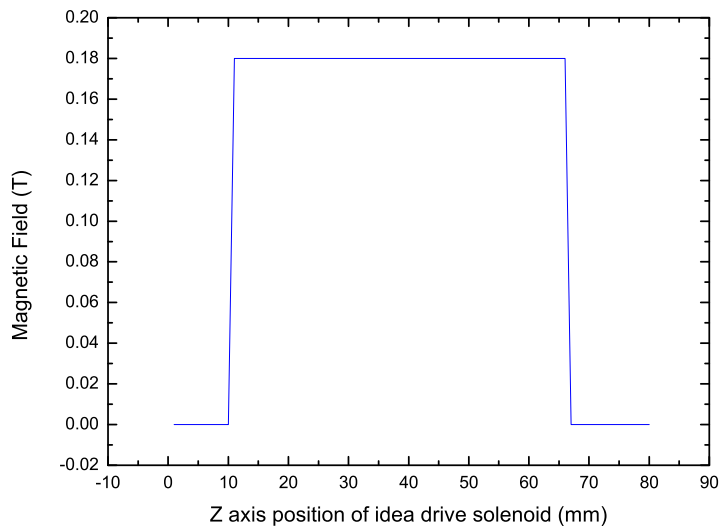

Figure 3-6. This is the magnetic field that was used to develop the theory for the inertial motor. With this assumption the current is finite and perfectly flat inside the drive solenoid and falls to zero directly outside of it.

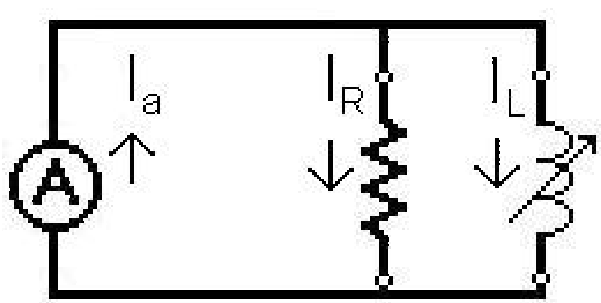

Figure 3-7. This diagram shows the names of the currents used for the motor motion theories.

3.3.1 Initial Results at 4 K

The theoretical framework discussed above was put to the test. A drive magnet, similar to the one in the theory, was wound on a mandrel. A $1/4$" diameter hollow Nb cylinder was epoxied to a G-10 tube and inserted into the center of the solenoid. A photo of this apparatus is shown in Figure 3-8. These first experiments were conducted in a 'suckstick' apparatus [82]. The suckstick is a double walled stainless steel cryostat, which can be easily inserted into a helium transport dewar. With an appropriate external pump, the cryostat is able to achieve a base temperature of just above 1.3 K. The drive coil for this apparatus was a 55 mm long solenoid wound with 4 layers of copper clad NB-Ti wire. This solenoid is shown attached to the optical dewar insert in Figure 3-9 and the calculated magnetic field for this coil is shown in Figure 3-10 as a function of position. The Nb used in these experiments is commercial annealed tubing Nb with a purity of 99.9 %.

For this initial experiment we constructed a position sensor similar to that used on the impulse motor discussed in Sec. 3.2. While the position sensing technique remained the same as in the previous work, the geometry was heavily altered to have a much larger gap between the moving Nb cylinder and the outer capacitive plates. This increased distance was required necessary to remove all non-superconducting electronic components from inside the helium cell.

The results with this experimental setup were inconclusive. The data suggested that the position detection of the Nb armature was not sufficiently sensitive and the motion profile as a function of input current was not determined. To produce a better position sensor, a considerable amount of effort was expended, while avoiding any metal or semiconducting components in the helium sample. This process led to the creation of several different position sensors, of different designs, and made from different materials. A small sampling of these can be seen in Figure 3-11. The best calibration from these tests is shown in Figure 3-3. Capacitive position sensors are not well suited

to this type of motor, because the capacitance of the sensor is inversely proportional to the gap distance between a given side of the capacitor and the Nb rod, while it is directly proportional to the distance the armature moves. This geometry dictates that the position sensor is sensitive to radial and axial changes in position. In addition, the increased gap necessary for the new cell make this an unsuitable design. But, to see if the theoretical motion calculations are accurate, the motor was mounted in a glass dewar where the motion could be directly observed.

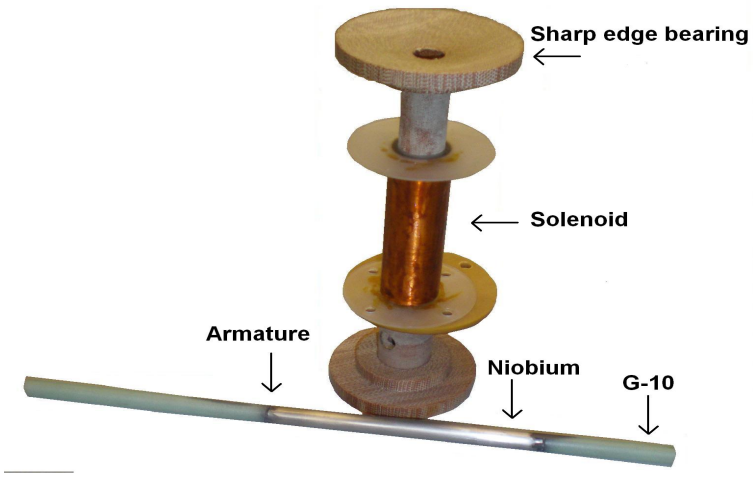

Figure 3-8. This figure shows the test cell used in many of the experiments in the suckstick. The drive solenoid is seen in the figure, as well as the sharp edge used to bear the armature during its motion. The armature used in this cell is shown lying in front of the apparatus.

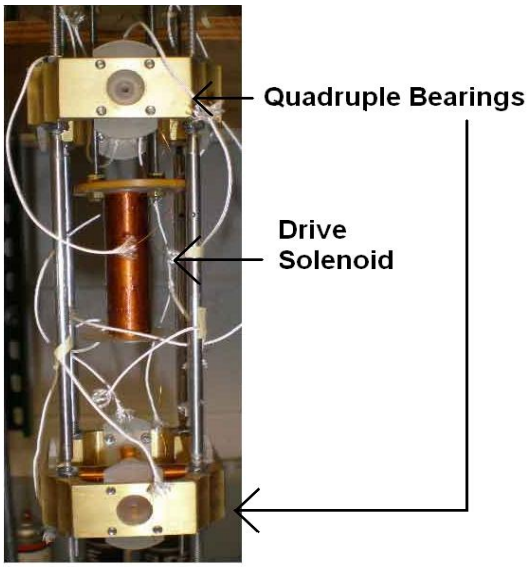

Figure 3-9. This is an image of the apparatus shown in Figure 3-4. Seen in this figure are the two quadruple bearing magnets and the $65\ mm$ drive solenoid.

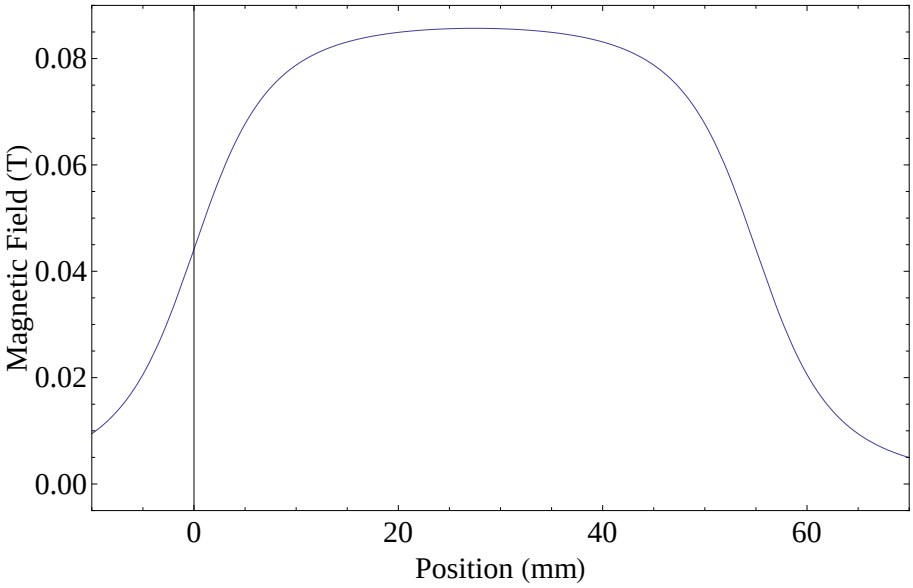

Figure 3-10. This figure shows the calculated magnetic field for the 55 mm drive coil used to test the inertial motor theory.

Figure 3-11. This is a photograph of the various position sensors constructed. The 1 inch inductive sensor is on the left next to 4 different capacitive sensors of slightly different design and sophistication.

3.3.1.1 Optical Cryostat Results

The motor was reassembled and attached to a new mount which is shown in Figure A-3. The motor assembly used for this work is shown in Figure 3-4, except here there was no position sensor mounted. The pertinent dimensions for this apparatus are given in Figure 3-9. The glass dewar apparatus insert is shown in Figure 3-9. Unfortunately, the first cool down of the dewar revealed a crack on the helium side of the glass dewar. Due to this, the liquid helium from the transfer seeped into the vacuum space and we were unable to proceed. However, a different dewar was available and the cryostat insert was changed to match the new design. This is mentioned because the replacement dewar used in place of the original was longer; this had the practical effect of raising our base experimental temperature to 4.2 K and eliminating our ability to submerge this motor in superfluid.

Therefore the first tests on the motor when the motion was verified were conducted in a optical glass cryostat at 4 K and the motion was observed visually and recorded on a standard digital camera. The purpose of this experiment was to verify that the motor behaved qualitatively as we expected since no accurate position sensor had been developed. Figure 3-12 shows a series of still frames of the motor moving and Figure 3-13 shows select motor motions taken from analyzing the videos of the digital camera. The position axis of the video is undetermined in the plots, but the total motion was $25\ mm$ and the scale measured in the videos is assumed to be linear.

Because of the exploratory nature of this experiment, the shunt resistor was situated outside of the cryostat insted of directly at the coil. Hence the lead wires to the drive coil have a total series resistance of about 1.5 Ω, rather than the insignificant resistance of a superconducting coil. This in turn required a larger power source than available to run the motor as designed. The minimum shunt resistance parallel to the motor coil was 3 Ω, or 30 times higher than the optimum calculated value.

The tests shown in Figure 3-13 show very slow changes in the motor position. The drive current was changed very slowly in time, rather than instantaneously as was proposed in the theory section. These tests served two purposes; they “mapped" out the magnetic field of the drive solenoid as a function of position, and showed the stability of the armature at each position along the traverse. The magnetic profile of the drive coil is observed in the shape of the motor traces in Figure 3-13, because the current was ramped linearly in time. Therefore, the equilibrium position of the motor for a given current can be calculated. For each run of the motor, at early times there is a quick rise to the top of the drive solenoid, followed by a slow controlled descent of the armature to the middle of the drive coil where the armature becomes unstable and falls out of levitation. This behavior is indicative of the changing magnetic field gradient. When it is in the bottom half of the drive coil the derivative of the magnetic field is positive, and when the Nb is situated above the center of the coil the bottom of the coil sits in stable equilibrium positions, exactly as expected. Because of this fact, only the solenoid magnetic field for for positions above the center of the coil can be mapped. One final curious feature from this data set is the violent oscillations on some of the motor runs. These were identified as physical oscillations initiated by nitrogen in the shield evaporating and are ignored as they are irrelevant to the operation of the motor in a dilution refrigerator.

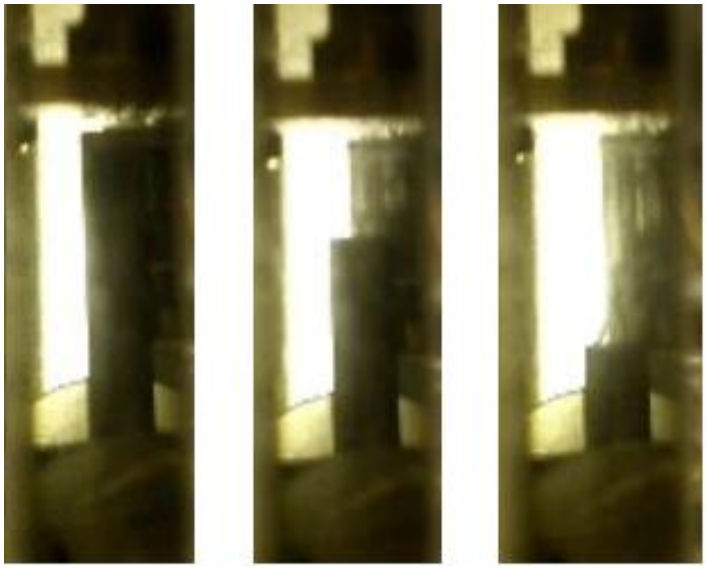

Figure 3-12. This figure shows still frames extracted from the videos of the motor motion. The dark cylinder moving downwards across the three figures is the top of the niobium being lowered by the magnetic field. These videos were analyzed to produce the first quantitative description of the motor motion.

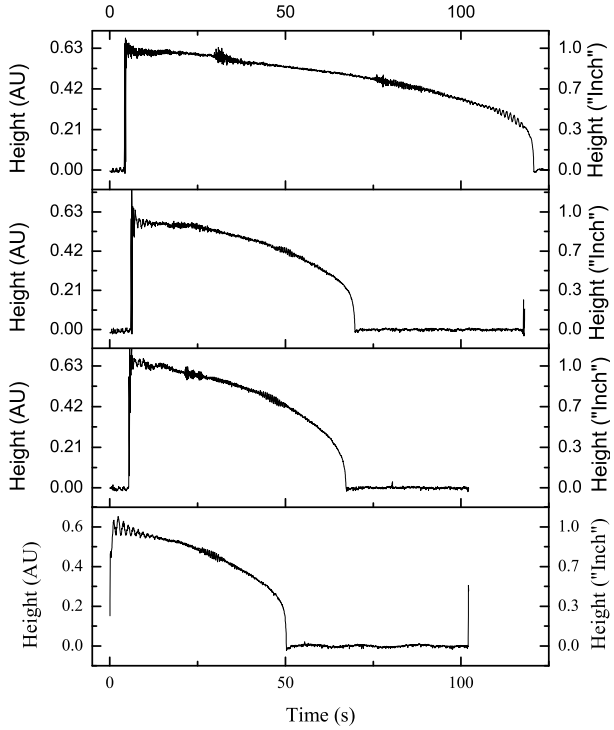

Figure 3-13. The motion traces in this figure were extracted from the video of the armature motion shown in the figure above. These three figures show a lowering of the armature in the experimental cell at varying speeds.

3.3.1.2 Results with inductive position sensor

After the mixed results with the motor tests in the optical dewar, an accurate position sensor and a more stable working environment. For the latter, a non-optical helium dewar which does not contain a evaporating nitrogen jacket was used. In this dewar, all of the helium bubbles can be suppressed by applying an external pressure (above T_λ) or pumping below the superfluid transition where cavitation is no longer present. An inductive position sensor was designed and wound to fit around the actuating Nb. The inductive technique has the advantage that it does not depend on the radial location of the Nb and has a sensitivity of the order of the diameter of the wires used in its construction. A photograph of the position sensor is shown along side the capacitive sensors in Figure 3-11. The inductive position sensor works by changing the magnetic susceptibility of the space inside the solenoid as the superconductor moves. The inductance, L, of a solenoid can be calculated by the formula,

$$L = (1 + \chi)A\frac{u_o N^2}{\ell}. \tag{3–31}$$

As the superconductor moves, it fills more (less) of the solenoid causing a decrease (increase) in inductance. In this equation χ is the susceptibility of the material inside the position sensor, A is the cross sectional area of the coil, μ_o is the permeability of free space, N is the number of turns in the solenoid, and ℓ is the solenoid length.

The first tests of this apparatus were conducted at 4 K . For these, the quadruple bearing magnets were temporarily abandoned due to the confined geometry of our cryostat, as these experiments were conducted in the suckstick apparatus. The experimental apparatus is shown in Figure 3-14. These experiments were designed to proceed with the same experimental procedure as the previous tests in the optical dewar without the interfering mechanical effects of a boiling nitrogen jacket. The motor apparatus was the same design as previously discussed, with the exception that the drive coil length was increased. The new drive solenoid is 10 layers of superconducting

wire, rather than 4, and the length of the solenoid was increased from 55 mm to 65 mm. The longer coil limited the motor traverse to 20 mm while never allowing the bottom of the Nb to enter the positive field gradient of the magnetic field. In other words, the magnet coil was made $10\ mm$ longer and the starting location for the Nb was moved to the center of the solenoid. The additional layers wound on the drive magnet allowed it to operate at lower currents and achieve the same magnetic field. With a smaller current, a smaller shunt resistor could be used, fitting better the parameters.

For these tests, the current to the drive was discreetly, rather than continuously, adjusted to move the armature a set distance. After each change in position the stability of the motor was examined. This method of motion produces a stepwise change in the armature position with time, which can be used as a calibration for the equilibrium current of the motor system as a function of position. A typical trace of this data is shown in Figure 3-15. These data were taken without the presence of a shunt resistor and therefore without a source of dissipation. After a new current level is delivered to the drive, the armature approaches the equilibrium position, overshoots it, and oscillates around that position with a very weakly damped sinusoidal decay. This can be seen in the inset Figure 3-15.

Recording the current required to hold the armature in each location revealed information about the magnitude and derivative of the Meissner force on the levitated Nb rod. The calculated frequencies are derived by treating the Nb as a mass on a spring where the spring constant $k = \frac{dB}{dz}$ and the frequency is $\omega = \sqrt{k/m}$. The measured equilibrium position as a function of drive current is shown in Figure 3-16 and compared to the prediction.

After mapping out the solenoid field and forces on the armature, the motor was ready to be tested in the operation mode described in the theory. Upon beginning this work, a curious effect became evident; the armature no longer oscillated after it moved, and changes in current no longer produced predictable changes in armature location.

These data are shown in Figure 3-17. Unlike with the previous motor motions, Figure 3-15, the size of the steps in this plot appear to have a random and unpredictable distribution of size and are strongly hysteretic. So what has changed? The Nb must have been exposed to a field above B_{C1}. Therefore in Figure 3-17 fluxons must have penetrated the superconducting cylinder. The penetration of flux in these experiments appears to be a gradual effect. Figure 3-18 shows 3 consecutive motor motions with identical current inputs. In this figure, the first motion, when the Nb is still virgin and not yet exposed to a field is shown in black and on top of the other two curves. The red and blue curves below are subsequent runs and it is observed that the amplitude of oscillations on these runs decease. Each time the motor is run, the motion appears more stable. This is attributed to the progressive increase of trapped flux in the armature and the dissipation associated with magnetic vortices moving through a magnetic field. Also shown in this plot is the drive current as a function of time. In this experiment, the magnetic field around the armature was never raised above the calculated zero temperature field, so it is postulated that the magnetic penetration occurred due in part to the geometry of the ends of the Nb cylinders.

The Nb cylinders used in this work were capped with machined Nb stoppers so that the superconductor would be one closed cylinder with no location for the field to penetrate the interior of the cylinder, and therefore maximizing the Meissner force. However, it seems likely that the machined Nb caps and their sharp features are nucleation sites for magnetic flux in the bulk superconductor. A recent paper on type-2 superconductors [83] shows minimal field leakage into a hollow superconductor of similar aspect ratio to the one used here. This is true even for DC fields. Therefore, the removal of the end caps from our system should not introduce a large amount of degradation of our Meissner force because the magnetic field will not sag into the interior of the superconductor. This statement implies that the superconductor will expel

flux in the absence of a closed geometry and the end caps used in this experiment are superfluous.

To examine this proposition, the end caps were removed from the system and the motor was once again cooled to 4 K. Figure 3-19 shows measurements of the current vs. position of several motion paths of an uncapped armature. Similar to Figure 3-17 and 3-18 there is evidence for presence of trapped flux. This implies that the source of trapped flux was not entirely the machined end caps. This set of tests show that the motor can operate without the massive Nb caps even though the trapped flux does not allow proper motor tests. These data, Figure 3-19, are presented in a different way. They show the position changes vs. input current to the drive coil for several different motor motions rather than just motion vs. time. This allows for a more in depth understanding of the system.

For each subsequent motion, the motor requires a larger current to both initiate movement and to travel across the experimental space. This is seen by looking at the black, red, then green lines, respectively. In this plot the black motion is first, followed by red and green. Each shift to the right on the plot represents a larger input current for the armature to move to the equilibrium position. The drive current is flipped and the motion initiates at a lower current, seen in the cyan colored trace. The current in the drive is then flipped again (back to the original) and the blue data are collected, showing smaller motions for the same current. The reduction of motion for a given current and an obvious magnetic polarity effect strongly suggest the the problems with this motor are due to trapped magnetic flux. This experiment also showed that, even without the obvious nucleation sites on the machined end cap this motor can not be reliably operated at atmospheric pressure helium temperatures (4 K). This plot also shows that in the event that magnetic flux does penetrate the superconductor, it grows with repeated motion through a magnetic field. However, the critical field of Nb rises substantially between 4 and 1 K (Figure 3-20), so the temperature of this apparatus can be lowered to avoid

trapped flux. These tests at 4 K give a good description of what motion will look like with trapped flux, so that after lower temperature tests this effect can be looked for.

Figure 3-14. This is a photograph of the apparatus used to test the motor in the suckstick cryostat. The position of the armature in the experiments with this motor were measured with the inductive sensor at the bottom of the figure.

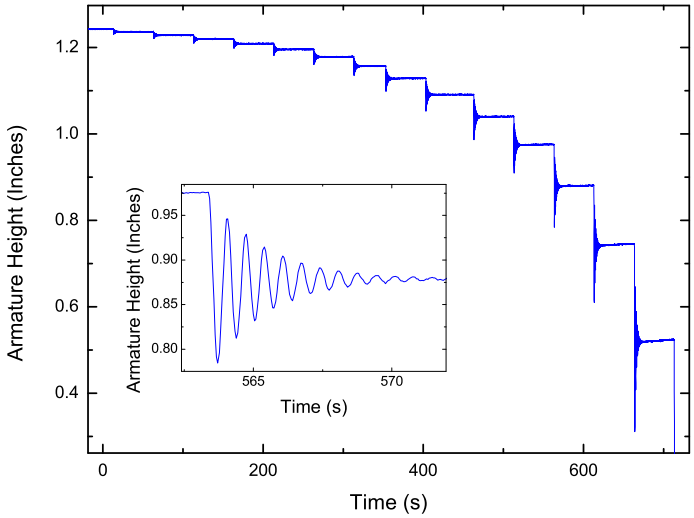

Figure 3-15. This figure shows the motion of the armature as a function of time for equal stepwise decreases in current as a function of time. After each discrete change in position the armature is seen to follow a damped ring down. This is shown or one such step in the inset of the figure.

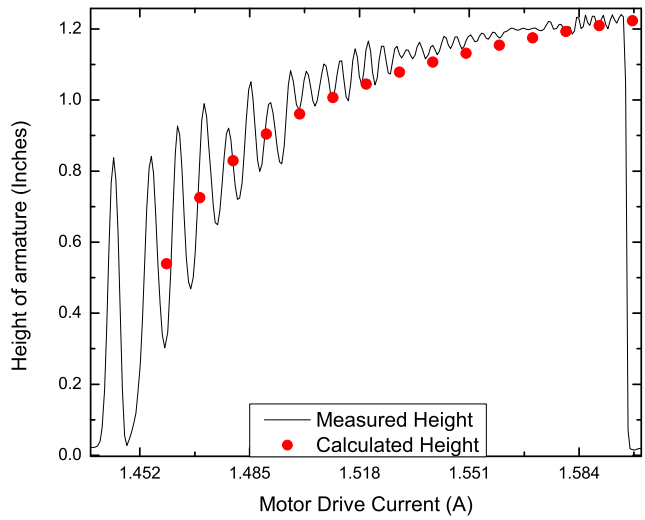

Figure 3-16. This figure compares the calculated and measured armature height as a function of motor drive current. The experimental data in this figure were obtained by linearly ramping the current as a function of time and the calculated data are the results of setting the sum of the gravitational and Meissner forces to zero.

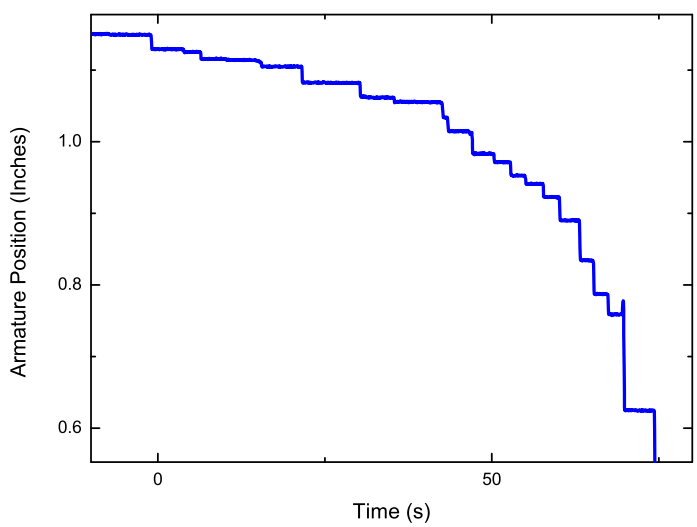

Figure 3-17. This data trace shows the armature response for discrete changes in drive current (similar to Figure 3-15) as a function of time. In this plot, unlike the previous one, there is no ring down behavior or predictable armature motion.

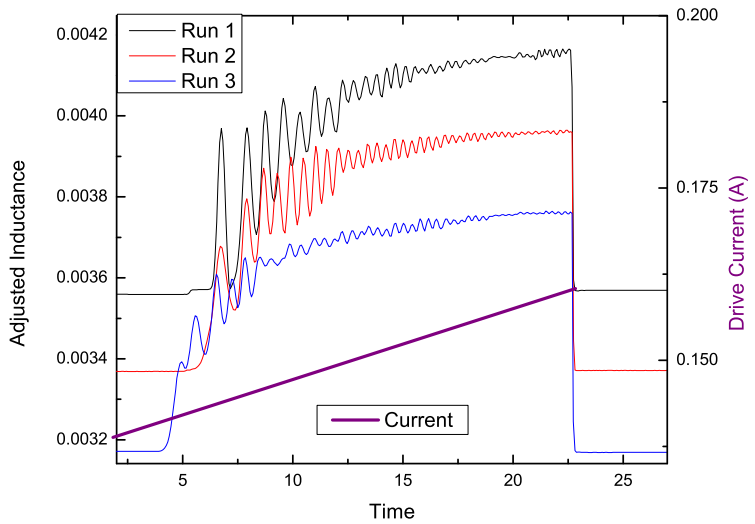

Figure 3-18. The data in this figure show the motion from three consecutive motor motions generated by identical ramps in the applied current. These plots clearly show a noticeable decrease in the oscillatory motion of the armature for identical applied current profiles.

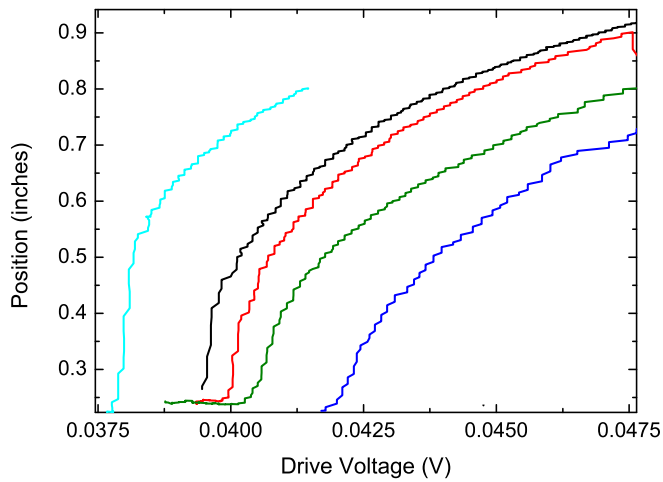

Figure 3-19. This figure shows evidence of trapped flux in the niobium cylinders without endcaps. The data was collected by repeatedly applying identical current ramps (except for the magnetic polarity which was switched twice). The data in the black trace were the first collected with a virgin niobium rod. After a few current ramps, a noticeable decrease in armature position compared to drive current is observed (red curve). Upon repeated current inputs the current profile drops to the green curve. After the drive polarity is switched, the data follow the bright blue curve, and once it is shifted back the data follow the dark blue curve.

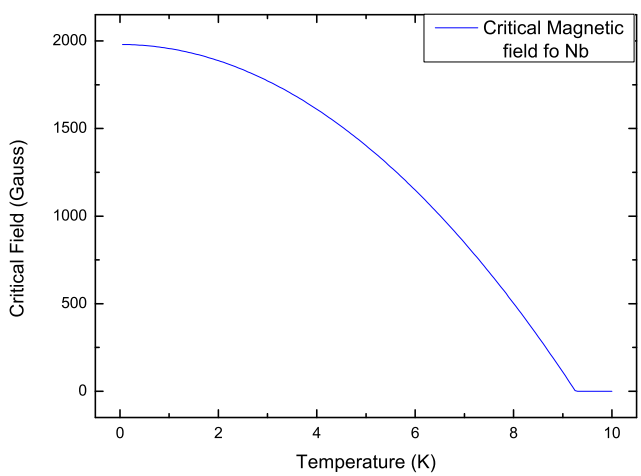

Figure 3-20. This plot shows the critical magnetic field of niobium as a function of temperature.

3.3.2 Initial Motor Tests at 1 K

The motor tests at 4 K made it clear that flux penetration into the superconductor is a problem and must be avoided to produce a motor that functions in a predictable way. The critical magnetic field of superconductors is temperature dependent [81],

$$H_{cb} = H_o[1 - (\frac{T}{T_c})^2]. \tag{3–32}$$

In this equation T_c is the maximum critical temperature, H_o is the zero temperature critical field, and H_{cb} is the specific critical field at the temperature T. Therefore, lowering the temperature will allow us to use higher magnitude fields without producing trapped flux. If the temperature is lowered from 4 to 1 K, the critical field is raised by nearly 20% for Nb. To do this, the Nb cylinder was cycled above the superconducting transition clearing any trapped flux; then the temperature was lowered to 1 K by evaporative cooling of the helium in the suckstick. At this temperature, the same experiments were performed as in Figure 3-18. The results are shown in Figure 3-21. The reproducibility of these motions is obvious, especially when compared to the 4 K data. The oscillations in this figure were reduced by ramping the current at a slower rate (no additional internal damping). These data are from over 20 different motor runs and there is no indication of trapped flux. To check this, the polarity of the drive coil was reversed to look for a shift of the calibration as was seen in Figure 3-19. In Figure 3-23, nearly half of the data are of one magnet polarity, while the other half are of the other. Unlike at 4 K, the motion at 1 K is independent of both motor history and drive polarity ultimately suggesting that there is no or negligible trapped flux. Note that with the Meissner effect the force is $\propto B^2$, so the polarity of the drive should be independent of the armature dynamics. However, if the superconductor has been penetrated, the trapped flux does have a polarity and is dependent on field direction.

At this reduced temperature, it is clear that the necessary magnetic fields to actuate a Nb cylinder are produced and maintained without changing the superconducting state.

With this preliminary work accomplished, the motor was then tested to produce various linear motion patterns. This experiment was designed to characterize the motor system, and verify that future work will be possible with these motor dimensions. Therefore, there is no shunt resistor present and the operation procedure outlined earlier in Chapter 3 is unapplicable. While the system remained cold, rather than warming up and starting again, linear velocity profiles were attempted without the resistor using a different technique.

This technique uses a current ramp in time such that the equilibrium position of the armature moves with a constant velocity, rather than instituting a stepwise change to the drive current. The current input is shown as an arbitrary function of time in Figure 3-21.

Data from these experiments are shown in Figure 3-22. In this figure, $z = 0$ is the center of the drive solenoid and increasing position correlate to the Nb moving upwards and out of the drive. These data are quite encouraging for driving the motor. Over a distance of nearly $0.5''$ a linear motor motion is observed. This motion is concentrated on the positions where the magnetic field gradient is relatively large. Therefore, running the motor in this operation mode has the opposite ideal specifications as the method described in the theory. For this type of motor motion a large magnetic field gradient is used to hold the armature in a moving potential well, as opposed to the original design where the motor is provided an impulse to increase its momentum before it moves through a force free region. In the operation procedure here the field gradient in the center of the coil, $-\frac{dB}{dz} \sim 0$ has very poor control over the motor motion and at the top when $-\frac{dB}{dz}$ is maximal the motion is very well controlled and linear. This is simply visualized by observing that at small values of z, in the coil, very small changes in current move the equilibrium position a great distance where near the top, a relatively larger current change is needed to move the armature a short distance. Several different motor motions are produced with this new actuation principle and are shown in Figure 3-23.

After fully exploring this motor without a shunt resistor present and this new actuation method, a shunt resistor was soldered parallel to the drive to explore its effect and the motor operation as designed. Figure 3-24 depicts three different motor motions, with three different resistive shunts. The velocities of the motor in this figure range from $80\ mm/s$ to $27\ mm/s$, the faster of these speeds approach the goal of $100\ mm/s$. However, if the speed of the motor is increased as in Figure 3-25, a large oscillation is routinely observed. For reference, the current step used for Figure 3-25 is shown in Figure 3-26. The oscillations atop Figure 3-25 were found at the end of all inertial motor motions with speeds above $\sim 80\ mm/s$, regardless of shunt resistor, current step size, or length. In addition, for a good brake after a motor traverse, the inertial motor design is not well suited for motor motions much slower than $10\ mm/s$, because of the inherent instabilities of a very weak potential well. In the end, the requirements of this elegant method are too great for its practical use and the force holding the armature after the motion is too weak. Therefore a new design was developed.

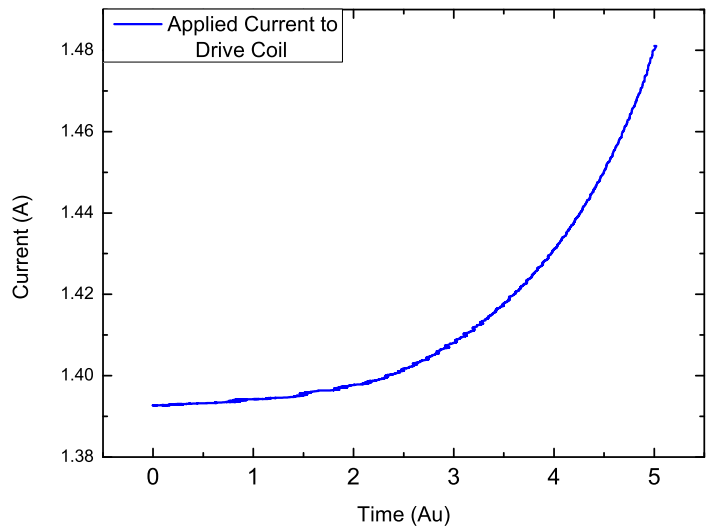

Figure 3-21. Current input to the drive coil required to produce linear movements in time for the inertial motor run without a shunt resistor. The time for this current ramp depends on the rate at which the motor moves.

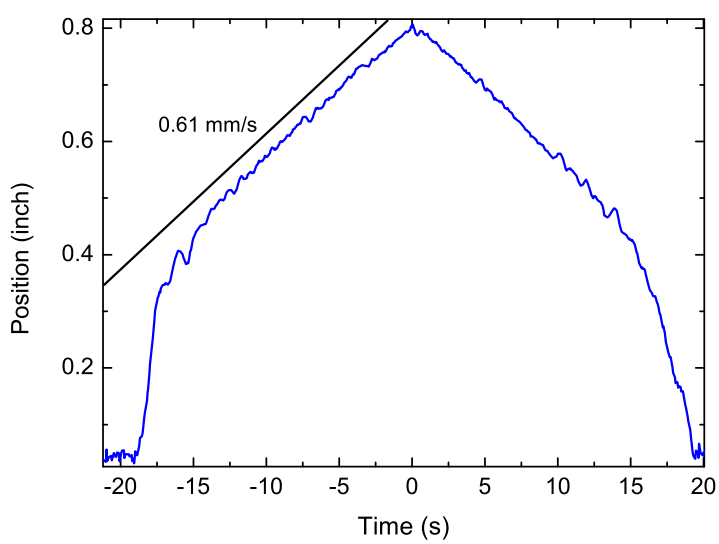

Figure 3-22. One typical 'linear' motion for the motor at 1 K. The grid velocity for this particular motion is $0.61\ mm/s$

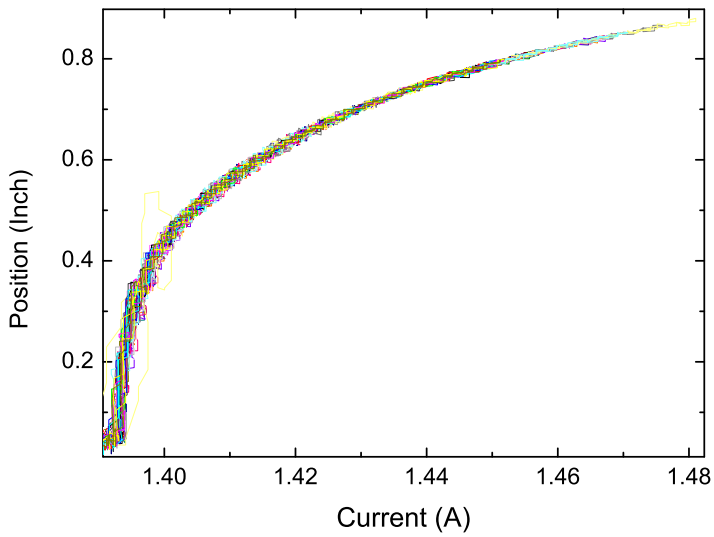

Figure 3-23. This figure shows the reproductivity of equilibrium motor positions over the course of many motor motions at 1 K. Roughly half of the motions in this figure are for a positive current drive, while the other the drive current is negative.

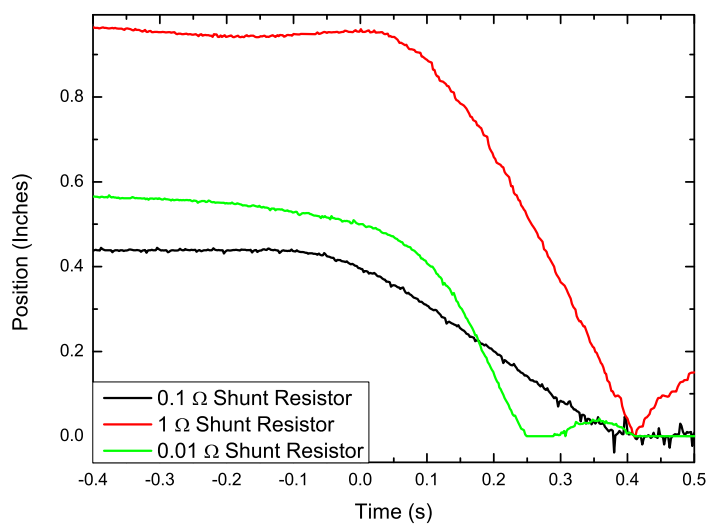

Figure 3-24. This figure shows the position of the niobium as a function of time for different shunt resistors when the motor is run according to the inertial motion theory.

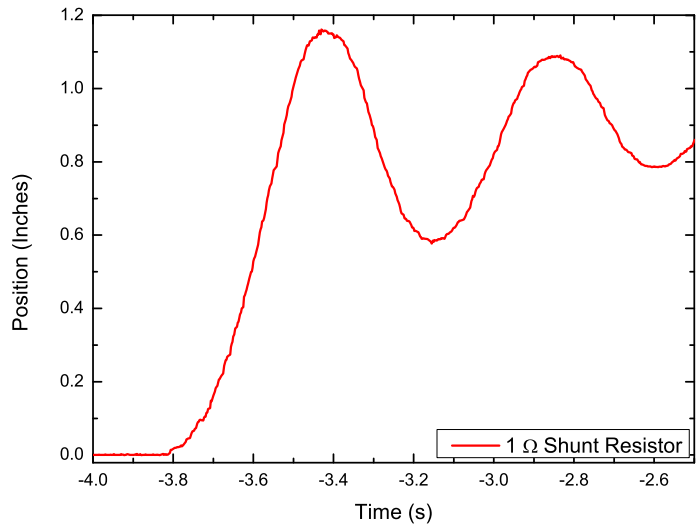

Figure 3-25. This plot shows the motion of the inertial motor with a 1 Ω shunt resistor when the armature is traveling in the opposite direction as gravity.

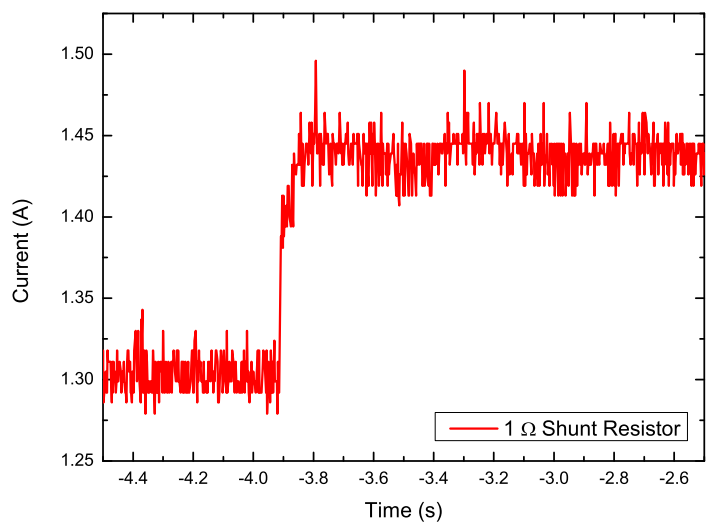

Figure 3-26. This plot shows the current step used to create the motion in the inertial motor.

3.4 Control Motor

After spending a considerable amount of time working out the operating procedure of the inertial motor, the limitations of the design instigated a new drive system. This design is similar to the inertial motor, in that long solenoids and controlled magnetic fields are used, but with the control motor the magnetic field gradient was specifically chosen rather than the B field itself. This change in the field structure allows more flexibility and continuity in the operation of the drive system. This design used a similar mathematical formalism to the one outlined in sec 3.3, but it is complicated by allowing a constant change in current as a function of time and a non-constant field gradient. A change in the coil design was required to create this new magnetic profile. The design and construction of this coil is outlined in subsection 3.4.1, the mathematical model in 3.4.2, and results in 3.4.3. The principle of the control motor is that during the linear motion of the armature, both the magnetic field at the bottom of the armature and the field gradient in the same location are constant in time. This will lead to a constant mechanical resonant frequency ($\omega = \sqrt{k/m}$) of the armature in the drive solenoid, which can be matched to the resonant frequency of the RL circuit.

3.4.1 Control Motor Design

The new magnet arrangement was needed to create the field profile dictated by the 'control' design. The requirements of this motor design are; the derivative of the force field needs to be constant in z, the input current to the motor should have a mathematically simple form (either linear, constant, or a Heaviside profile) in order to provide a constant force on the armature as it moves, and the design should be simple with as few different circuits as possible. There were several theoretical models created for such a coil. Two are reviewed below.

The first attempt at creating a field profile of this type was by winding a step pattern on top of a uniform field solenoid. The field gradient is decided by the number of winding layers along the drive solenoid.This process arranges several solenoids along a line,

each with a different field and superimposes those fields together. A cartoon schematic of such a system is shown in Figure 3-27; a calculation of the magnetic field is shown in Figure 3-28; and the corresponding Meissner force in Figure 3-29. The adjustable parameters for a design such as this are the number of steps, their size, both in number of layers and width, and the step location. From these figures, it is clear that with proper locations of steps and the number of windings, a custom coil can be created that produces a linear variation magnetic field as a function of position. The derivative of the force field as a function of position is shown in Figure 3-30. This coil design is promising, except that changing the current during operation to actuate the armature also changes the derivative of the field. This is because when the current is increased (decreased) the low z magnetic field is raised (lowered) disproportionately to the low (high) z magnetic field, leading to a non-constant dF/dz as a function of current. Because of this, the step motor coil design is not ideal and was not pursued further.

The failing of the stepped solenoid design led to a loosening of the simple circuit requirement and two separate coils with individual current sources are used. This system requires one extra set of lead wires, but still only needs one varying current input. This motor was created by placing an anti-Helmholtz coil around the $65\ mm$ drive coil used in the previous design. With this double layer design, the anti-Helmholtz current is maintained at a constant value, providing a constant dB/dz, while the long solenoid has its current raised and lowered to change the magnitude of the B field. A schematic of the magnetic coils is shown in Figure 3-31 and a photo of the apparatus is shown in Figure 3-32 and the machine schematics are shown in Figure A-8. The magnetic fields of each of the coils in the anti-Helmholtz pair and their relative positions are shown in Figure 3-31, where the two large humps are the two coils of the anti-Helmholtz pair and the smaller hump is a central compensation coil for the $65\ mm$ solenoid. Figure 3-33 shows the sum of the individual anti-Helmholtz fields along with the drive coil, and Figure 3-34 shows the force profile of this coil. In these figures, the

Table 3-2. Control Motor Coil Parameters

Object	Dimension	
Drive Solenoid Radius	7.5	*mm*
Anti-Helmholtz (AH) Radius	22	*mm*
Drive Solenoid Compensation Coil Radius	22	*mm*
Drive Solenoid Length	65	*mm*
Drive Solenoid Wire Layers	10	Layers
Drive Solenoid Position	0	*mm*
Positive AH Length	12	*mm*
Positive AH Wire Layers	13	Layers
Positive AH Position	0	*mm*
Negative AH Length	11	*mm*
Negative AH Wire Layers	20	Layers
Negative AH Position	48	*mm*
Compensation Coil Length	17	*mm*
Compensation Coil Wire Layers	2	Layers
Compensation Coil Position	24	*mm*
Wire Diameter	0.19	*mm*

current in the anti-Helmholtz is 2.5 A and the current is 1.5 A in the long drive solenoid. During operation the current in the drive solenoid is variable, but one particular value was chosen for these plots. The various parameters of the drive system are given in Table 3-2 and the schematic is shown in Figure 3-31.

With these parameters from Table 3-2, the current input into the drive solenoid for different, constant, anti-Helmholtz currents can be calculated. These are presented in Figure 3-35. and the effective spring constants produced by the same anti-Helmholtz currents can also be calculated as a function of position. These are presented in Figure 3-37. These calculations show that the field profile required for this theory can be created. As in the theory of the inertial motor, the shunt resistor will be placed across the long drive solenoid to damp the oscillations of the armature. Since the anti-Helmholtz solenoids maintain a constant current, the dissipation through them is trivial and small, due to their large radius. The mathematics of the armature interaction with the drive solenoid and the dynamics of the motor motion are expanded on in the next section, 3.4.2.

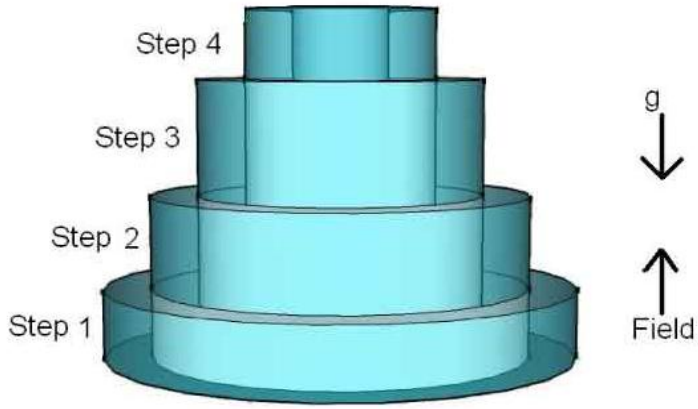

Figure 3-27. This figure shows a cartoon of the first control motor drive coil conceived.

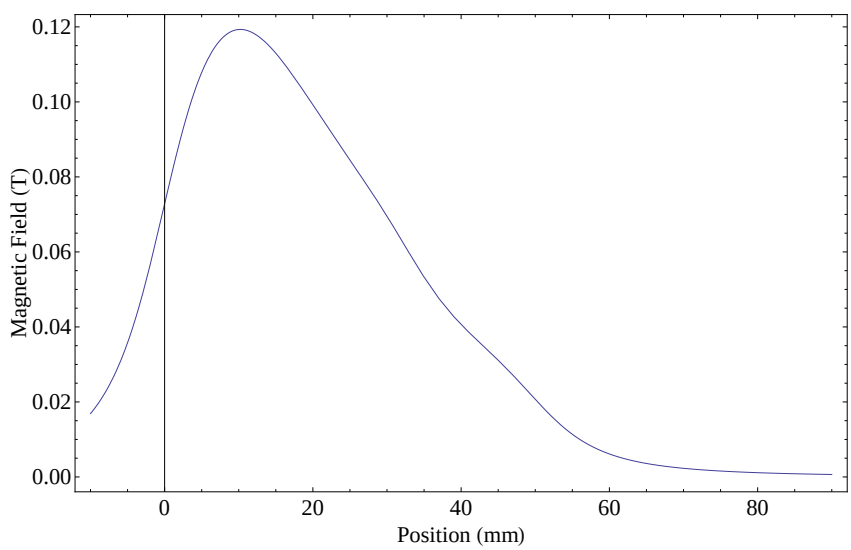

Figure 3-28. This figure shows the calculated magnetic field produced by a stepped motor design.

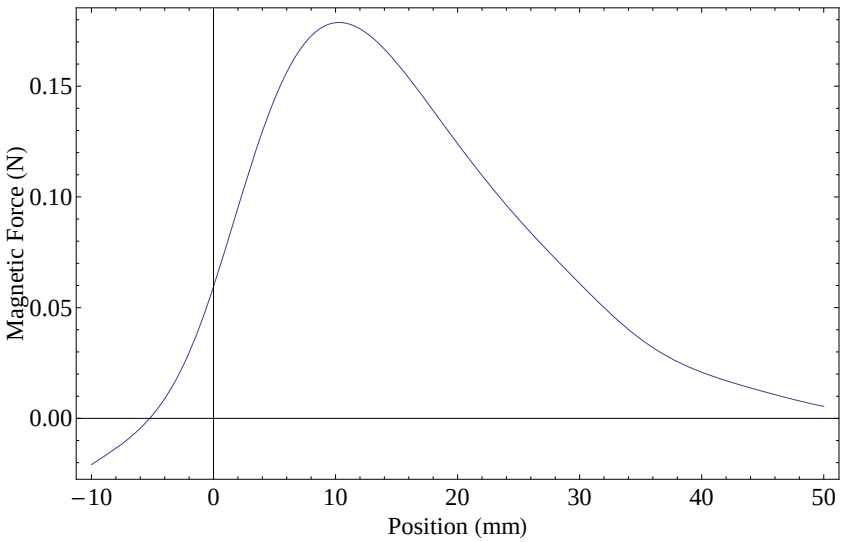

Figure 3-29. This figure shows the calculated force profile produced by a stepped motor design.

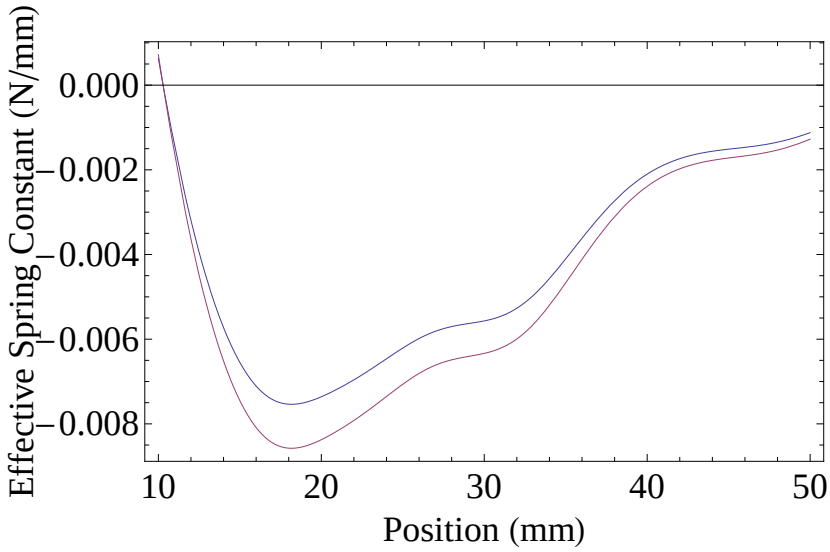

Figure 3-30. This figure shows the nonconstant derivative of the magnetic force for a stepped coil design for a changing drive current.

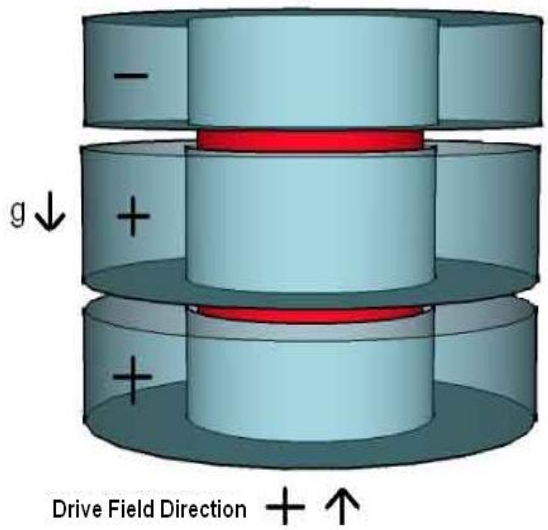

Figure 3-31. Schematic drawings for the anti-Helmholtz magnets. In this figure the inner red coil is the variable current drive solenoid and the outer three blue cylinders are the surrounding anti-Helmholtz coils.

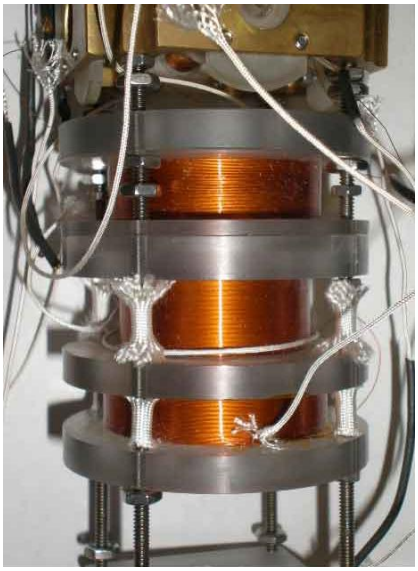

Figure 3-32. Photo of the anti-Helmholtz magnets

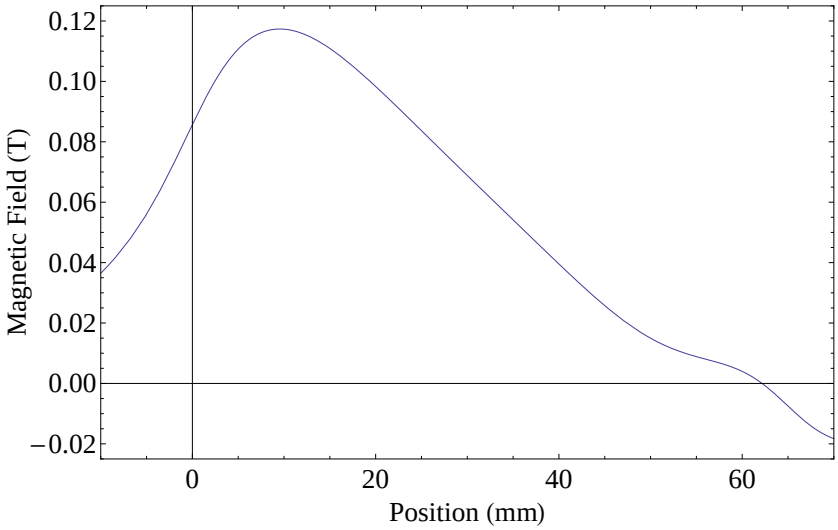

Figure 3-33. This figure shows the calculated magnetic field produced by a anti-Helmholtz motor design.

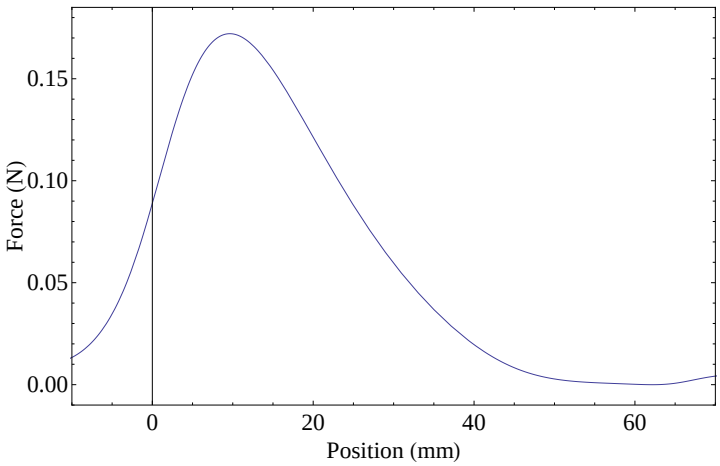

Figure 3-34. This figure shows the calculated force profile produced by a anti-Helmholtz motor design.

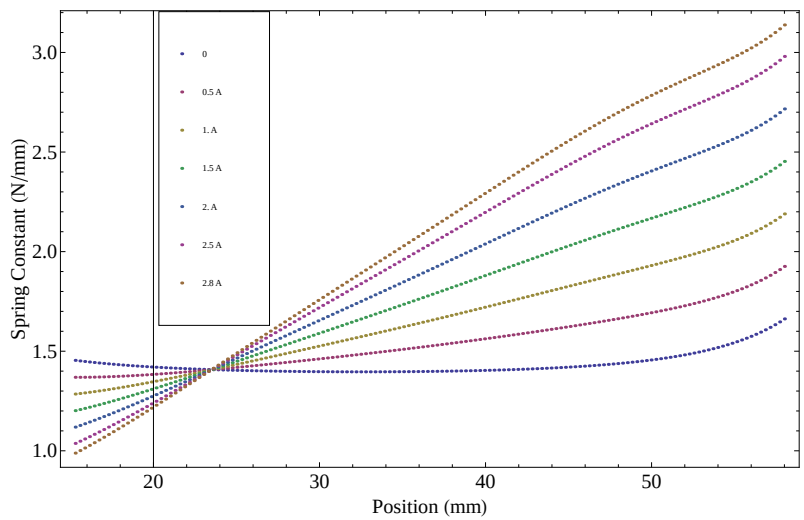

Figure 3-35. The calculated armature equilibrium currents vs. armature position

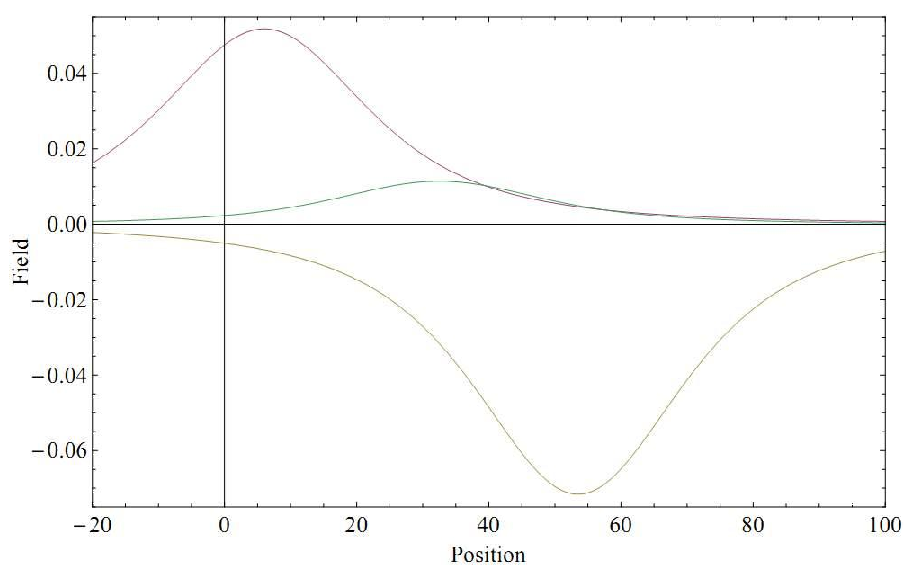

Figure 3-36. Calculated magnetic field inside each of the three solenoids of the anti-Helmholtz circuit

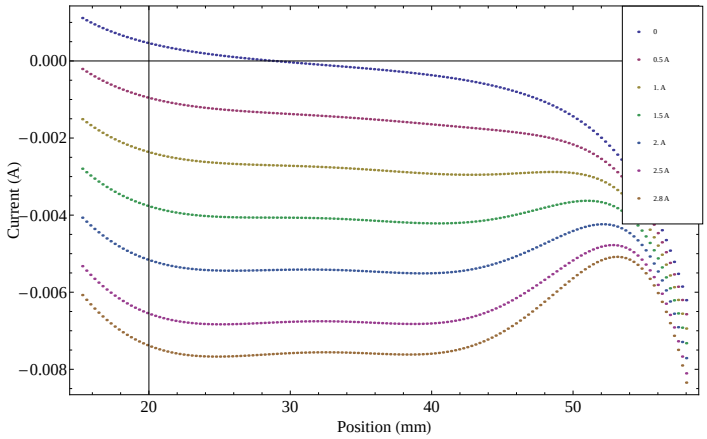

Figure 3-37. Calculated effective spring constants of the control motor vs. armature position for several different anti-Helmholtz currents

3.4.2 Control Motor Theory

The magnetic field inside an arbitrary coil can be defined as,

$$B(z) = \mu_o n I_L P(z) \tag{3–33}$$

where I_L is the current through the electromagnet, $P(z)$ is function of z describing the strength of the magnetic field along the center of the solenoid, and n is the turn density. The force on the Nb coils defined by Equation 3–14, and it is assumed that $B_T^2 << B_B^2$. When B is functionally dependent on z, Equation 3–8 is replaced by Equation 3–33, the new equation of motion is

$$m\dot{U} = \frac{1}{2}\mu_o n^2 A I_L^2 P^2(z) - mg. \tag{3–34}$$

The simplest solution for this equation (aside from $P(z) = C$, which is the ideal field used in Sec. 3.3) is when $P^2(z) = a + bz$. Here a and b are constants set by the construction of the coil. This is the form of the drive force shown in the previous section, Figure 3-34. By implementing this into the force equation,

$$m\dot{U} = \frac{1}{2}\mu_o n^2 A I_L^2 (a + bz) - mg. \tag{3–35}$$

This equation is solved to reveal the equations of motion for the control motor.

Like before, the mathematics are easier if the equations are solved for a shunt resistor of $R = \infty$. This will be worked out first, followed by a solution with a finite value of R. Define $z = 0$ at the bottom of the motor coil and assume that the armature starts from rest. Therefore, $0 = mg - \frac{1}{2}aI_o^2 A n^2 \mu_o$, implying that $a = \frac{2mg}{\mu_o n^2 A I_o^2}$ where I_o is the current in the drive solenoid such that the Meissner force and gravity are in a perfect balance. Suddenly, the current is changed at $t = 0$ and the motor will respond; the source current by construction will increase with a constant rate of γ:

$$I_a = I_o + \gamma t, \tag{3–36}$$

where I_a is the applied current. The force equation now becomes

$$m\dot{U} = \frac{1}{2}\mu_o n^2 A(I_o + \gamma t)^2(a + bz) - mg. \tag{3–37}$$

Because there is no shunt resistor, $I_a = I_L$ where I_L is the current in the inductor. The schematic of the electronics is the the same as previously shown in Figure 3-4. By expanding equation 3-4 we arrive at

$$m\dot{U} = \frac{1}{2}\mu_o n^2 A(I_o^2 + 2\gamma t I_o + \gamma^2 t^2)(a + bz) - mg. \tag{3–38}$$

The higher order terms are taken out, reducing to the form of a well known partial differential equation,

$$\ddot{z} + \widetilde{A}z = \widetilde{B}t, \tag{3–39}$$

where $\widetilde{A} = \frac{\mu_o n^2 A \alpha I_o^2}{2m}$ and $\widetilde{B} = \frac{\mu_o n^2 A \gamma a I_o^2}{m}$. The solution for this equation with the conditions $x(0) = 0$ and $\dot{x(0)} = 0$ is

$$z(t) = \frac{2\gamma a}{\alpha}(t - \frac{Sin(\omega t)}{\omega}), \tag{3–40}$$

where the frequency, ω, is defined by

$$\omega = \sqrt{\widetilde{A}} = \sqrt{\frac{\mu_o n^2 A b I_o^2}{2m}} \tag{3–41}$$

and the linear portion is defined by the non-homogenous solution. The data for this motor design are shown to match expectations in Sec. 3.4.3.1.

For the production of a linear low temperature motion and isotropic, homogenous quantum turbulence, a shunt resistor is introduced into the circuit, similar to Sec. 3.3. With the presence of this shunt, a direct source of strong damping is created. Defining the input current as $I_a = I_o + \gamma t$, the current in the drive solenoid is,

$$I_L(t) = I_a + \delta I_L. \tag{3–42}$$

The labels for the electronics in different parts of the apparatus are the same as used before and shown in Figure 3-4. Once again, we can calculate the current in the shunt

resistor as a result of the EMF due to the traveling superconductor:

$$\frac{LI_L}{dt} = R(I_o - I_L) = R(\gamma t - \delta I_L) \tag{3–43a}$$

$$L\delta\dot{I}_L + (I_o + \delta I_L)\dot{L} = R(\gamma t - \delta I_L) \tag{3–43b}$$

and from Equation 3–9 we can extrapolate that to lowest order

$$\dot{L} = \frac{nAU(\mu_o n I_L \sqrt{a}\sqrt{1 + bz/a})}{I_L} \simeq \frac{nAU(\mu_o n I_L \sqrt{a})}{I_L}. \tag{3–44}$$

Putting these equations together yields

$$L\delta\dot{I}_L = R(\gamma - \delta I_L) - A\mu_o n^2 a^{1/2} I_o U. \tag{3–45}$$

Taking Equation 3–37 to first order, it can be reduced to

$$m\dot{U} + \frac{1}{2}\mu_o n^2 A b I_o^2 z = \mu_o n^2 A I_o a \delta I_L. \tag{3–46}$$

Using the standard electromagnetic machinery introduced above and solving for δI_L we arrive at

$$\delta I_L = \frac{m}{\mu_o n^2 A I_o a}\dot{U} + \frac{bI_o}{2a}z \tag{3–47}$$

which has a derivative of

$$\delta\dot{I}_L = \frac{m}{\mu_o n^2 A I_o a}\ddot{U} + \frac{bI_o}{2a}U. \tag{3–48}$$

Substituting in Equations 3–47 and 3–48 into Equation 3–45, a second order partial differential equation is obtained:

$$\frac{Lm}{\mu_o n^2 A I_o a}\ddot{U} + \frac{LI_o b}{2a}U = R\gamma t - \frac{Rm}{\mu_o n^2 A I_o a}\dot{U} - \frac{RI_o b}{2a}z - A\mu_o n^2 a^{1/2} I_o U, \tag{3–49}$$

Differentiating Equation 3–50 by t and rearranged gives

$$\dddot{U} + D_1\ddot{U} + D_2\dot{U} + D_3 U = D_4. \tag{3–50}$$

Here $D_1 = \frac{R}{L}$, $D_2 = \frac{\mu_o n^2 A I_o a}{Lm}(\frac{L I_o b}{2a} + A\mu_o n^2 a^{1/2} I_o)$, $D_3 = \frac{R b \mu_o n^2 A I_o^2}{2Lm}$, and $D_4 = \frac{\mu_o n^2 A I_o a \gamma}{\tau m}$. The homogenous solution for this equation is $U(t) = C_1 e^{-\alpha_1 t} + C_2 e^{-\alpha_2 t} + C_3 e^{-\alpha_3 t}$ and the complete solution including the additional constant is

$$U(t) = C_1 e^{-\alpha_1 t} + C_2 e^{-\alpha_2 t} + C_2 e^{-\alpha_3 t} + \frac{2\gamma a}{b I_o}. \tag{3–51}$$

The constants α_i are the solutions to the cubic root equation defined in the differential equation. The solution to this equation is cumbersome and will not be reported, but the leading order real component is equal to $R/3L$ for each α_i with several additional real and complex terms following. The leading order term gives an idea of the rate of approach to the constant velocity solution as the oscillator components decay.

The above exercise quantitatively describes the simplified motor system to high precision. However, during operation, our motor system is not always inside the bounds of our assumptions, particularly when the current is ramped quickly. As the “small” terms increase and become important in the electro-magnetic calculations, the differential equations above become non-linear and unsolvable. Because of this, it is educational to remove ourselves from the rigorous electro-magnetic calculations above and examine the forces on the armature at any given time, to gain some intuition on the motor operation for varying current ramp speeds.

With a constant field gradient on one end of the armature at all times, both the Meissner force and the equilibrium oscillation frequency of the armature is unchanged throughout its traverse when the current is ramped at the proper speed. Using Equation 3–14 to calculate both the levitation force on the armature at any given time, and the use of mathematica, the motor can be effectively “simulated” as a function of a given current profile. With the use of a simple model, a moving mass on a spring, the hassle of formal circuit calculations and the simplifying assumptions required may be circumvented.

To qualitatively visualize this concept, the Nb armature sits in the bottom of a potential well defined by the field gradient and the Meissner force. If dF_z/dz is constant

in z, then the potential well is a perfect quadratic well defined by the coil geometry. From here it is simple to visualize a potential well traveling at some given velocity U along with the armature. The Nb actuator is pushed along by the upward sloping and trailing edge of the well, always maintaining the distance behind the well minimum required to produce the motive force. The Nb will oscillate with the frequency defined by the well until the motion of the well has stopped. At this time the Nb will decay into the bottom of the potential. In this picture the oscillation frequency is calculated by the forces and matched as the current in the drive coil is driven into the shunt resistor. Therefore, if the R/L time constant of the dissipation circuit is matched to the oscillation frequency of the actuator, the oscillations after the run can be critically damped.

3.4.3 Control Motor Experiment

These experiments were conducted using the same insert as the glass dewar experiments, Figure A-3. The dewar used for these experiments was a standard super insulated helium dewar which can be externally pumped, reducing the temperature to about 1.3 K. The majority of the data presented in this section were taken with a 1" long position sensor, used previously. However, for the longer motions a new 1.5" copper wound coil was used to give a longer range of sensitivity. A photo of this coil is shown in Figure 3-38 and its calibration is shown in fig 3-39. For these experiments, quadruple bearings are used and shown in Figure 3-40. A photo of the system is shown in Figure 3-32. Several different experiments were conducted using this apparatus, including motor operations with, with a 0.01 Ω, a 0.1 Ω, and a 1 Ω and infinite shunt resistor.

Each of the data sets was collected by the same methodology. Initially, the motor motion is created by slowly increasing the drive current over time. From these data, the current vs. inductance is extracted and compared to the inductance position calibration. From here, a data file is created which will input a linear change in equilibrium positions as a function of time. These are calculated and plotted in Figure 3-35 for several different anti-Helmholtz coil currents. With an input file expressing the currents required

for linear motion, the rate at which this file is read dictates the speed of the motor traverse. For exceptionally fast motor motions $\sim 20 - 30\ mm/s$ the input current profile is similar, but not exactly, the same as described in the inertial motor section, 3.3, as the motion is too fast to read in the entire input file. These data are presented below and divided by the size of the shunt resistor.

Figure 3-38. This is a photograph showing an inductive position sensor

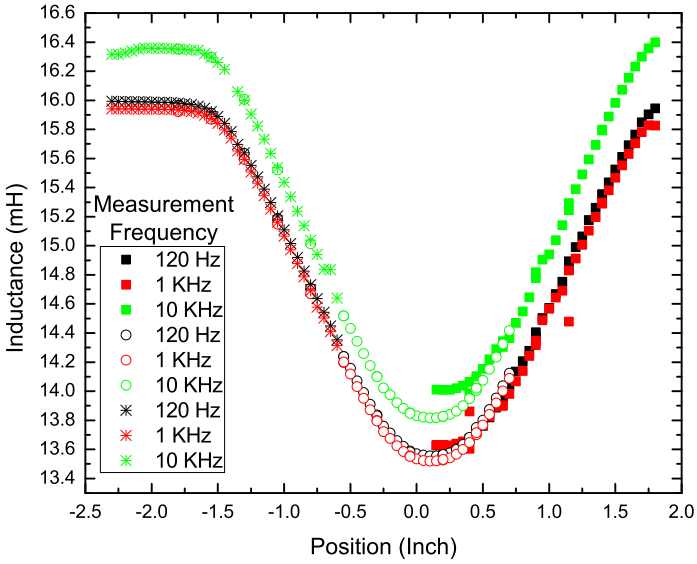

Figure 3-39. This figure shows the position calibration for a 1.5 inch solenoid. Recorded in the figure are the inductances measured with a LCR bridge at 3 different frequencies.

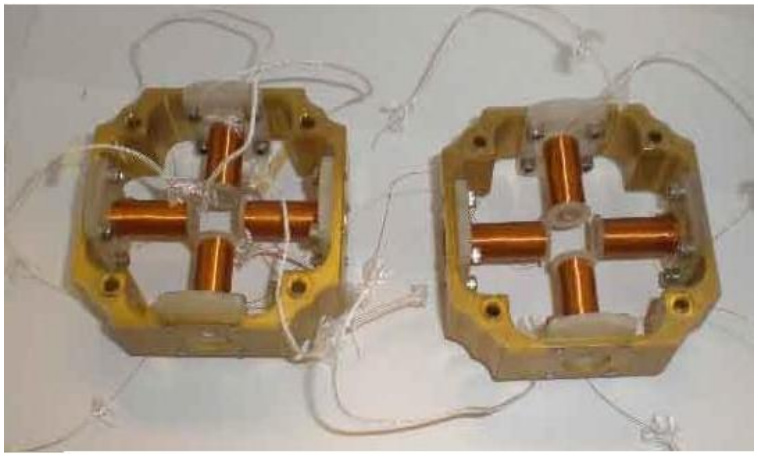

Figure 3-40. Photograph of quadruple magnets and their mounts

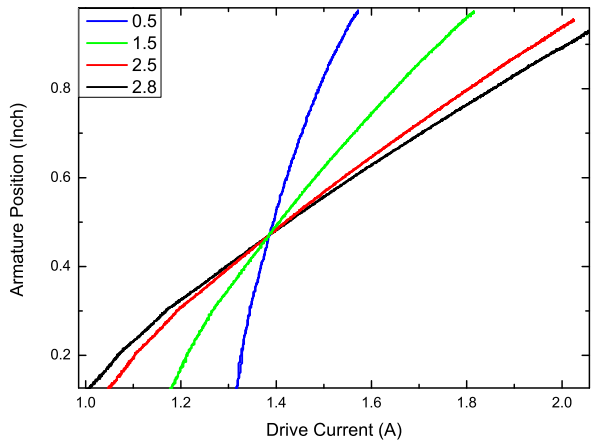

Figure 3-41. This figure shows the measured data of the equilibrium positions of the control motor, without shunt, as a function of drive current.

3.4.3.1 Shunt resistance = 0

The motor apparatus was cooled down to 1.2 K with no shunt in the drive circuit. The quadruple solenoids and the anti-Helmholtz coils were driven by a Hewlett Packard Harrison 6303B, 0-7.5V, 0-3A DC power supply, the drive solenoid is driven by the same BOP as previously mentioned and the data is collected by a combination of an Agilent LCR meter, Keithly volt meters, and a NI 6009 DAQ. The procedure is controlled by LabView software.

The slow ramping of the current as a function of time is shown in Figure 3-42. The raising and lowering of the armature was done very slowly, so that the armature remained in equilibrium with gravity and the levitating force. Motor motions are shown in Figure 3-42 and Figure 3-43 with speeds ranging from 1 mm/s to 20 mm/s. The data is arranged so that the motion start times for each run are coincident and the faster motions finish first while the slower take more time. The motion is shown to be linear in time, superimposed with a weakly damped sinusoid which was predicted in sec 3.4.2. As the motion becomes more rapid, the amplitude of the oscillations grows. This is intuitive, considering the theory of motion presented in Chapter 3 and predicted by the current ramp rate, γ, in the amplitude of the oscillation in Equation 3–40. The frequency generally appears to be independent or weakly dependent on armature velocity and location in the drive coil. There is a phase shift in Figure 3-44, due to the artificial shift in t used to ensure that the motions have the same initial start time.

Figure 3-44 isolates three separate motor runs shown in Figure 3-43. Two of these three motor runs have the same exact current input files and input rates applied to the drive current source. The motion is nearly identical in the two plots, showing a high level of reproducibility in our motion. The difference between the two motions is shown in the plot inset and appears to be electrical noise. The third plot in this figure is from a slightly different set of input data, where the input file is interpolated so there are 0.5 times as many points and the computer inputs the points at 0.5 times the rate. Comparing this

motor motion to the other two proves that the slew rate of the BOP and the output rate of the DAQ are not relevant to the motion of the armature at these velocities.

Upon increasing the current ramp rate to our motor, and therefore increasing the motor velocity, a strange behavior appears. At particular speeds the natural oscillation frequency of the motor system and the time scale for starting and stoping the motion appear to show evidence of a resonance. When the phase change of the natural oscillations matches the time scale of the motion, large oscillations at the stopping time are present and when the two are exactly 180° different in phase, there is nearly an absence of motor oscillations at the end of a motion. This is shown in Figure 3-45 as a train of separate motor motions operated at slightly different ramp speeds of 40 mm/s to 71 mm/s. The separation in time is added to ease the eye. It is clearly observed when looking at this train of motor motions that, depending on the phase of the motion, rapid decelerations are either possible or they induce large scale oscillatory motion at the end of the motion.

The interaction between the phase of the oscillations and the amount of time the motor travels can be used to produce linear motion profiles with fairly high velocities. Fig 3-46 shows one such tuned motion, where the travel distance for the armature has been reduced to coincide with the natural harmonics of the system. By using a system like this, a set of motor motions were produced for possible use in the study of quantum turbulence.

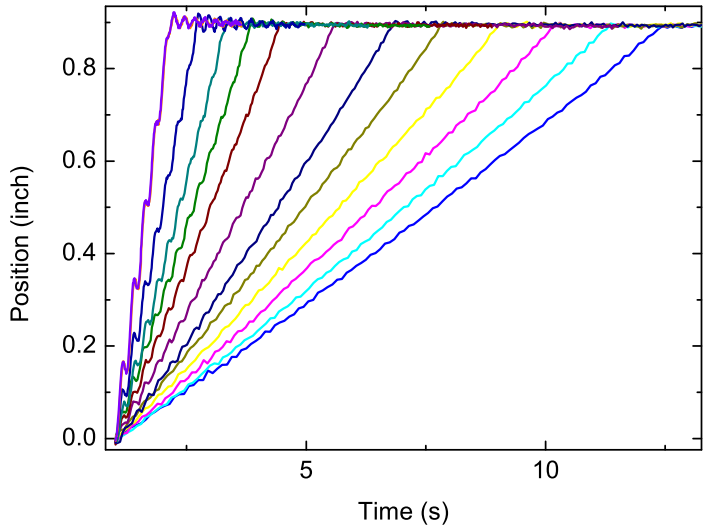

Figure 3-42. This figure shows slow motor motions with speeds ranging from 1-20 mm/s for the control motor with no shunt resistance.

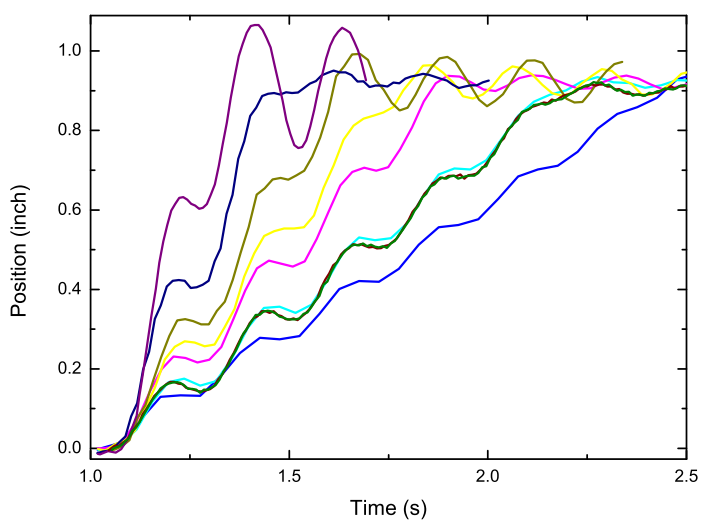

Figure 3-43. This figure shows motor motions with speeds ranging from 15-45 mm/s for the control motor with no shunt resistance.

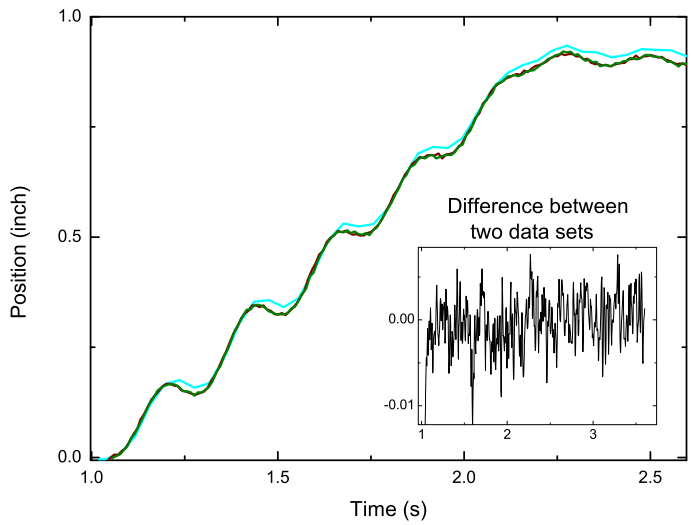

Figure 3-44. This figure shows three different motor motions. The two motor traces that lie on top of one another are motions from identical current inputs. Their difference is show in the figure inset. The third line on the figure shows the result of a similar current input, but with the drive profile delivered to the amplifier at half the speed.

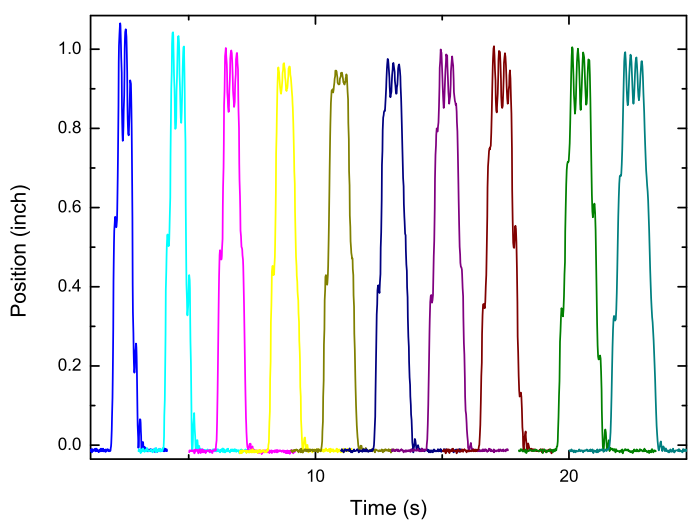

Figure 3-45. This plot exemplifies the effect observed when the integrated time of motor motion is an integer multiple of the resonance period of the armature at a particular anti-Helmholtz frequency set by $\omega = \sqrt{k/m}$.

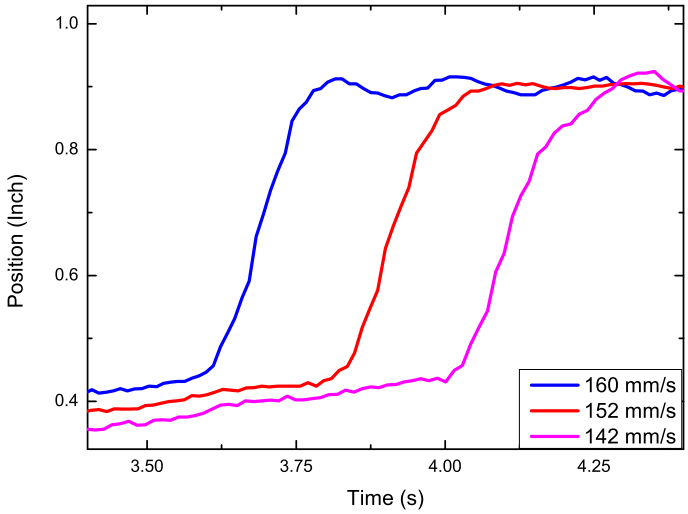

Figure 3-46. These motor motions are created by taking advantage of the motor resonances and actuating the grid for a specified amount of time to maximize the armature speed.

3.4.3.2 With a 0.01 Ω shunt resistor

The first shunt resistor used in the apparatus had a value of $10\ m\Omega$. This shunt is roughly 10 times smaller than the ideal value calculated for the motor theory. This reduced value of resistance increases the inductive time constant of the circuit (L/R) and does not allow for fast changes in the drive current. Figure 3-47 shows a slow motor ramp as a function of time for the highest anti-Helmholtz current used ($2.8A$) and Figure 3-48 shows the relationship of drive current to position for the different anti-Helmholtz currents. If this figure is compared to the similar one for no shunt resistance the difference is chosen. Because of the long time scales needed for the motor to come into equilibrium with the applied current, there is delay in the movement of the motor with a change in current. Due to the low shunt resistor, oscillations on the motor are strongly suppressed, in particular for the higher anti-Helmholtz currents. Fig 3-49 shows several different motor motions with nearly the same velocity but with different anti-Helmholtz currents. The fourier information from these different motions are presented in the inset of the figure.

To produce fast motions in this coil design, changes in current of nearly 1 A are required, where the reactance of the motor circuit and not allow. This can be seen in Figure 3-50 where stepwise changes in current produce inductively slowed motions.

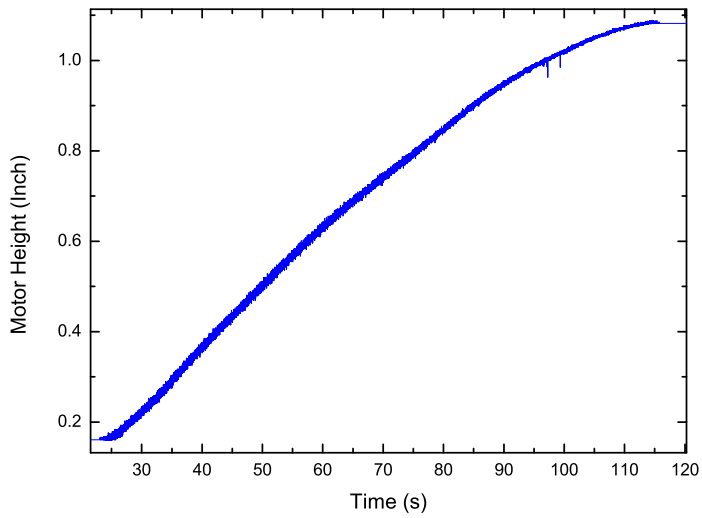

Figure 3-47. Slow motor ramp showing calibration data for the 10 $m\Omega$ shunt motor. The current recorded from this motion is used to produce the input files for this motor design.

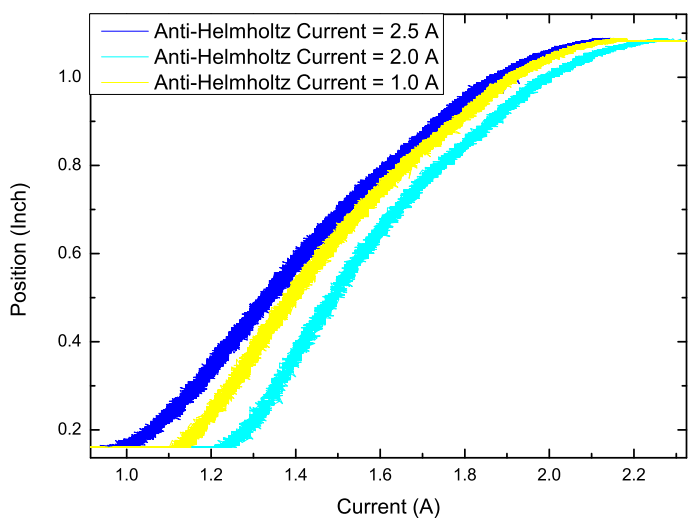

Figure 3-48. Current vs. position for the 10 $m\Omega$ shunt motor. This figure shows a curious effect where the calibration data from the different anti-Helmholtz currents do not differ by much. This is attributed to the long electrical relaxation time of the LR circuit.

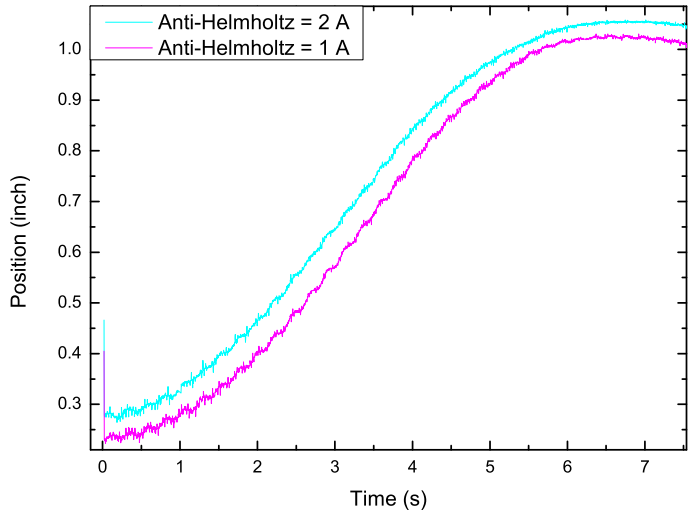

Figure 3-49. This figure shows two similar motion profiles for different anti-Helmholtz currents.

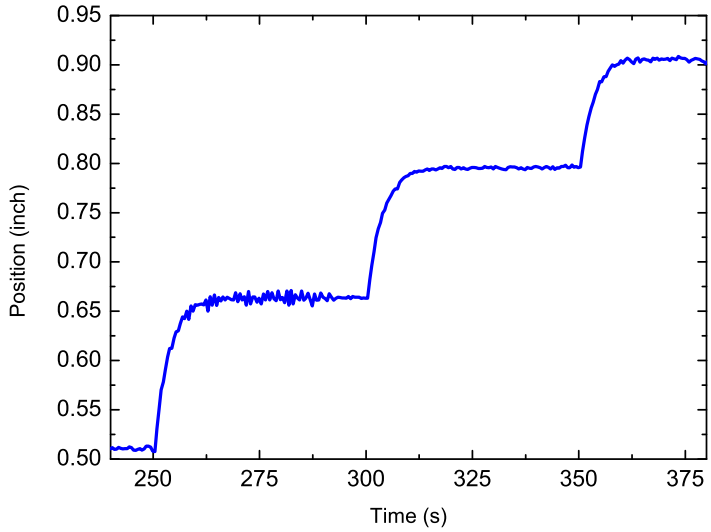

Figure 3-50. This figure shows the long equilibrium times for the motor after a current step with the 0.01 Ω shunt resistance.

3.4.3.3 Shunt resistor = 0.1 Ω and 1 Ω

In the motor theory calculations, a shunt resistance of about 0.1 Ω matched the natural harmonic of the system. As was seen before, a lower value of shunt resistance produces under damped motion. This is apparent by the faster reaction time of the motor circuit. The motor motions for both a 1 Ω and a 0.1 Ω shunt resistor are now shown below.

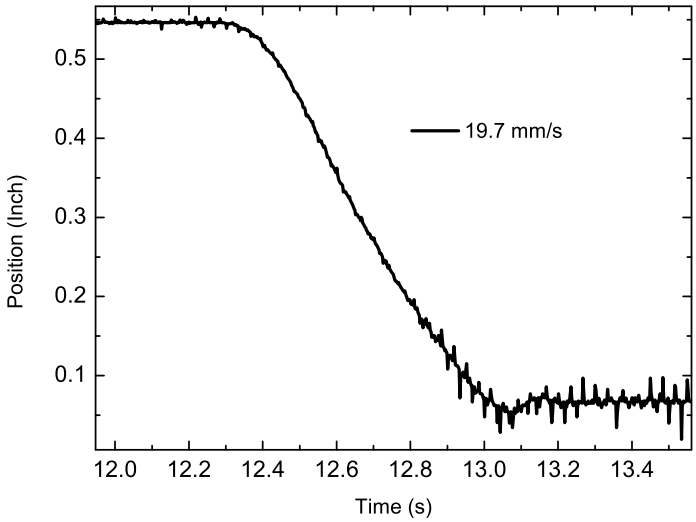

Figure 3-51. This figure shows a $19.7\ mm/s$ motion for the $0.1\ \Omega$ shunt resistance control motor

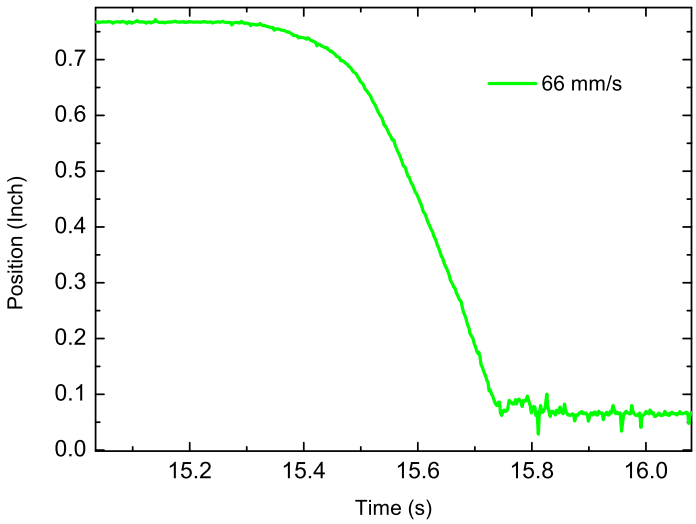

Figure 3-52. This figure shows a $66\ mm/s$ motion for the $0.1\ \Omega$ shunt resistance control motor

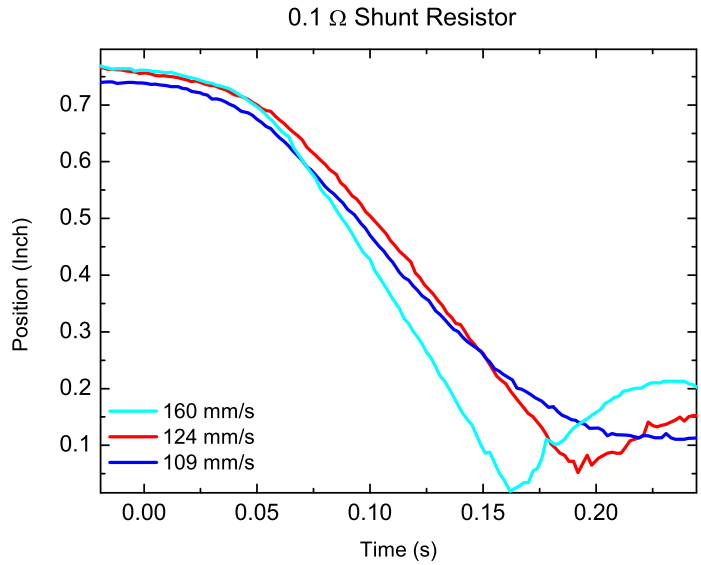

Figure 3-53. This figure shows a $109 - 160\ mm/s$ motion for the $0.1\ \Omega$ shunt resistance control motor

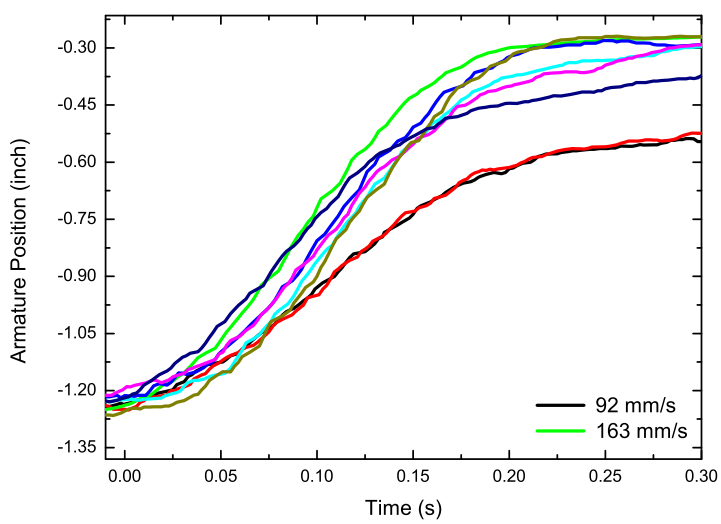

Figure 3-54. This figure shows a $92 - 163\ mm/s$ motion for the $1\ \Omega$ shunt resistance control motor

CHAPTER 4
MILLIKELVIN EXPERIMENTS

The first linear motor built for experiments at mK temperatures was constructed by S.C. Liu, G. Labbe and G.G. Ihas [74]. In Chapter 3 this motor construction was referred to as the impulse motor. This experimental apparatus and the resulting work are the first incarnations of isotropic homogeneous turbulence produced by moving a grid at mK temperatures. The details of the experiment and apparatus are thoroughly reviewed in [75] and the operation procedure of the motor is reviewed in the impulse motor section, Section 3.2. A schematic of the experimental cell is shown in Figure A-12 and the relevant parameters are in Table 4-1.

The apparatus has been cooled to millikelvin temperatures several times, each time with a slightly different operating procedure which is reviewed in Chapter 4. The initial experiments were conducted with a spring steel grid producing eddies in a helium bath and reported in [84]. Concerns about the magnitude and type of heating observed in this work led to a new grid design and material. A stainless steel mesh of identical design was constructed to replace the magnetic spring steel grid. Results from this are published in [85]. With this additional work, the results were still not well understood and the grid was removed from the system and the cell was run as a control to measure the heating from electronic and frictional dissipation from the actuation procedure alone. After the control measurements, the stainless steel mesh was re-installed and the

Table 4-1. Relevant properties of the impulse motor

Category	Result	
Solenoid Radius	5	mm
Length of Solenoid	10	mm
Nb can Radius	3.175	mm
Length of 1st Nb can	13	mm
Length of 2nd Nb can	15	mm
Gap between Nb cans	21	mm
Mass of armature	2.6	g

impulse motor cell was cooled again, to reproduce the previous measurements. These experiments and the comparisons between them are reported in Chapter 4.

This motor was designed to create a massive amount of turbulence in a very short time. Data from Stalp et al. [86], suggested that at 1.4 K grid velocities of upwards of 1 m/s were required to establish a long and well defined inertial regime. At the time, theory suggested that well developed quantum turbulence required fairly high grid velocities, with this in mind a mK experimental cell was created to meet these demands. The operation of this motor is explained in the motor design Chapter 3 in the section on the “Impulse Motor”.

The cell was machined from oxygen free copper and heat sunk to the mixing chamber of a dilution refrigerator, without a sintered heat exchanger. The motor was designed to have a weak thermal link to the mixing chamber, so that it can be both cooled by the mixing chamber and isolated enough to observe quick changes in the helium temperature. The motor was plated with superconducting lead to form an insulating layer, both magnetically and thermally, between the helium and the copper. The lead plated copper was mounted on a gold plated heat stage which was attached to the mixing chamber via 4 1/4" copper rods. This set up is the same as was used to calibrate the thermistors. No sinter was used because the experiment was designed to measure fast temperature changes from a large amount of turbulence rapidly decaying. Therefore, the thermometers are designed to measure the change in temperature before the cell equilibrates with the mixing chamber.

Due to the rapid nature of the proposed decay process, the Kapitza boundary resistance between the lead and helium and lead and copper was used to insulate the cell. The lead is a superconductor and therefore unable to hold much heat (due to the absence of electron modes), but the two layers of boundary resistance and poor thermal conductivity of lead insulate the helium on the time scale of our measurement.

The experimental procedure was to fill a cylinder with a pool of helium, stabilize the temperature, drag a towed grid through the pool, and measure the helium response with various sensors. The turbulence creating grid is positioned at the bottom of the cylinder, suspended just above the thermometers, heaters, and pressure sensors. During different phases of the experiment, different grids are used including grids made from stainless steel, spring steel, and G-10 mesh. The thermistors were mounted on a plastic circuit board just above, but not in direct thermal contact with, the bottom of the cell, while the other thermometers were suspended in the liquid by their electrical leads. The grid is towed upwards with a rapid acceleration, average 50 m/s^2, to speeds of $\sim$ 1 m/s then decelerated at the end of the motion by a similar rapid technique. The grid is pulled through the fluid, then pulled through the surface or left in the liquid, depending on experiment. Once the grid is out of the liquid, it can be held above the surface on plunged back through the liquid by gravity.

Throughout the experiment, the thermistor resistance is monitored with a wheatstone bridge circuit driven at 70 kHz and an integration time constant of 300 μs. The position of the grid is monitored by the capacitive position sensor in a separate bridge circuit driven at 90 kHz. The position of the motor, cell temperature and helium temperature are all controlled and/or monitored by a National Instruments Board and LabView software. The DAQ board has a maximum sampling rate of 50 μs.

The first measurements using this motor system were completed with the spring steel grid at a temperature around 500 mK. For the data presented here, the grid was pulled 4 mm through the liquid helium and held above the surface for 0.03 s before it was allowed to fall. After the initial rise and fall of the motor, the grid was allowed to relax and sit in the lowest position of the cell. An example of one particular motor motion is presented in Figure 4-1 [84]. In addition to the motor speed, the mesh Reynolds number for the motion is given using viscosities from two different sources [84, 86]. In the figure, the positive grid speeds correspond to motions opposing gravity and the negative

speeds are for motion aligned with gravity. The mesh Reynolds number is defined as,

$$Re_M = V_g M \rho / \nu, \tag{4–1}$$

where M is the mesh size, $\frac{\rho}{\nu} = \eta$ is the kinematic viscosity, and V_g is the grid velocity.

Measurements at 600 millikelvin were taken without the presence of liquid helium in the cell. These measurements are used as a control, showing the electrical coupling between our sensors and the drive, as well as the heating produced by the motion of the grid when only a helium film is present. Note the small rise in temperature seen in both the no bulk helium present and the helium present data. When there is no bulk helium in the cell, the second larger temperature rise is absent. Data taken from this grid pull are shown in Figure 4-2 [84]. These data show an immediate rise in temperature which quickly plateaus following the current drive to the motor and the corresponding motion of the armature. This set of data is compared to a similar motor motion at 520 millikelvin when a column of helium is present in the cell Figure 4-2. In this second experiment, after an initial time period where the measured data from both runs match, a second larger temperature rise is observed.

For comparison to fluid dynamic studies, the change in temperature shown in Figure 4-2 can be converted into internal thermal energy of the helium in the cell. Using the helium volume and the tables compiled by Donnelly and Barenghi [34], the helium temperature can be converted into an enthalpy. This is shown in Figure 4-3 along with the position of the grid as a function of time. Plotting both data sets on the same axis shows that the initial rise in temperature seen in both the empty cell and helium fulled cell coincides with the initial motion or initial application of potential to the drive coil. This signal is likely electrical and independent of the fluid motion. The second rise appears to be more interesting. It clearly occurs after the motion of the grid has ceased. Because the thermal conductivity of superfluid helium is extremely large, it is not likely that this heating was created in the helium at the time of the motor motion.

The expectations for heating after the decay of quantum turbulence can be calculated, both as a function of time and the magnitude of energy released. First we calculate the drag force on the grid assuming helium is a classical fluid and the drag coefficient is of order one,

$$F = CAV_g^2\rho/2. \tag{4–2}$$

A is the opaque area of the grid (1.78 cm^2), C is the coefficient which is taken to be one, and ρ is helium density at 0.52 K. Integrating this force through the traverse of the grid through the helium we can obtain an injected energy of about 30 μJ. Therefore, the maximum expected kinetic energy of the helium is only 1/5 of the energy we measure! Therefore, based on this rudimentary order of magnitude estimation, something unexpected is happening in the sample.

The unexpected magnitude of heat measured in this experiment, paired with a difficulty to reproduce consistent motor motions, forced us to rethink the cell design and search for alternative, other then turbulent, sources of heating in the experiment as well as reasons for an irreducible motor motion. The cell was warmed up and the original magnetic spring steel grid was replaced with a non-magnetic stainless grid in an attempt to mitigate the small magnetic coupling between the grid and the drive magnet. In an effort to not change more than one parameter, the experimental cell was re-cooled with only this design alteration.

Data from motor motions with the stainless steel grid are shown in Figure 4-4 [85]. These data were taken after similar motor motions as shown in Figure 4-3. The motor motion is also shown on these plots in red. These data are taken over an expanded time-scale to show the extent of the heating measured by our thermometry. The top two plots of Figure 4-4 show a short time response, still more than 10 times as long as the previous figure, where the initial temperature rise is seen. The short time scale data cover a range of time significantly longer than the figures presented in Figure 4-3, so the short electronic heating signal is not detailed. Again, the motor motion is provided

to give a reference time scale. This temperature change is similar to, but smaller than, the data presented for the spring steel grid. However, if the signal is tracked for longer periods of time a second, even larger heat signal is measured. Since the original data was only recorded over a short time scale, it is unknown whether this signal was present in our first series of experiments. Once again these heating signals are too large to be due entirely to turbulent energy decay.

With the inability to identify the source of heating in our previous experiments, the turbulence creating grid was removed and the motor system was run with just the armature. Figure 4-5 shows the evolution of the measured heat vs. time for a motor run without the grid. In this plot, there are also data measured from a square voltage pulse into a carbon heater. The two figures are very similar is shape, showing a sharp initial spike in temperature followed by the absorption of that heat by the cell walls and mixing chamber. The only difference between the two figures is that the heating from the motor motion appears to have a better heat link to the thermal bath.

The heating pattern without the grid present can be compared to the measured change in energy for the previous runs when the motor was run with a stainless steel mesh. These data are presented in Figure 4-6. These data show a clear distinction between the behavior of our system from the data taken with the eddy creating grid present and the data collected when the grid was removed. In this figure, the shape of the measured temperature change is completely different between the two runs, as is the absolute magnitude of the heating produced.

The final measurements conducted using this apparatus were with the stainless grid reattached, checking the substantial difference measured previously between the heating measured with a grid and without the grid. Data from these motor runs are presented in Figure 4-7. Each different color on this plot represents a different current profile sent to the drive motor. Predictably, the larger the input current and the faster the motor motion, the larger the heating measured. Since our previous work suggested that

the entire heating signal was not due to the turbulent energy decay, but a combination of electrical heating, frictional dissipation and turbulent energy decay, the differences between the energy released from each motor run was compared to the changes in the motion profile.

Figure 4-8 shows data from two similar motor motions. The main plot in the figure shows the energy difference between the measured thermal response of both runs, and the inset shows the armature position as a function of time for each motor motion. Figure 4-9 shows the same type of data but from two very different motions: one in which the grid moves through the fluid and the other in which the grid does not move at all. For both figures 4-8 and 4-9, the difference in applied current to the motor is the same, but in one there is a large difference in the armature motion while in the other, there is not. The change in energy for both plots are very similar to one another. This implies the heating measured is not due to the motor motion, but some other source. Both of the energy differences are plotted next to one another in Figure 4-10 demonstrating this effect. From these data, it appears that the energy produced by the motor is independent of the grid motion, and depends more directly to the current level applied to the motor drive coil.

Because of the independence of the heating on the measured motion of the grid and the enormous size of the heating measured in the experimental cell, it is shown that the majority of the signal observed was not due to turbulent energy decay. In addition, the heating in the cell appears to be directly dependent on the current supplied to the drive coil. This implies that there is either a resistance along the motor current leads in the cell where power is dissipated or a magnetic coupling to another conductive part of the cell which produces eddy currents.

The first attempt at reducing the large heating signal was to replace the brass electronic pins connecting the superconducting motor leads to the copper heat exchanger outside the cell, reducing ohmic heating from the large currents traveling

though the pins. Once it was shown that this did not have a noticeable effect on the heat signal measured, attempts were made to reduce the eddy currents produced by the drive motor. In the original motor construction, discussed in the literature [74] and used here, this was done by coating the copper cell with superconducting lead to reduce the eddy currents in the copper cell itself. This also did not seem to be the source of the heating.

Currents in the metal gird were also considered and a plastic grid was constructed to replace the steel one. This grid is shown in Figure 4-11. The values of the eddy currents in the spring and stainless steel grids are calculated by the standard formula [87] using the formula,

$$\dot{Q}_e = PV\dot{B}^2/\rho, \tag{4–3}$$

and P is the geometric factor defined below, V is the body volume, $\dot{B}^2$ is the functional change in magnetic field, and ρ is the electrical resistance.

$$P = \frac{d^2}{16}\frac{(w/d)^2}{(1+w/d)^2},$$

where w and d are the width and length of the mesh on the grid. Since the magnetic field outside a solenoid decays rapidly, the eddy currents on the grid are not large enough to produce the heating observed.

After the final experimental run (data shown in Figure 4-7), it became apparent that the problem with this motor design did not stem from any of the sources listed above, so an entire new experimental system was created which removed all of the non-superconducting metal from the experimental volume. This experiment is outlined in Chapter 5. When the troublesome motor was disassembled it was observed that the capacitive position sensor was extended with the use of conductive silver paint. This paint not only formed a large conductive loop in the drive motor, it also covered up parts of the superconducting cylinders. The paint was likely added to increase the sensitivity range of the position sensor, but it had the effect of providing a large conduction path

for eddy currents. These currents can be estimated by a similar set of equations to Equation 4–4, but modified for the case of a thin film [88]

$$\dot{Q}_e = \frac{\pi^2 \dot{B}^2 t V}{6\rho}, \tag{4–4}$$

where t is the film thickness. Depending on the resistivity used for the silver paint niobium circuit combination, this heating source can range from μW to mW. This is more than enough energy to account for both the heating observed in the experiments and the irreproducibility of the motor motions.

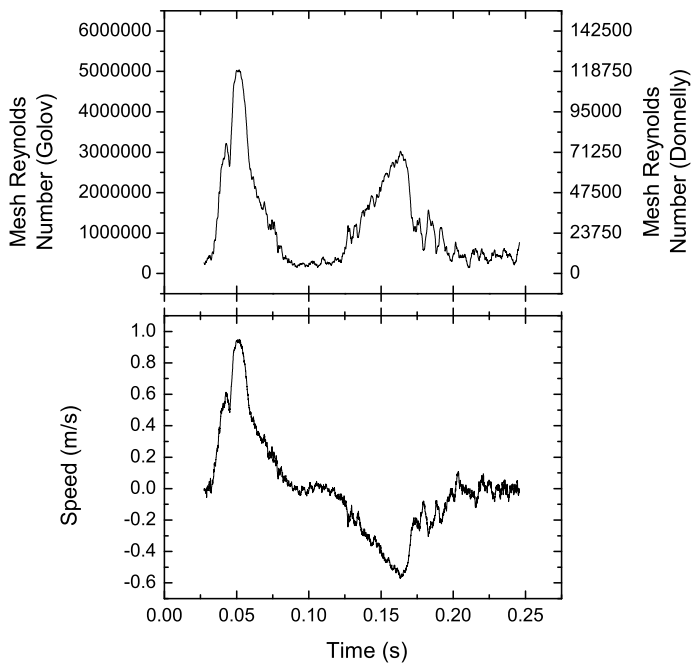

Figure 4-1. This figure shows the grid speed from the inertial motor at millikelvin temperature and the associated mesh Reynolds number [84]. There is some question as to what the effective viscosity of the helium is at this temperature so both possible scales are given [7, 34]

.

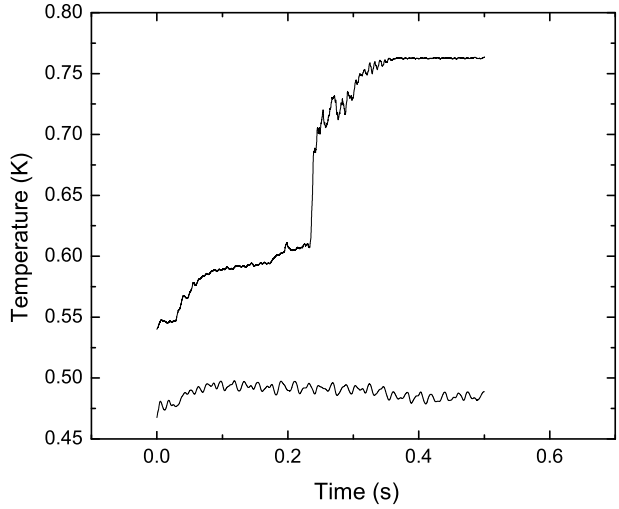

Figure 4-2. The temperature rise measured by the thermistor after the grid is pulled for the cases where the cell contains helium and when it does not [85]. The larger rise is only present when there is liquid helium in the cell while the early time small rise is present whether there is bulk liquid helium in the cell and just a helium film.

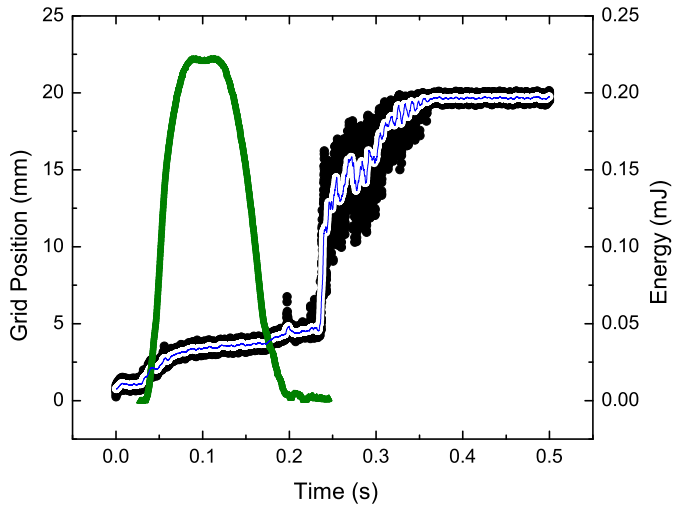

Figure 4-3. This graph shows the temporal relationship between the motor motion and the measured temperature increase in the cell. The first rise in energy directly corresponds to the initialization of current in the drive, while the second rise occurs some time after the motion has stopped [84].

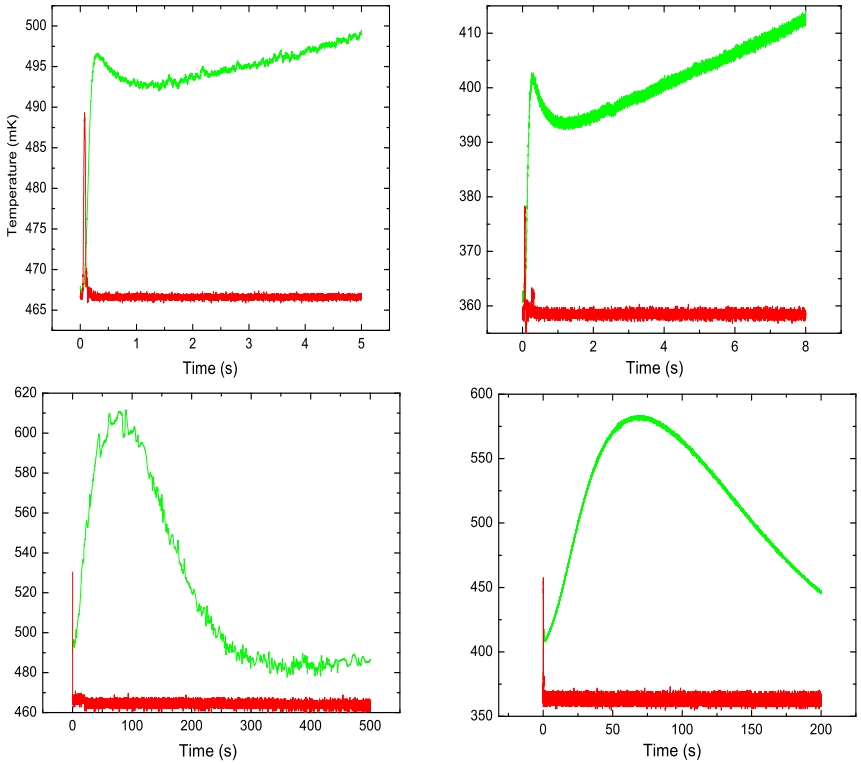

Figure 4-4. This plot shows four different instances of motor actuation in the helium and the similar heat profiles following the motion. The data are arranged such that the short time scales are in the top row and the longer times scales are on the bottom row. In addition to the difference in time scales the lower temperature data are on the left and the higher temperature data are on the right.

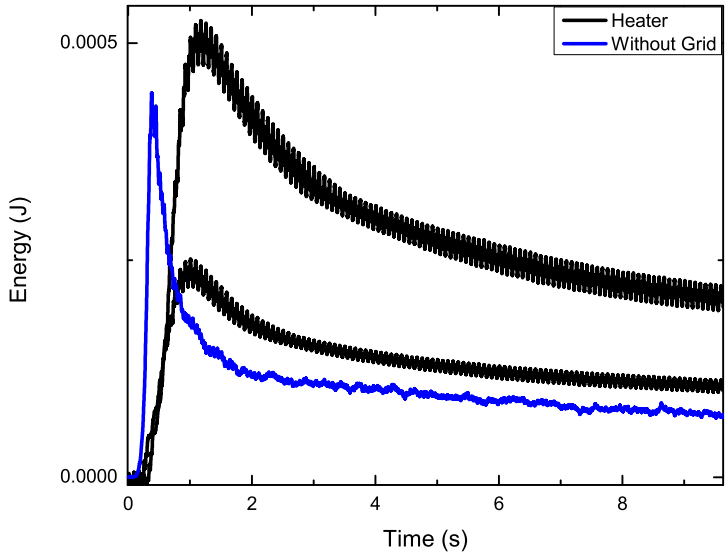

Figure 4-5. Plot showing the difference in heat generated from a carbon heater emersed in helium and due to motion of the armature sans gird. The heat from the heater was calibrated to deliver a similar amount of energy as was seen by the motion in the cell without the turbulence creating grid.

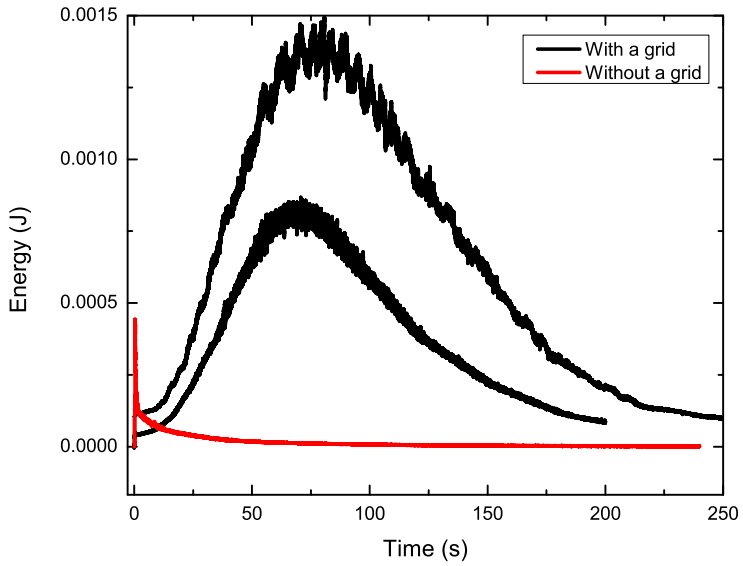

Figure 4-6. This figure shows the difference in the measured heat signals when the grid is attached to the armature and when it is not.

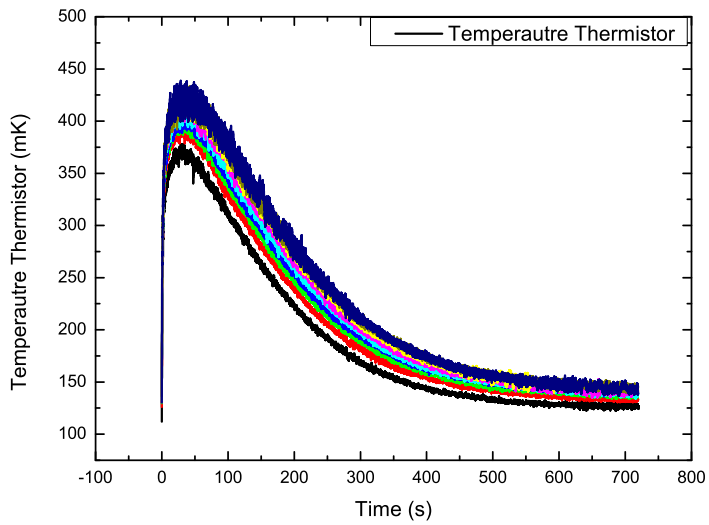

Figure 4-7. These heat traces are measured after different grid pulls. For each trace moving from the top to the bottom, lessen current is driven through the drive coil of the motor. In the bottom few traces on this plot the motor did not move at all.

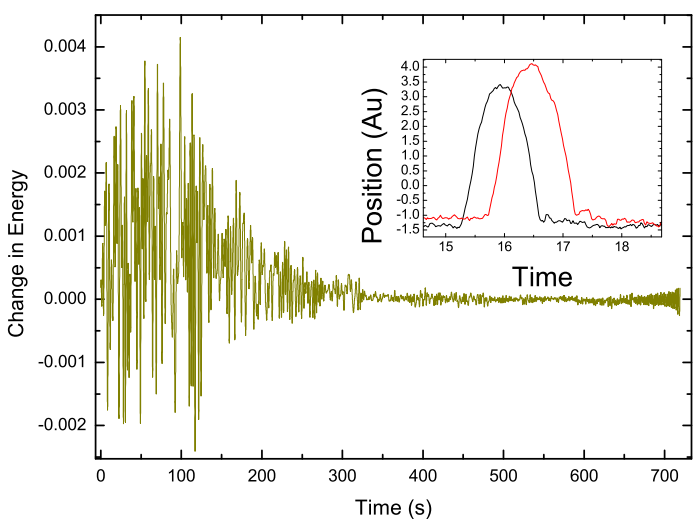

Figure 4-8. This figure shows the difference in measured energy between two traces with similar motion profiles. The motion of the grid is shown in the inset of the figure and the difference in the measured heat is shown in the main figure

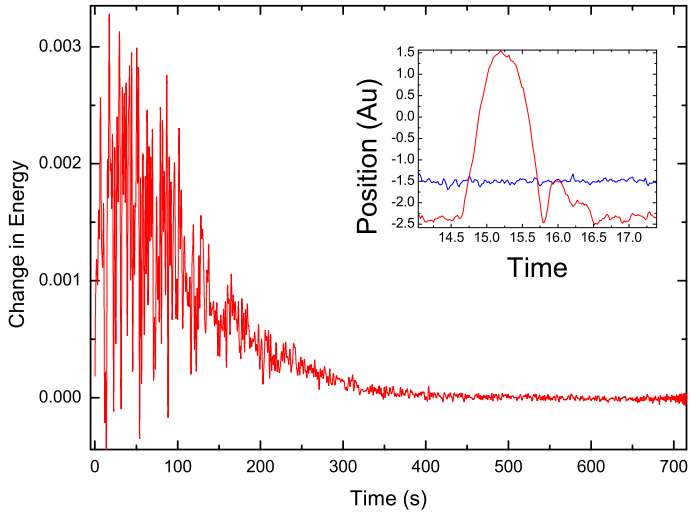

Figure 4-9. This figure shows the difference in measured energy between two traces with different motion profiles. The motion of the grid is shown in the inset of the figure and the difference in the measured heat is shown in the main figure.

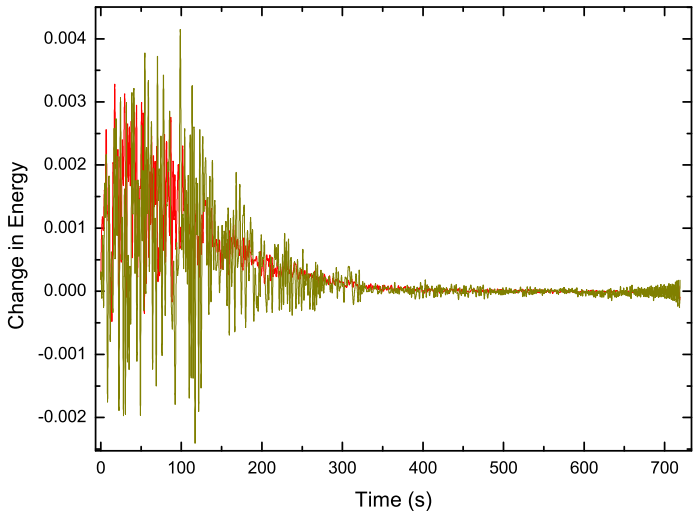

Figure 4-10. This figure shows the previous two energy differences (4-8 and 4-9) plotted on the same axis. This proves that the bulk of energy we are seeing from our motor system is not due to real motion of the grid, and therefore not due to turbulent energy decay.

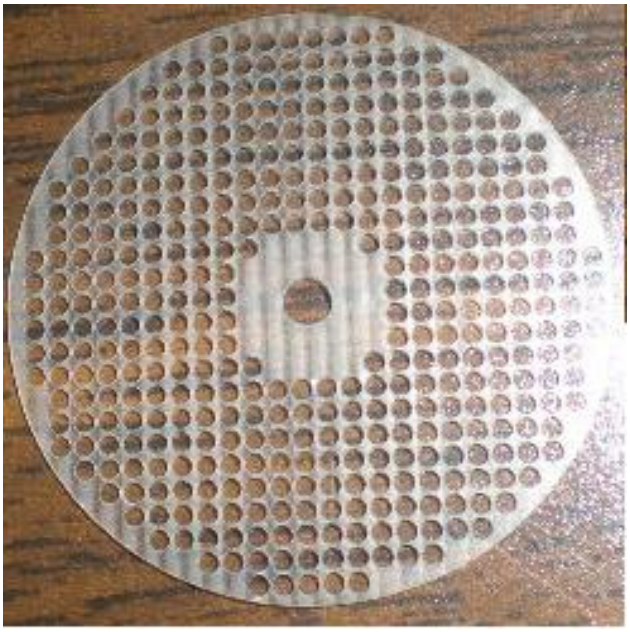

Figure 4-11. This figure shows a turbulence creating grid machined from G-10

CHAPTER 5
ONGOING AND FUTURE WORK

Presented in this dissertation are: an experimental implementation of an existing linear motor to create the first studies of quantum turbulence created by this means in the low temperature limit; identification of the possible shortfalls of this preliminary motor system and the development of a new, more sophisticated, drive apparatus; and the creation, exploration, and development of new and existing of sensors for measuring the properties of quantum turbulence. But alas, no work is ever complete. There is always more to do, learn, and explore. A few of the on-going projects and directions in laboratory will be over viewed and outlined in this Chapter. Specifically, the repair and modifications to the impulse motor assembly for another millikelvin experiment, the implementation of the control motor for the first runs to obtain new information about quantum turbulent energy decay, as well as some closing thoughts.

5.1 Second Sound and the Control motor

A second sound cell has been built and cooled to 1K. The machine drawings for the experiment are shown in Figure A-10. This experiment is mounted on the same insert shown in Figure 3-9 and placed above the top quadruple bearing. Three different turbulence-creating grids have been manufactured and images of them are shown in Figure 5-1. Two of the grids are of the typical design where an array of squares have been cut out of stainless steal stock to form a square mesh. The material has a thickness of $\sim 0.001\ in$ and the grids are $0.8\ in$ squares. These grids were created to have well defined length scales to characterize the turbulence. The third grid is of a very different, modeled after the only other cryogenic helium experiment where a linearly actuated grid is used [72].

This is the first grid to be cooled in this apparatus. It will be used in an attempt to recreate the data previously measured [72]. The control motor actuation distance is many times shorter that the motor used in Oregon, but still more than 10 times the

mesh spacing of grids that will be used. There is reason to believe that the control motor channel is long enough to create homogenous turbulence for this mesh size. Once this is established, the control motor will be used to investigate many new phenomenon in quantum turbulence. Of specific interest is the applicability of classical fluid dynamic like descriptions of grid turbulence for various different grid sizes and designs. Also, the early time formation of turbulence in the control motor channel, specifically if the momentum structure of the tangle obeys a Saffman or Bachelor expansion for low wave numbers will be investigated.

The control motor, grids, and channel used have a versatile design. They may be mounted both on the apparatus used in much of this work, as well as an optical apparatus where helium excimer molecules can track the normal fluid motion [58] and potentially track quantum vortex lines in the superfluid state!

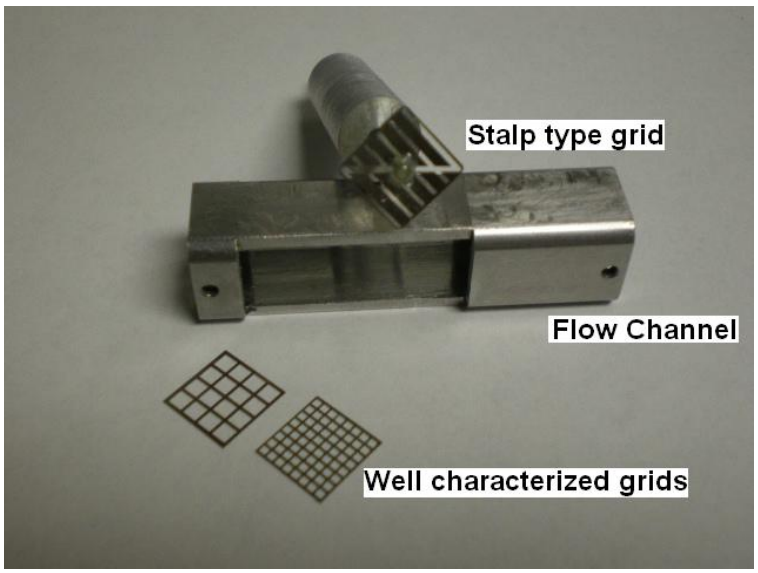

Figure 5-1. This figure shows three different grid geometries built to explore their effect on the creation and decay of turbulence at around 1K. The grids will be pulled through the channel in the figure and the second sound transducers mount on the slits shown in the channel.

5.2 Nonconducting impulse motor cell

A new nonconducting impulse motor cell has been created with similar dimensions to the one used in Chapter 4. The machine drawings and specifications of the cell are presented in Figure A-12. The capacitive position sensor was cleaned and the silver paint was replaced by a longer niobium cylinder. The stainless steal grid was replaced by a grid machined from polycarbonate as shown in Figure 4-11. This experimental cell was machined from Garolite XX, which is a paper epoxy mixture. The cell was machined to the dimensions specified and coated with a thin layer of Stycast 1266 epoxy to assure a superfluid helium leak tight system. Once at millikelvin temperatures, the operation of this motor system will proceed in a manner similar to that described in Chapter 4 and sec. 1.6.

The main difference of this experimental cell from the copper cell previously used is the heat exchange with the mixing chamber. The old cell relied on the poor thermal conductivity of superconductors and Kapitza boundary resistance where the new plastic cell is mounted on a thermal heat switch. With this improvement the calorimetry cell can be made much more independent of the mixing chamber, and the ancillary heat capacities from the copper mounts are no longer available as a heat sink.

The heat exchanger is a low mass modification of the standard helium heat switch used by the Ihas group. Photographs of the heat switch are shown in Figure 5-2. The switch operates on the principle that in different states, superconducting or normal, a indium wire will either conduct heat (closed) or not (open). The end of the thermal switch is soldered to a set of two silver sintered heat exchangers with exceptionally large surface area such as those commonly used at the University of Florida [89]. Silver sinter is a well established means for heat contact to helium at low temperatures [90]. The sintered silver is a pressed pellet of many 70 nm radius silver granules around a fine silver wire. By calculating the number of granules from the assumed grain volume and the measured mass of the popsicle, the surface area of the sensor can be inferred by

multiplying the number of grains by their individual surface area. After accounting for surfaces that touch with a factor of $1/2$ the surface area of the heat exchanger is shown to be $\sim 0.5\ m^2$.

The thermal conductivity of the switch can be calculated with this table for both the 'open' and 'closed' position of the indium wire. The thermal conductivity of the sliver wire connecting the switch to the popsicles and the thermal conductivity of the popsicles with the helium are also calculated below.

The Kapitza conductivity of the popsicle can be calculated at 100 millikelvin [66],

$$\frac{\dot{Q}}{\Delta T} = \frac{1}{R_k} \simeq \frac{5,000\ cm^2}{15080\ (Kcm^2/W)} = 0.33\ W/K. \tag{5–1}$$

The thermal conductivity of the 1" long of silver wire connecting the heat exchanger to the popsicles is [87]

$$\frac{\dot{Q}}{\Delta T} = \kappa_{silver} * \frac{L}{A} = 1 * 10^{-2}\ W/cmK \frac{1\ inch}{0.01^2 * \pi\ inch^2} = 2 * 10^{-6} W/K \tag{5–2}$$

and the thermal conductivity of the indium in its superconducting state [91]

$$\frac{\dot{Q}}{\Delta T} = \kappa_{In\ super} * \frac{L}{A} = 1.58 * 10^{-3}\ W/cmK \frac{6\ inch}{0.03^2 * \pi\ inch^2} = 6.2 * 10^{-9} W/K \tag{5–3}$$

and the normal state

$$\frac{\dot{Q}}{\Delta T} = \kappa_{In\ normal} * \frac{L}{A} = 1.020\ W/cmK \frac{6\ inch}{0.03^2 * \pi\ inch^2} = 4.0 * 10^{-5} W/K. \tag{5–4}$$

The other property of note for this heat exchanger is its low thermal heat capacity. Using the standard heat capacity for a metal at low temperature $c/T = \alpha T^2 + \gamma$ and a silver mass of $0.6\ g$ the thermal mass of the silver is [92]

$$C_{100\ mK} = 0.17414 * 0.1^3 + 0.61717 * 0.1 * 5.56 * 10^{-3} = 3.744 * 10^{-4}\ mJ/K \tag{5–5}$$

compared to the $1.2376 * 10^{-1}\ mJ/K$ for $1.5\ mol$ of helium [34].

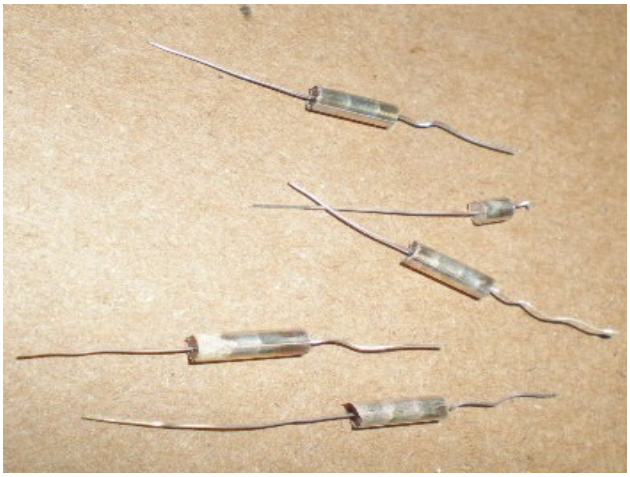

Figure 5-2. Photograph of 0.5 m^2 surface area sinter popsicles

APPENDIX
MACHINE DRAWINGS

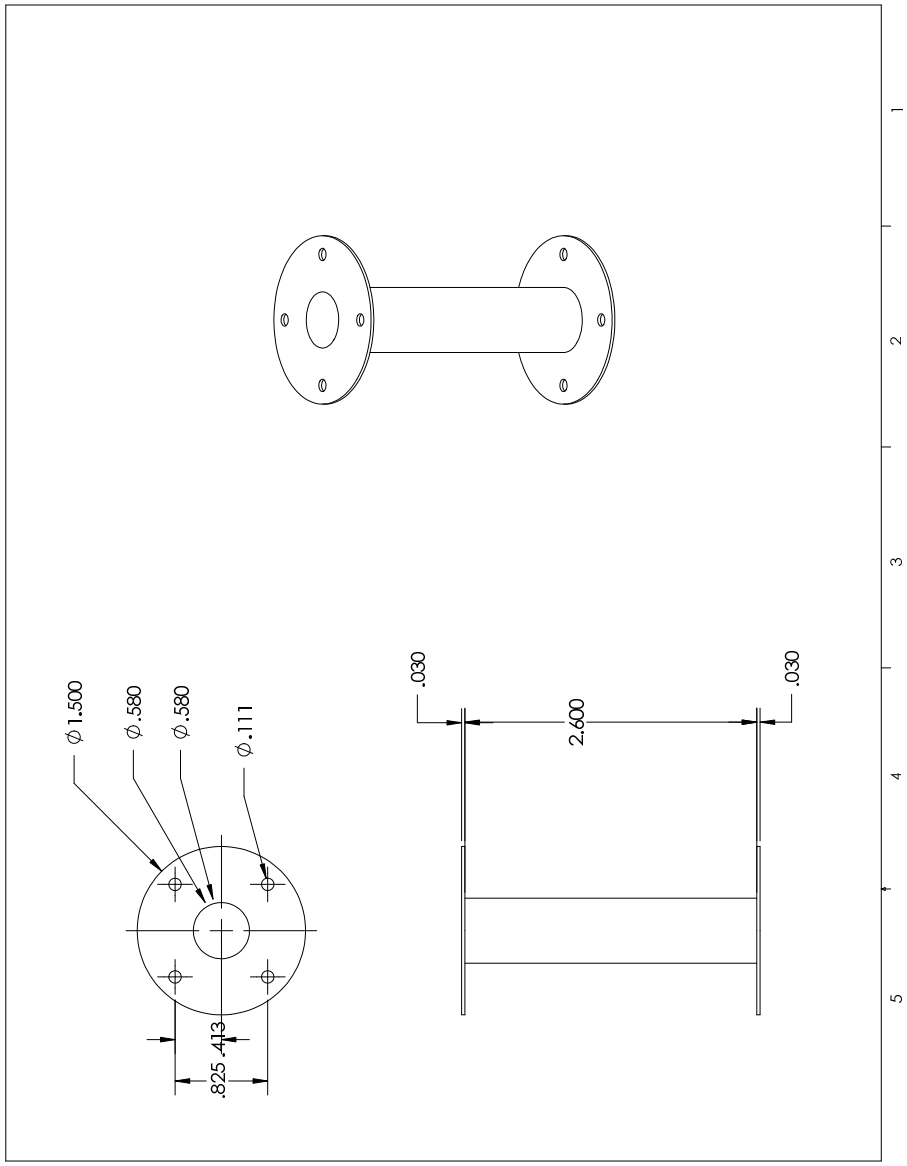

Figure A-1. Machine Drawing of drive solenoid

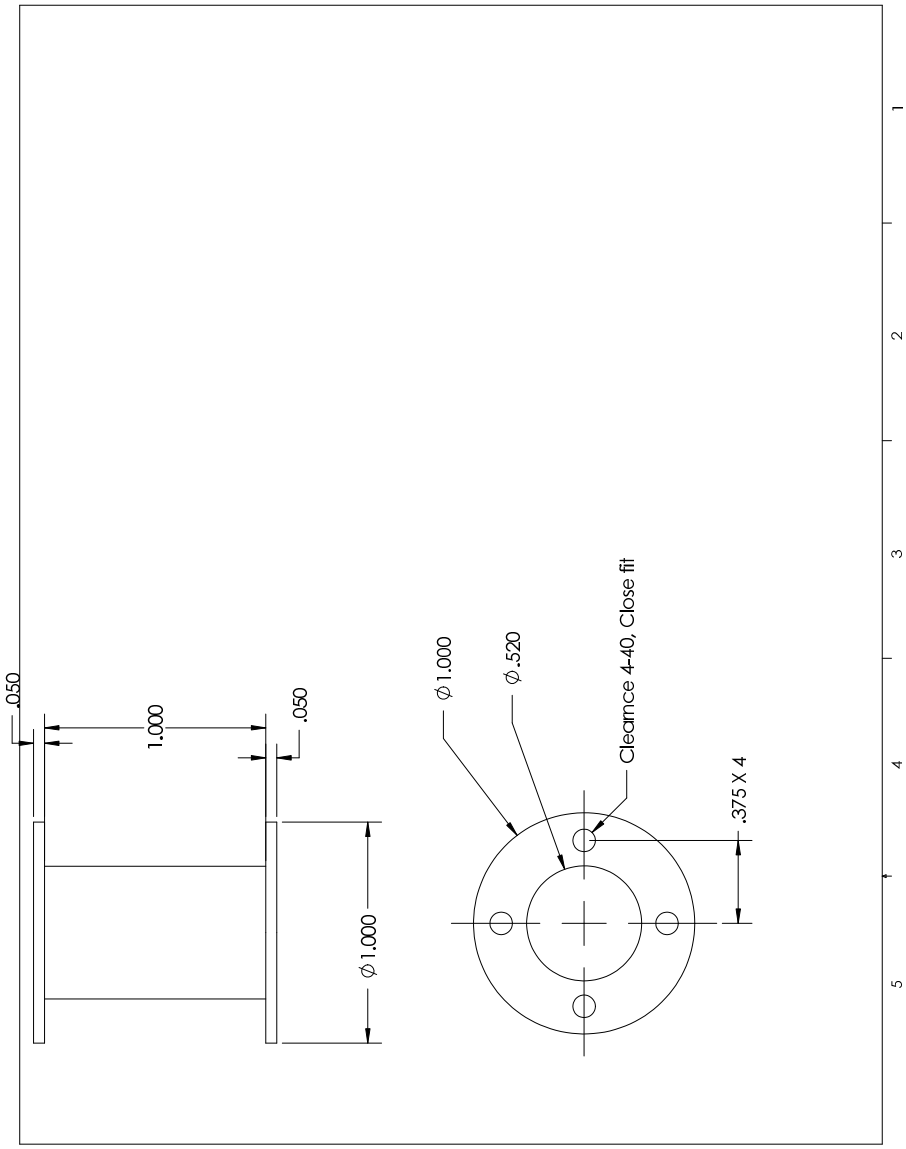

Figure A-2. Machine Drawing of inductive position sensor

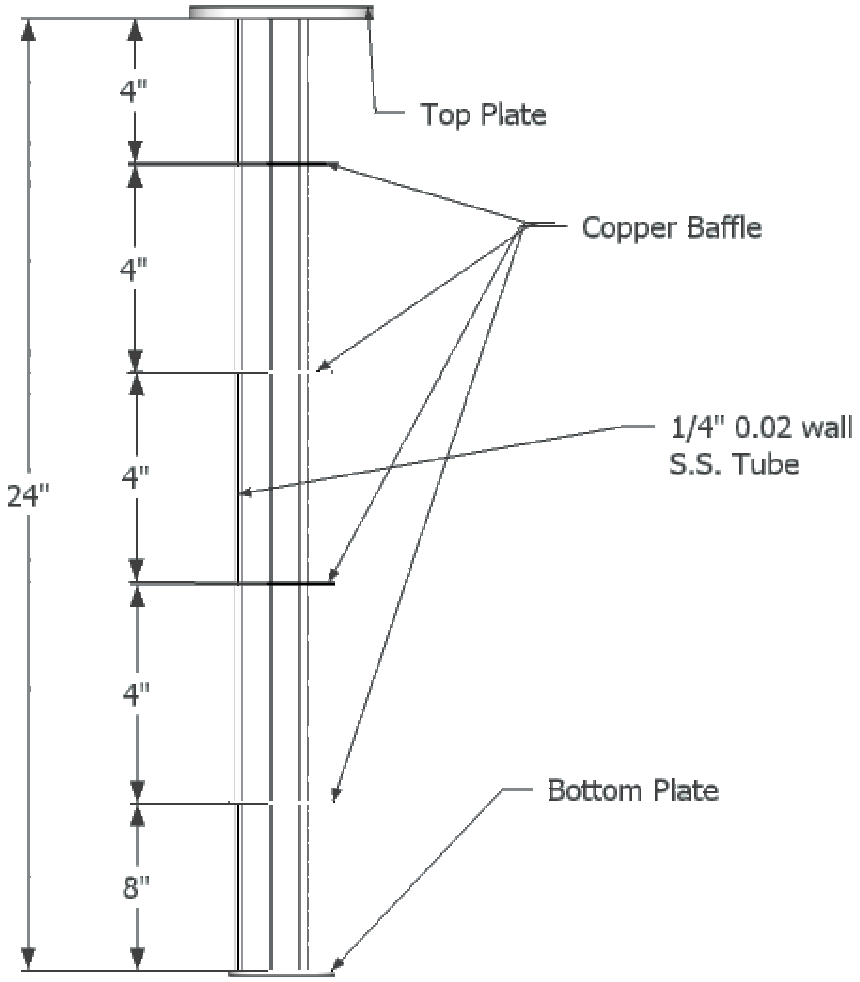

Figure A-3. Schematic drawings for the glass dewar insert

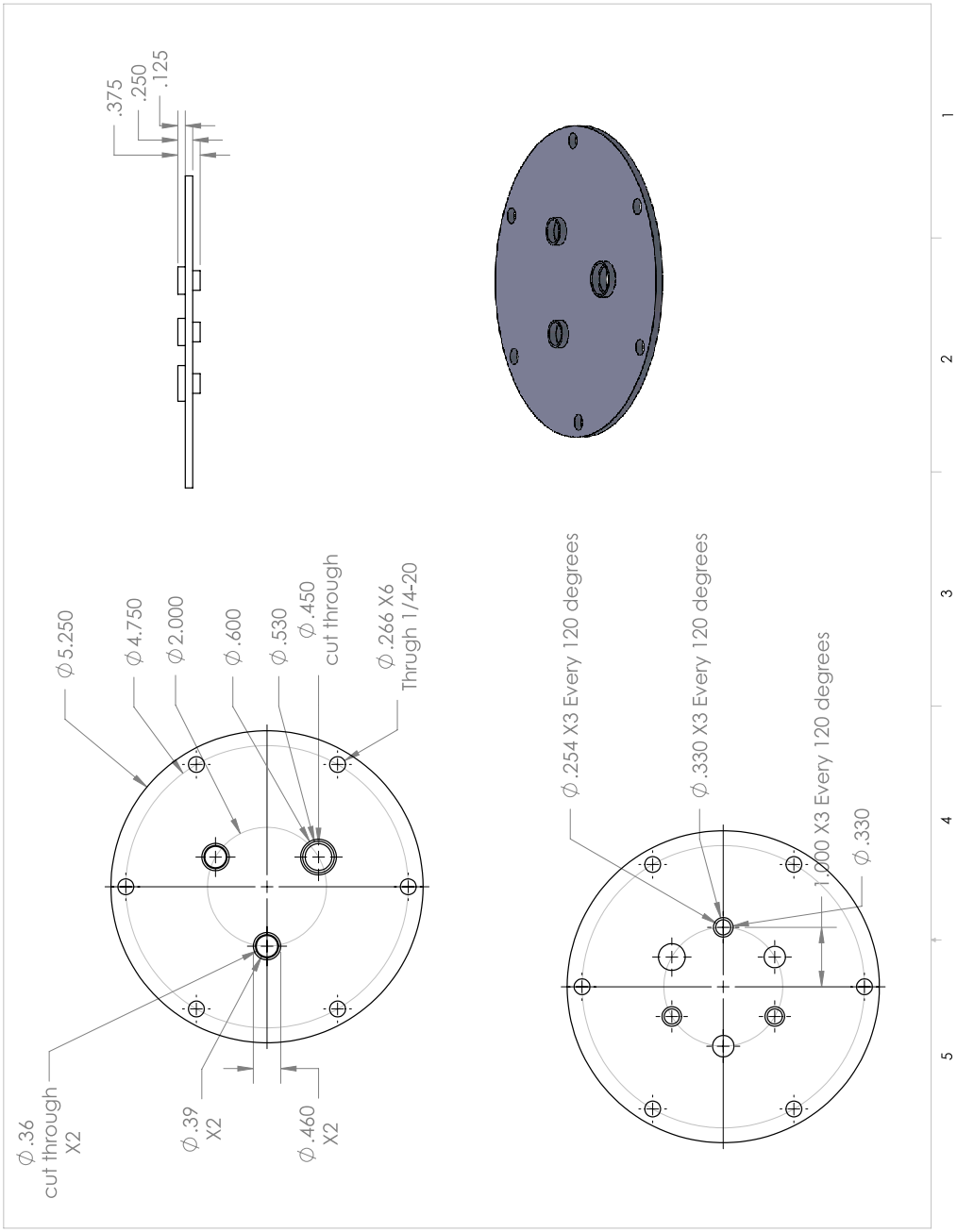

Figure A-4. Machine Drawing of top plate from glass dewar insert

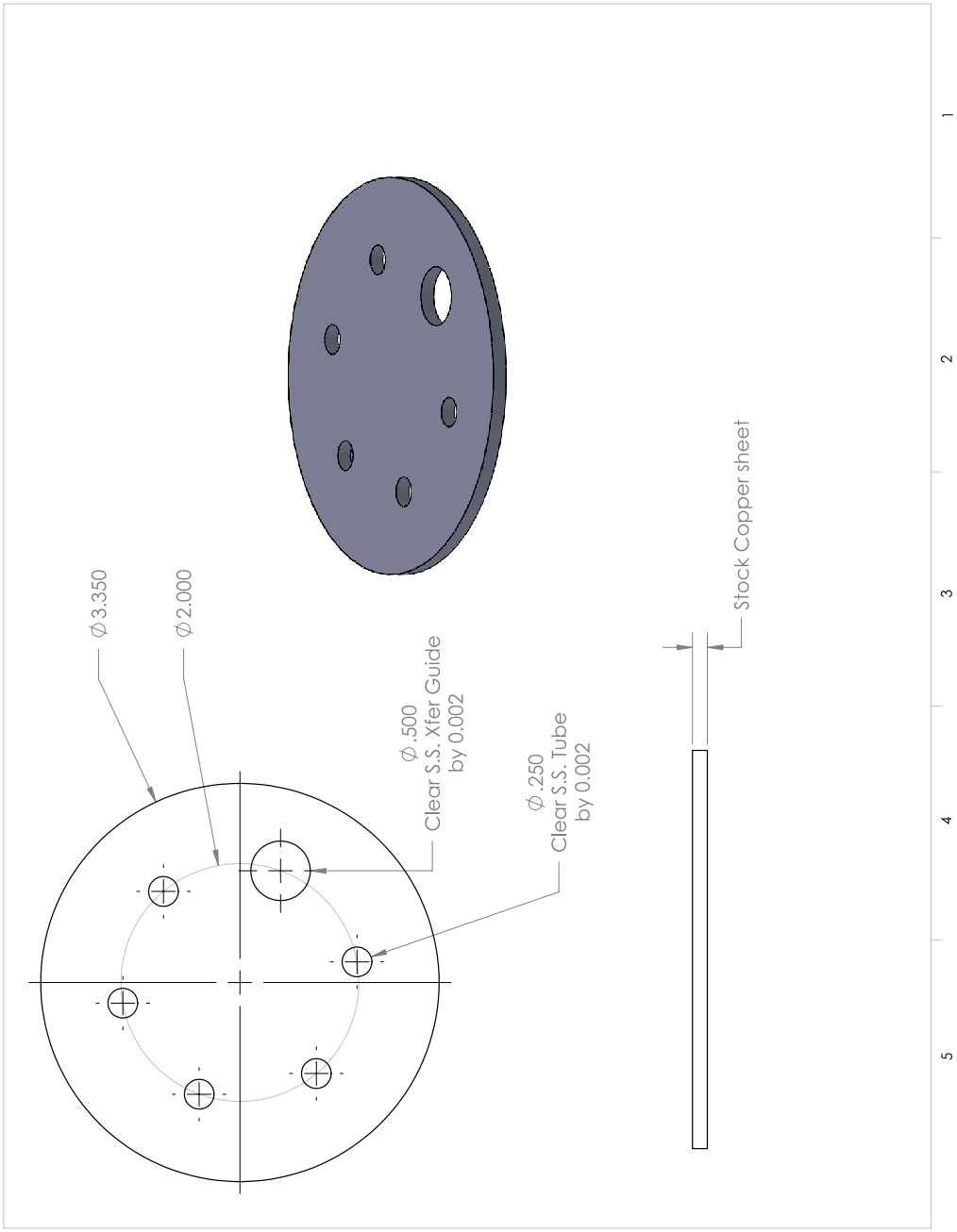

Figure A-5. Machine Drawing of baffle from glass dewar insert

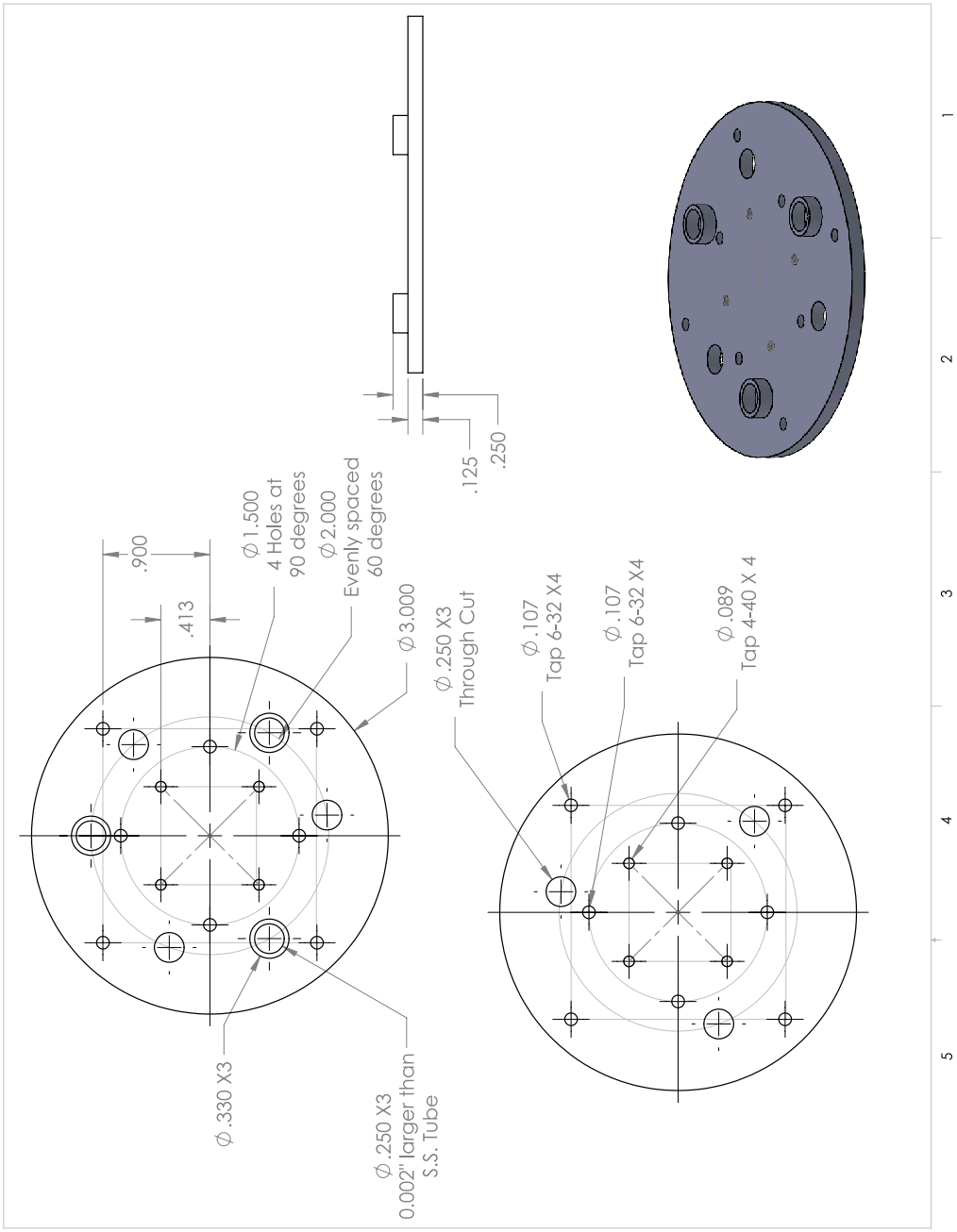

Figure A-6. Machine Drawing of bottom plate from glass dewar insert

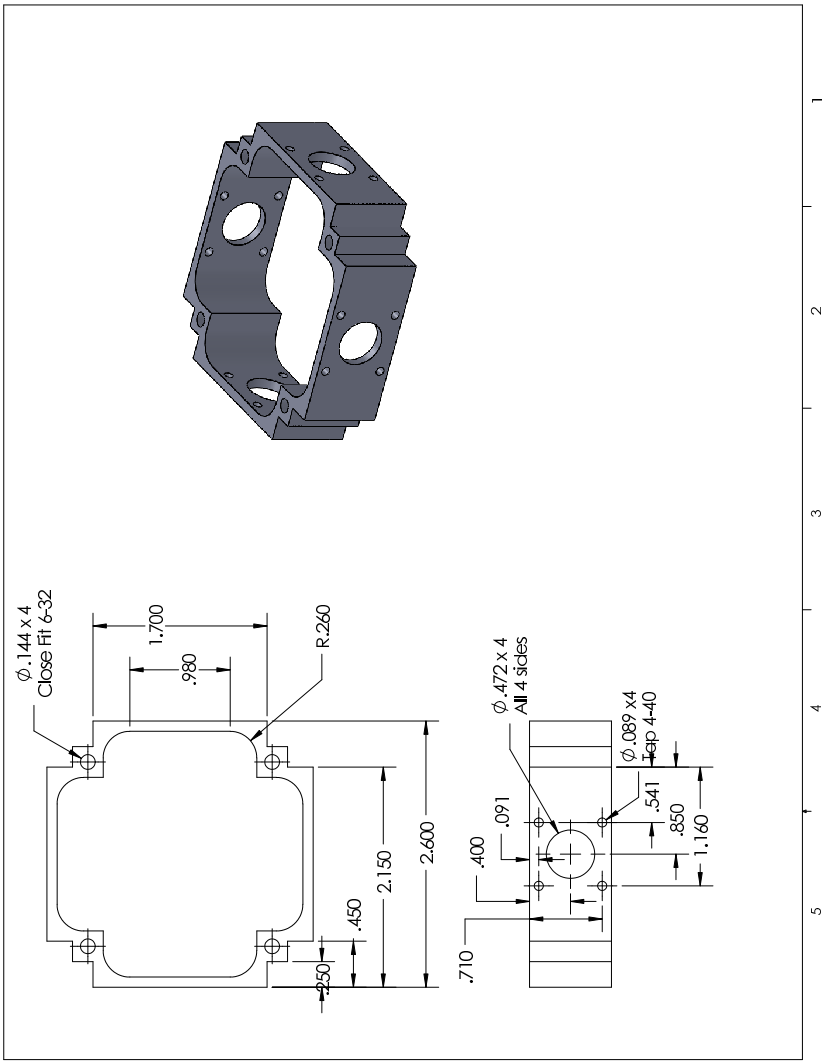

Figure A-7. Machine Drawing of quadruple magnet mounts

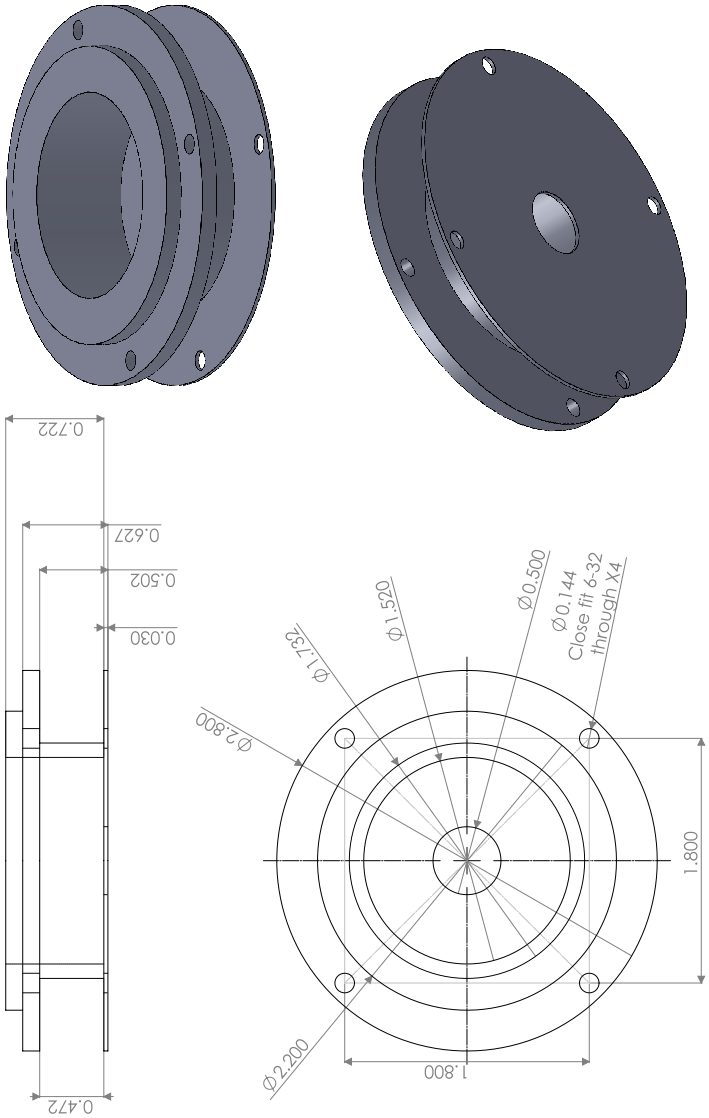

Figure A-8. Machine Drawing of top half of the anti-Helmholtz mandrel

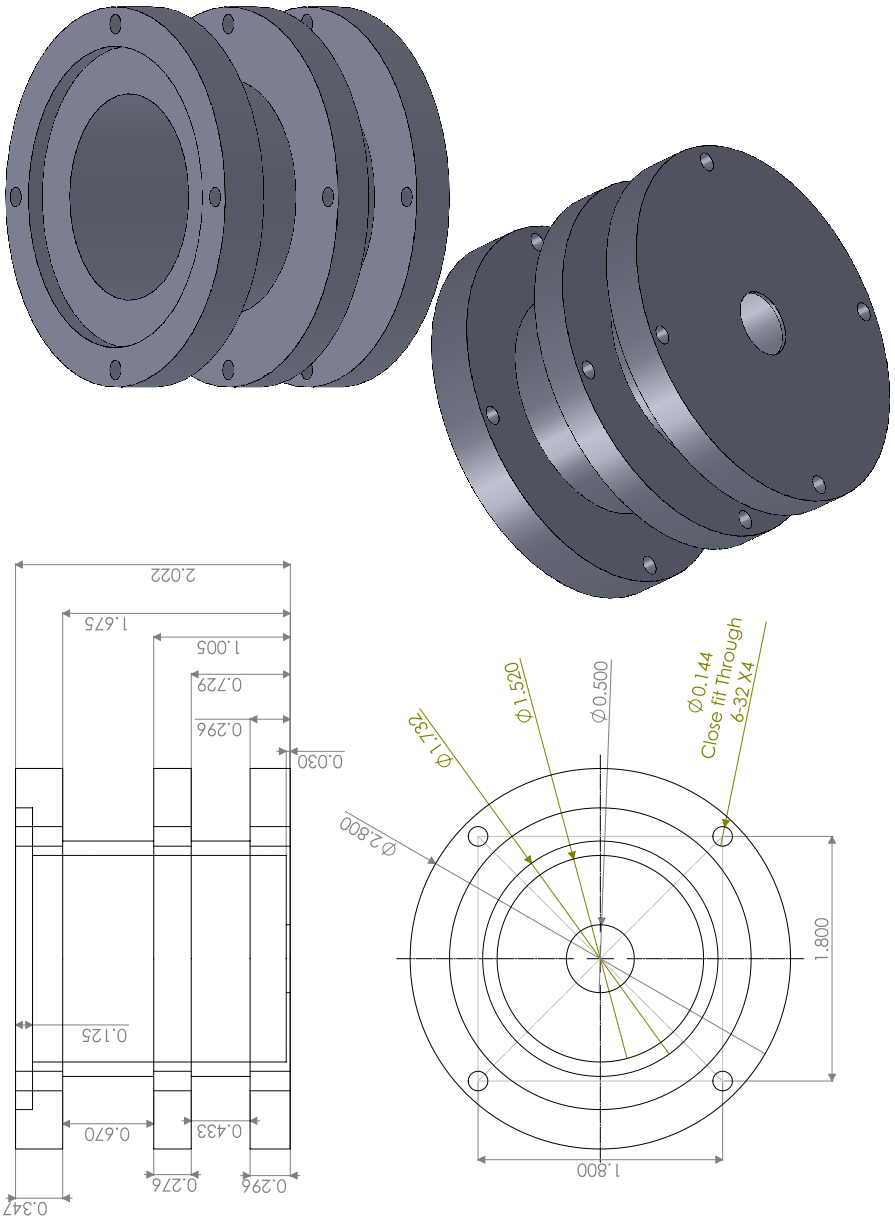

Figure A-9. Machine Drawing of bottom half of the anti-Helmholtz mandrel

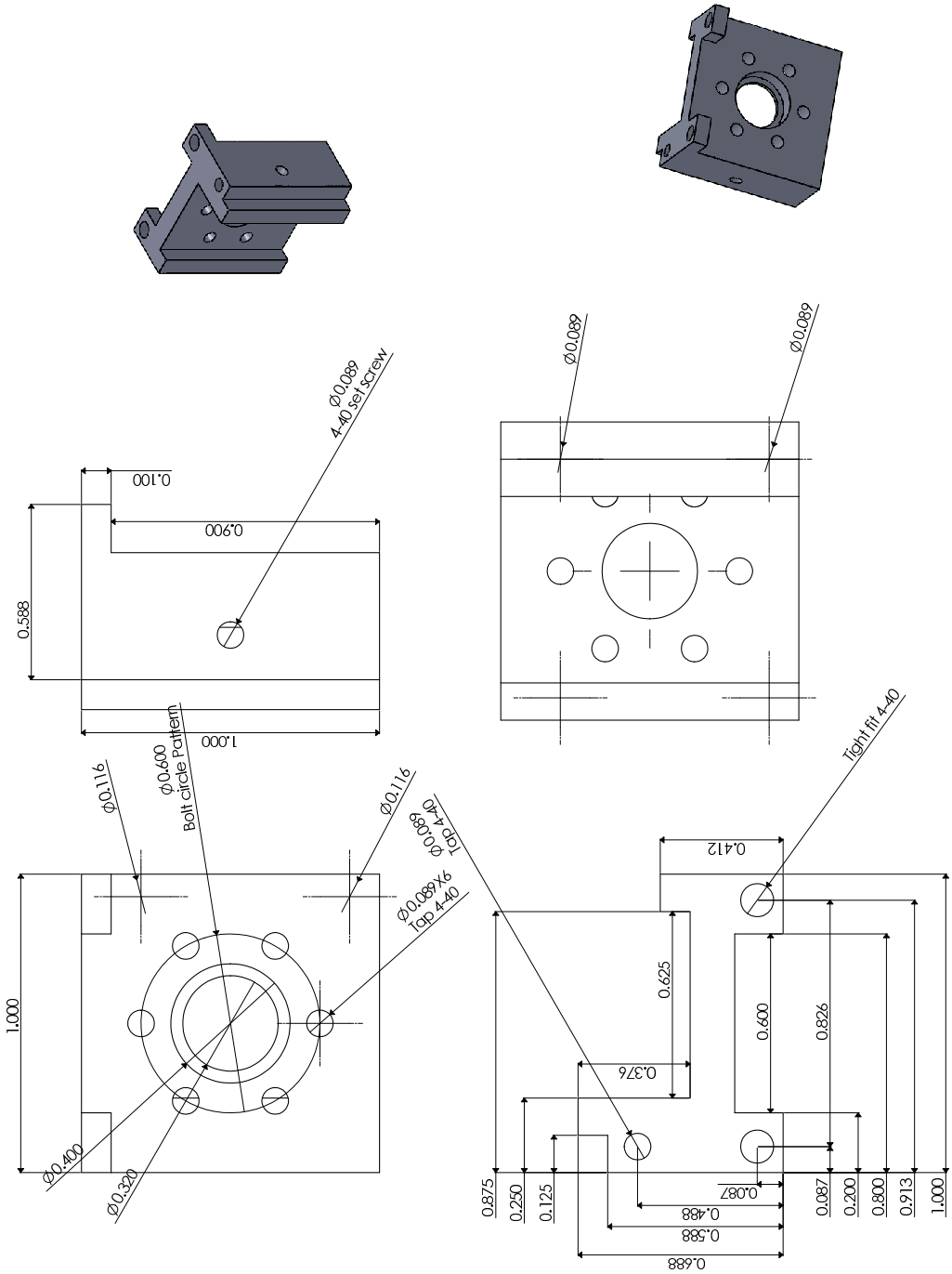

Figure A-10. Machine Drawing of top half of the second sound transducer mount

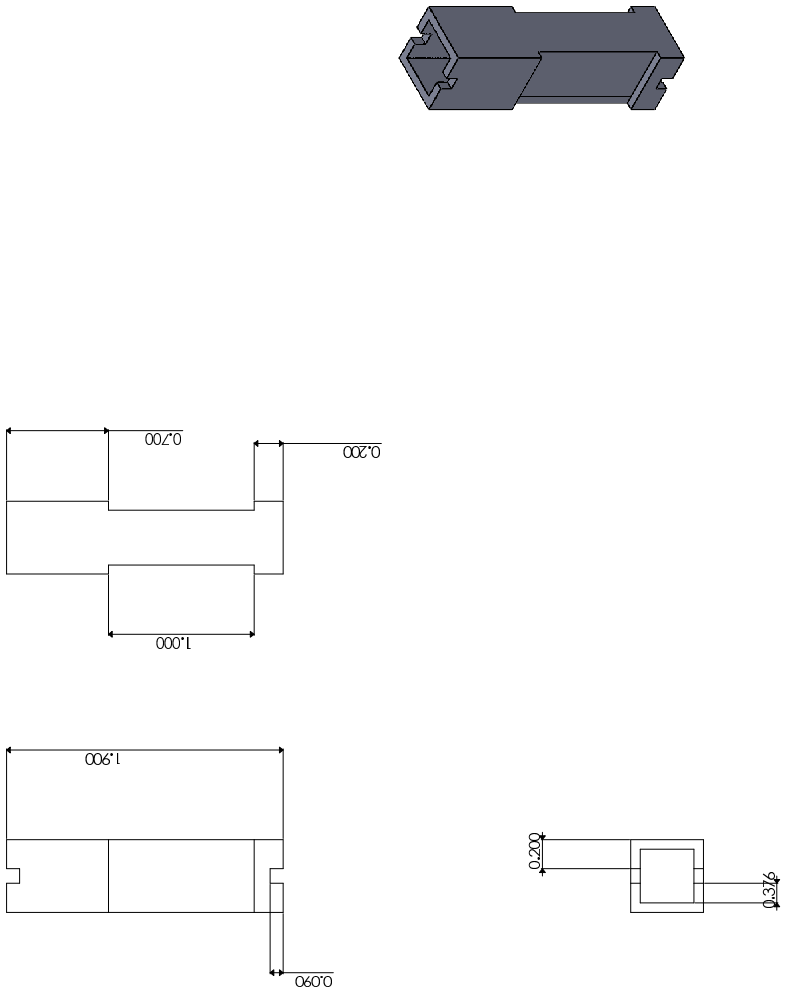

Figure A-11. Machine Drawing of top half of the second sound turbulence cell

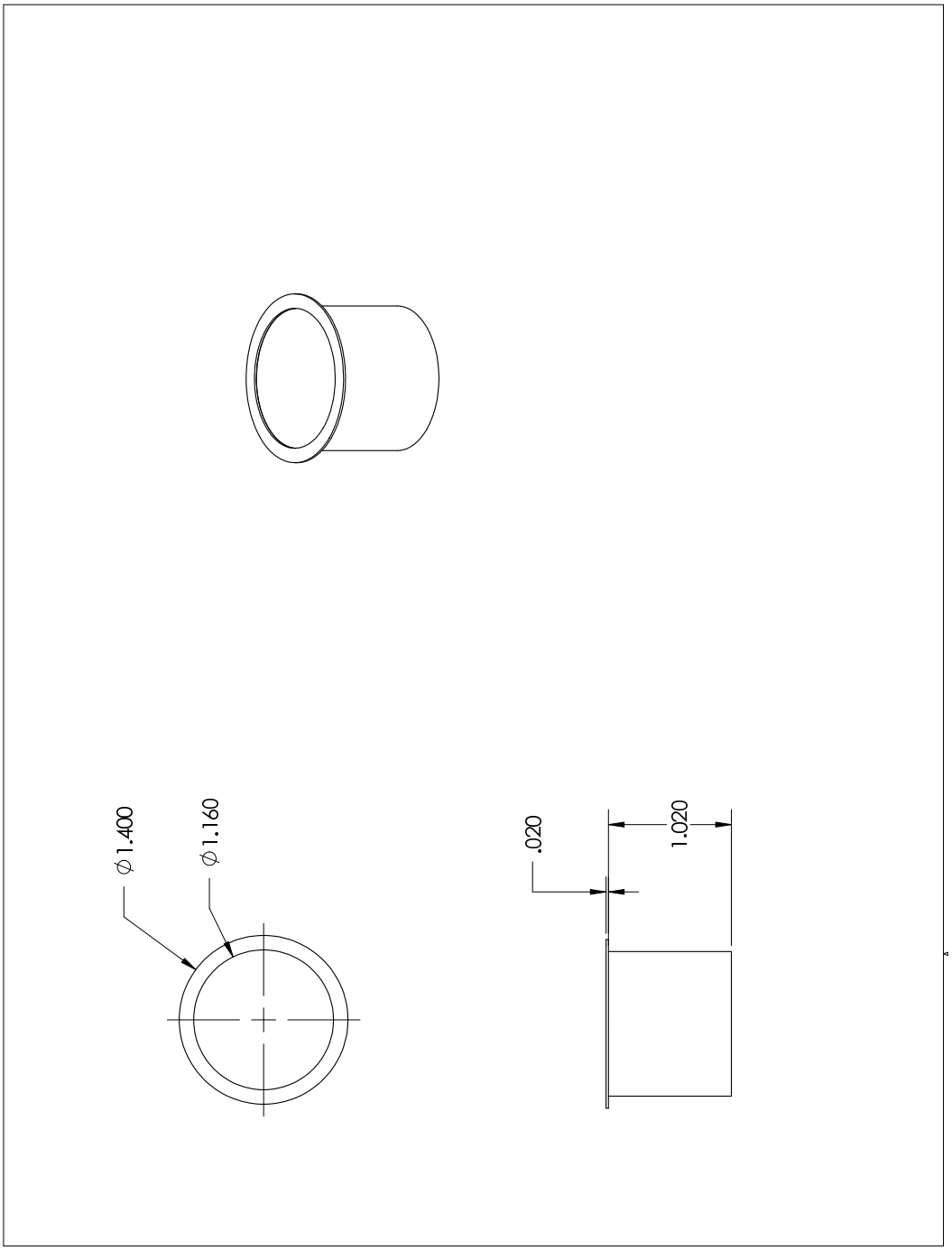

Figure A-12. Machine Drawing of bottom of the plastic impulse motor cell

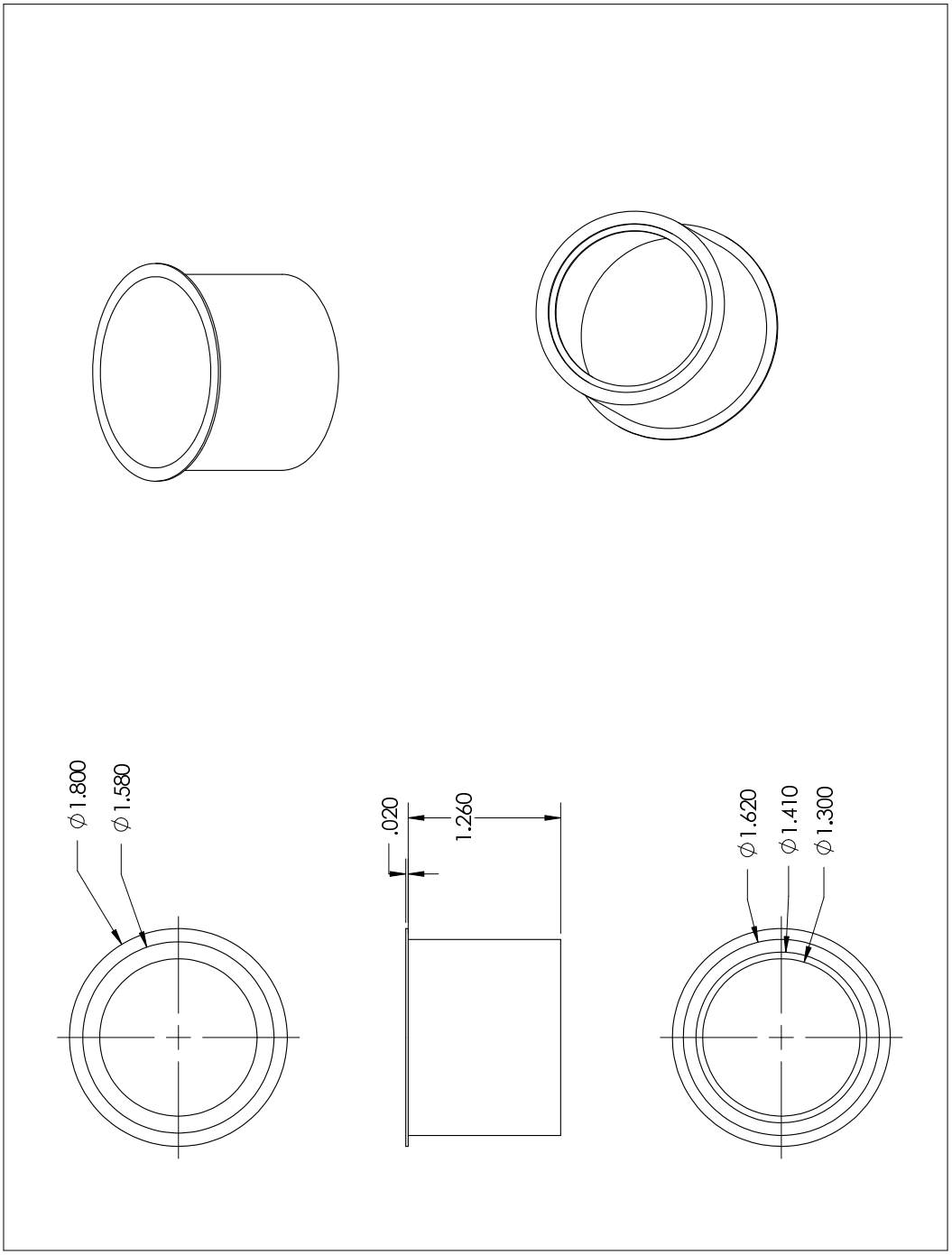

Figure A-13. Machine Drawing of middle of the plastic impulse motor cell

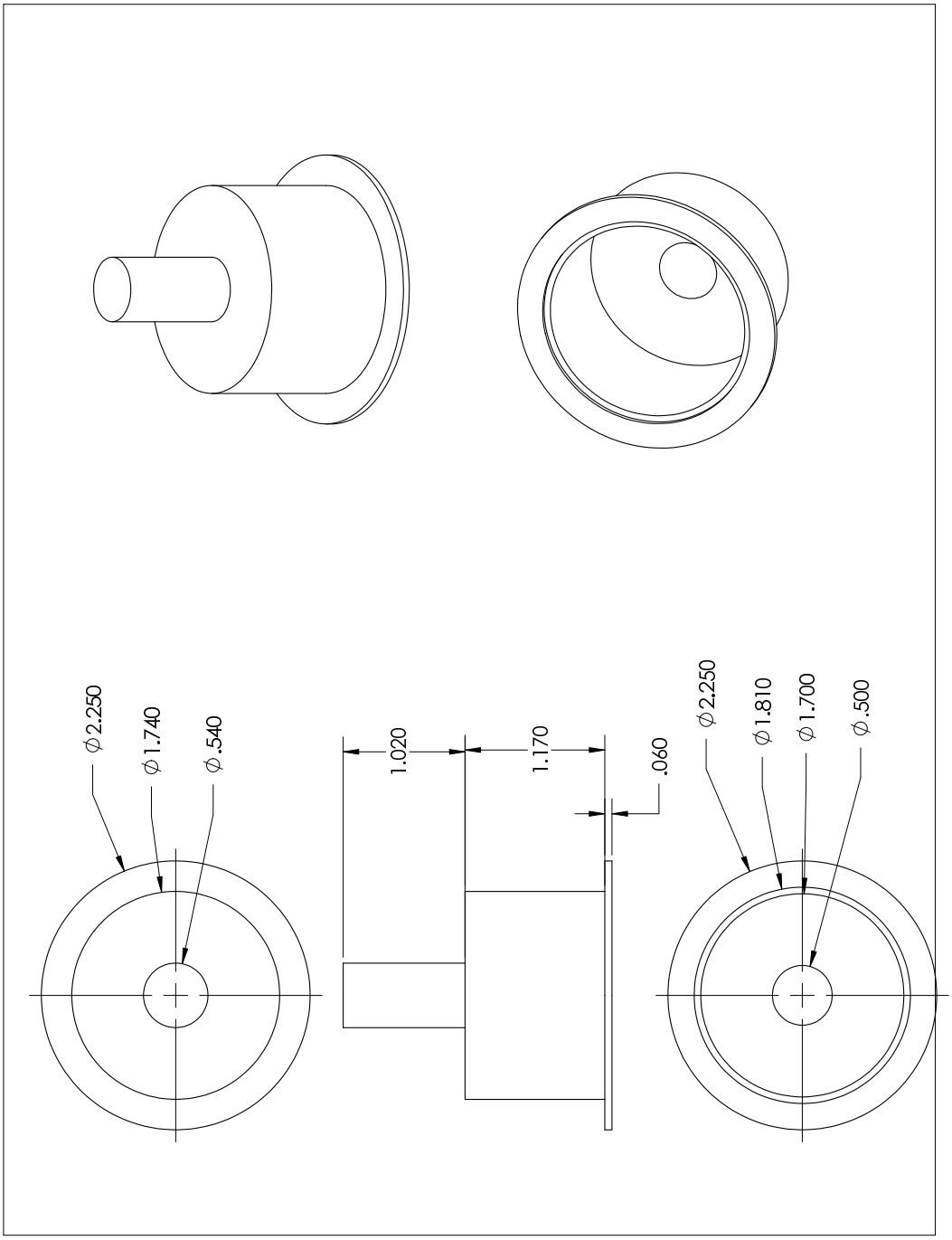

Figure A-14. Machine Drawing of top of the plastic impulse motor cell

REFERENCES

[1] H. Tennekes, J. Lumley, *A First Course in Turbulence*.

[2] R. L. Panton, *Incompressible flow* (John Wiley, New-York, 1984).

[3] L. Landau, E. Lifshitz, *Fluid Mechanics*, no. v. 6 in Course of theoretical Physics.

[4] A. Kolmogorov, *C. R. Acad. Sci. URSS* **30**, 301 (1941).

[5] L. Skrbek, J. J. Niemela, R. Donnelly, *Journal of Physics Condensed Matter* **11**, 7761 (1999).

[6] T. E. Toolbox, List of kinimatic viscosities. Available from: http://www.engineeringtoolbox.com/kinematic-viscosity-d_397.html.

[7] P. M. Walmsley, A. I. Golov, H. E. Hall, A. A. Levchenko, W. F. Vinen (2007).

[8] J. Allen, D. Misener, *Royal Society of London Proceedings Series A* **172**, 467 (1939).

[9] A. D. B. Woods, A. C. H. Hallett, *Canadian Journal of Physics* **41**, 596 (1963).

[10] J. Wilks, D. Betts, *An introduction to liquid helium*, Oxford science publications.

[11] L. Landau, *Phys. Rev.* **60**, 356 (1941).

[12] S. Putterman, *Superfluid Hydrodynamics*, North-Holland series in low temperature physics.

[13] D. Osborne, *Proceedings of the Physical Society A* **63**, 909 (1950).

[14] R. Feynman, *Progress in Low Temperature Physics* **1**, 34 (1955).

[15] F. London, *Superfluids: Macroscopic theory of superfluid helium*, Structure of matter series.

[16] L. Tisza, *Nat.* **141**, 913 (1938).

[17] V. Peshkov, *Dokl. Akad. Nauk SSSR* **45**, 365 (1944).

[18] *Physics Letters A* **84**, 435 (1981).

[19] D. Brewer, *Progress In Low Temperature Physics*, no. v. 8 in Progress in Low Temperature Physics.

[20] R. J. Donnelly, C. E. Swanson, *Journal of Fluid Mechanics* **173**, 387 (1986).

[21] R. Donnelly, *Quantized Vortices in Helium II*, Cambridge Studies in Low Temperature Physics.

[22] W. B. Hanson, J. R. Pellam, *Phys. Rev.* **95**, 321 (1954).

[23] J. R. Pellam, *Phys. Rev.* **75**, 1183 (1949).

[24] I. Khalatnikov, *Zh. eksp. teor. Fiz.* **20**, 243 (1950).

[25] K. R. Atkins, C. E. Chase, *Proceedings of the Physical Society. Section A* **64**, 826.

[26] J. Heiserman, I. Rudnick, *Journal of Low Temperature Physics* **22**, 481.

[27] G. G. Ihas, F. Pobell, *Phys. Rev. A* **9**, 1278 (1974).

[28] J. Heiserman, J. P. Hullin, J. Maynard, I. Rudnick, *Phys. Rev. B* **14**, 3862 (1976).

[29] Sterlitech, *0.3 μ m porosity* .

[30] S. Stalp, *Decay of Grid Turbulence in Superfluid Helium, Ph.D. thesis* (University of Oregon, Eugene, Or, 1998).

[31] C. Swanson, *A Study of Vortex Dynamics in Counterflowing Helium II, Ph.D. thesis* (University of Oregon, Eugene, Or, 1985).

[32] H. Hall, W. Vinen, *Royal Society of London Proceedings Series A* **238**, 204 (1956).

[33] H. Hall, W. Vinen, *Royal Society of London Proceedings Series A* **238**, 215 (1956).

[34] R. J. Donnelly, C. F. Barenghi, *http://pages.uoregon.edu/rjd/vapor1.htm* .

[35] M. S. Paoletti, M. E. Fisher, K. R. Sreenivasan, D. P. Lathrop (2008).

[36] C. F. Barenghi, R. J. Donnelly, W. F. Vinen, eds., *Quantized Vortex Dynamics and Superfluid Turbulence*, vol. 571 of *Lecture Notes in Physics, Berlin Springer Verlag* (2001).

[37] K. W. Schwarz, *Phys. Rev. B* **38**, 2398 (1988).

[38] M. Tsubota, T. Araki, S. K. Nemirovskii (2000).

[39] J. Koplik, H. Levine, *Phys. Rev. Lett.* **71**, 1375 (1993).

[40] M. Leadbeater, T. Winiecki, D. C. Samuels, C. F. Barenghi, C. S. Adams (2001).

[41] A. Leonard, *Annual Review of Fluid Mechanics* **17**, 523 (1985).

[42] W. T. Ashurst, D. I. Meiron, *Phys. Rev. Lett.* **58**, 1632 (1987).

[43] W. F. Vinen, J. J. Niemela, *Journal of Low Temperature Physics* **128**, 167.

[44] W. Thomson, *Philosophical Magazine Series 5* **10**, 155 (1880).

[45] B. V. Svistunov (1995).

[46] W. F. Vinen, *Phys. Rev. B* **61**, 1410 (2000).

[47] W. F. Vinen, *Phys. Rev. B* **64**, 134520 (2001).

[48] S. K. Nemirovskii (2010).

[49] V. S. L'vov, S. V. Nazarenko, O. Rudenko (2007).

[50] E. Kozik, B. Svistunov (2008).

[51] D. C. Samuels, C. F. Barenghi (1998).

[52] J. Maurer, P. Tabeling, *Europhys. Lett.* **43** (1999).

[53] J. Salort, *et al.*, *Phys. Fluids* **22**, 125102 (2010).

[54] A. M. Guénault, V. Keith, C. J. Kennedy, S. G. Mussett, G. R. Pickett, *Journal of Low Temperature Physics* **62**, 511.

[55] H. Yano, *et al.*, *Journal of Low Temperature Physics* **156**, 132.

[56] M. Blaďková, *et al.*, *Journal of Low Temperature Physics* **150**, 525.

[57] T. Zhang, S. W. van Sciver, *Nature Physics* **1**, 36 (2005).

[58] W. Guo, S. B. Cahn, J. A. Nikkel, W. F. Vinen, D. N. McKinsey (2010).

[59] N. Giordano, *Journal of Low Temperature Physics* **55**, 495.

[60] G. Zimmermann, F. Pobell, *Journal of Low Temperature Physics* **61**, 213.

[61] R. A. Sherlock, D. O. Edwards, *Review of Scientific Instruments* **41**, 1603 (1970).

[62] V. Dugaev, *et al.*, *Sensors, 2002. Proceedings of IEEE* (2002).

[63] *Cryogenics* **47**, 474 (2007).

[64] R. A. Antonia, N. Phan-Thien, A. J. Chambers, *Journal of Fluid Mechanics* **100**, 193 (1980).

[65] I. KHALATNIKOV, *ZHURNAL EKSPERIMENTALNOI I TEORETICHESKOI FIZIKI* **22**, 687 (1952).

[66] G. Pollack, *Reviews of Modern Physics* **41**, 48 (1969).

[67] P. Keesom, G. Seidel, *Physical Review* **113**, 33 (1959).

[68] *International Journal of Heat and Fluid Flow* **8**, 82 (1987).

[69] R. K. Childers, J. T. Tough, *Phys. Rev. B* **13** (1976).

[70] H. A. Nichol, L. Skrbek, P. C. Hendry, P. V. E. McClintock, *Phys. Rev. Lett.* **92** (2004).

[71] D. I. , *et al.*, *Phys. Rev. B* **85**, 224533 (2012).

[72] S. R. Stalp, L. Skrbek, R. J. Donnelly (1999).

[73] M. Giltrow, D. Charalambous, P. V. E. McClintock, *Journal of Physics: Conference Series* **150**, 012014.

[74] S.-c. Liu, G. Labbe, G. Ihas, *Journal of Low Temperature Physics* **145**, 165.

[75] S. Liu, *Quantum Turbulence: Decay of Grid Turbulence in a Dissipationless Fluid, Ph.D. thesis* (University of Florida, Gainesville, Fl, 2007).

[76] C. Kittel, *Introduction to Solid State Physics*, vol. 2012 (1995).

[77] N. Ashcroft, N. Mermin, *Solid state physics*, Holt-Saunders International Editions: Science : Physics (Holt, Rinehart and Winston, 1976).

[78] B. W. Maxfield, W. L. McLean, *Phys. Rev.* **139**, A1515 (1965).

[79] Y. Asada, H. Nosé, *Journal of the Physical Society of Japan* **26**, 347 (1969).

[80] D. Griffiths, *Introduction to electrodynamics* (Prentice Hall, 1999).

[81] D. Tilley, J. Tilley, *Superfluidity and Superconductivity*, Graduate Student Series in Physics.

[82] B. N. Engel, G. G. Ihas, E. D. Adams, C. Fombarlet, *Review of Scientific Instruments* **55**, 1489 (1984).

[83] S. Denis, M. Dirickx, P. Vanderbemden, M. Ausloos, B. Vanderheyden, *Superconductor Science and Technology* **20**, 418.

[84] G. Ihas, G. Labbe, S. Liu, K. Thompson, *Journal of Low Temperature Physics* **150**, 384.

[85] K. Thompson, S. Liu, G. Labbe, G. Ihas, *Journal of Physics: Conference Series* **150** (2009).

[86] S. R. Stalp, J. J. Niemela, W. F. Vinen, R. J. Donnelly, *Physics of Fluids* **14**, 1377 (2002).

[87] F. Pobell, *Matter and Methods at Low Temperatures*.

[88] F. Fiorillo, I. Mayergoyz, *Characterization and Measurement of Magnetic Materials*, Elsevier series in electromagnetism.

[89] W. Pan, *et al.*, *Phys. Rev. Lett.* **83**, 3530 (1999).

[90] *Cryogenics* **24**, 477 (1984).

[91] P.-C. Ho, R. B. Hallock, *Journal of Low Temperature Physics* **121**, 797.

[92] K. DeConde, G. A. Williams, R. E. Packard (1974).

BIOGRAPHICAL SKETCH

Kyle J. Thompson was raised in the valley of Amherst, Massachusetts, looking up at the foothills of the Berkshires. He graduated from the same high school as both of his parents, Amherst Regional High School, in 2002. Afterward he immediately enrolled at The University of Massachusetts to pursue his interests in math, physics and engineering. During his time in college he gravitated away from engineering to the more purely scientific pursuits. Early on he flirted with the soft sciences, working in microbiology for Dr. Lovely's lab, but then smartened up to study fundamental physics in Dr. Hallock's laboratory. After geting his feet wet with helium physics and graduating in the fall of 2006 with honors degrees in both mathematics and physics from the commonwealth college he enrolled in a Ph.D. program at the University of Florida. For 5 of the next 6 years he went on to work in the laboratory of low temperature physics with Prof. Ihas producing the document in front of you today. After his Ph.D. he has agreed to take on a post doctoral position at the University of Sao Paulo in Sao Carlos Brazil studying Bose-Einstein condensates.